2016

Impacts of Rock-Brine Interactions on Petrophysical Properties of a Sandstone Reservoir, Utilizing Geochemical and Pore Network Modeling

Masoud Safari-Zanjani
Louisiana State University and Agricultural and Mechanical College

IMPACTS OF ROCK-BRINE INTERACTIONS ON PETROPHYSICAL PROPERTIES OF A SANDSTONE RESERVOIR, UTILIZING GEOCHEMICAL AND PORE NETWORK MODELING

A Dissertation

Submitted to the Graduate Faculty of the
Louisiana State University and
Agricultural and Mechanical College
in partial fulfillment of the
requirements for the degree of
Doctor of Philosophy

in

The Craft & Hawkins Department of Petroleum Engineering

by
Masoud Safari-Zanjani
B.S., Iran University of Science and Technology, 2005
M.S., Bu-Ali Sina University, 2008
August 2016

Acknowledgements

First and foremost, I would like to thank my parents whose love and moral support sustained me throughout. I am eternally indebted to my parents for their endless love, support and encouragement. Indeed, to them is this work dedicated.

I would like to thank my advisers Dr. Karsten E. Thompson and Dr. Stephen O. Sears for providing me with guidance and the resources, my Geology minor advisor Dr. Jeffrey S. Hanor for his invaluable contributions, and other committee members Dr. Richard Hughes and Dr. Clinton Willson for their supports that have given shape to this work. I also would like to thank Dr. Christopher D. White for his contributions in the earlier part of this research. I want to thank the PoreSim and LSU's geothermal research groups.

I am appreciative of my friends and colleagues with whom I shared and gained useful ideas. This includes, Dr. Amin Mirsaeidi, Timothy Thibodeaux, Godfrey Mills, Paulina Mwangi and Dr. Ali Takbiri. Portions of this research were conducted with high performance computing resources provided by Louisiana State University (http://www.hpc.lsu.edu). Shared Instrument Facility (SIF) at LSU is also appreciated for their assistance in this project. I also thank Dr. Dongmei Cao, Dr. Amar Karki, Mrs. Wanda LeBlanc, and Mr. Fenelon Nunes for their assistance in conducting some of the rock characterization tests.

Portions of this work were performed at GeoSoilEnviroCARS (The University of Chicago, Sector 13), Advanced Photon Source (APS), Argonne National Laboratory. GeoSoilEnviroCARS is supported by the National Science Foundation - Earth Sciences (EAR-1128799) and Department of Energy- GeoSciences (DE-FG02-94ER14466). This research used resources of the Advanced Photon Source, a U.S. Department of Energy (DOE) Office of Science User Facility operated for the DOE Office of Science by Argonne National Laboratory under Contract No. DE-AC02-06CH11357.

I gratefully acknowledge financial support for this work from the U.S. Department of Energy under grant DE-EE0005125.

This dissertation is dedicated to my parents Khalilollah and Parvin, my wife Mina, my brothers Mehrdad and Daryoush, my nephew Kiarash, and my nieces Niloufar and Hila.

Table of Contents

List of Tables

List of Figures

Abstract

Unfavorable consequences of geochemical reactions, such as calcite and silica scaling, in geothermal power plant surface facilities have been discussed in many recent studies. However, the impact of brine-rock interactions related to geothermal projects on reservoir properties has not been addressed fully. In this study, interactions between geothermal fluid and reservoir rocks in two fields located in Vermilion Parish, LA, and Chocolate Bayou, TX, are examined using geochemical modeling. The studied reservoir belongs to the Frio formation. In the geochemical models, the brine is cooled down to the estimated output temperature of a geothermal heat exchanger and re-equilibrated. Then, brine-rock interactions at reservoir temperature are simulated, and the changes of rock composition due to geochemical reactions are anticipated. Results show that the pore space volume change is negligible. Feldspar transformation to clay minerals, however, has been observed as a mineral conversion process which is expected to impact permeability.

Pore Network Modeling has been utilized to investigate the impact of the geochemical interactions on the reservoir permeability. To build the pore network, micro-CT scan images were acquired from three core samples. The image segmentation was done considering the results of rock characterization studies. After completing the objective segmentation, the anticipated geochemical changes were incorporated into the micro-CT scan images using a computer code. Permeability of the resulted image was calculated and compared to the initial permeability calculations. The impact of the micro-porosity of newly formed clay minerals was estimated using an innovative method. Results indicate that the newly generated clay minerals due to the geochemical reactions may cause important damage, as high as 50 percent, to reservoir permeability.

Chapter 1
Introduction

1-1 Geothermal Resources

Geothermal energy resources have recently attracted the interest of the global energy sector. With just over 3.5 GW of operating nameplate capacity and just over 2.7 GW of net capacity, the United States is a world leader and innovator in terms of new geothermal technologies (GEA, 2015). The majority of geothermal power plants in the US are located in California and Nevada. Louisiana is one of the states that recently have started to study the development of the geothermal source of energy. These projects are mostly focused in southwest Louisiana where the depleted oil wells could possibly be re-operated to produce geothermal fluids.

Heat flowing from the earth's core and mantle and from radioactive isotopes decaying in the earth's crust is the energy source for geothermal power projects. In the conventional geothermal power plants water adsorbs heat from the rock and transports it to the earth's surface, where turbines and generators convert heat into electrical energy.

Geothermal often cannot compete with fossil fuels commercially. The cost of drilling enough wells to supply full plant capacity is almost equivalent to purchasing most of the fuel required for the next 20 years in a fossil-fired plant (Gallup, 2009). On the other hand, after operating the geothermal power plant the costs will be mostly the maintenance expenses. Therefore, a geothermal power plant has to work reliably for a long period of time to be profitable.

Although, considerable efforts have been made to solve the scaling problem in production and surface facilities, the impact of rock-brine interactions on reservoir properties has not been addressed as fully. In this study, interactions between geothermal fluid and reservoir rocks are examined using geochemical modeling and also the impacts of these interactions on reservoir behavior are studied using pore network modeling.

1-2 Objectives

In the case of high salinity geo fluid, corrosion and scale forming may cause serious problems in production and surface facilities and also impact the reinjection process. In a proposed geothermal research project by the LSU geothermal research group, contrary to conventional geothermal power plants, heat exchangers will be installed in a horizontal well, and the heat exchanging process will happen inside the reservoir. Therefore, no geothermal fluid will be produced on the surface. The heat energy of the geothermal reservoir will be transferred to the surface facilities by a working fluid (Fig. 1-1).

Permeability damage due to mineral transformations and scale formation in the heat exchanger can be a potential problem for operating downhole heat exchangers. In the proposed project by the LSU geothermal research group, the injection of hot brine to the heat exchangers will be done by pumps. To produce electricity economically, a specific amount of flow rate into the heat exchangers must be maintained. In case of losing the reservoir permeability due to geochemical reactions, pumps will have to work harder and will consume more energy. In some point, a considerable amount of produced energy by the power plant will be consumed in pumps, and at this point the project will not be economic anymore. Therefore, investigation of the reservoir permeability damage due to geochemical reactions is of crucial importance.

The objective of this project is to estimate the risk of permeability reduction in result of rock-brine geochemical interactions considering temperature drop and geo-fluid circulation in life span of a geothermal power plant. For this purpose, geochemical reactions between reservoir rock and brine were modeled using the Geochemist's Workbench software (Bethke, 2008). In the next step, pore network modeling was utilized to evaluate the permeability changes due to geochemical alterations. Knowing the probable rock composition alterations, geochemical changes were applied to a micro-CT scan image of a core using a new algorithm. The pore network models, then, were formed using the micro-CT scan images and the permeability changes were calculated using another algorithm.

In chapter 2, the performed procedure to determine rock composition of studied core samples are presented. Chapter 3 investigates the possible geochemical changes due to rock-brine interactions in the studied area. In chapter 4, the impact of the anticipated geochemical changes

on permeability are studied utilizing pore network modeling. Chapter 5 presents a summary of the conclusions of this study and also addresses future research ideas that might be fruitful to other researchers.

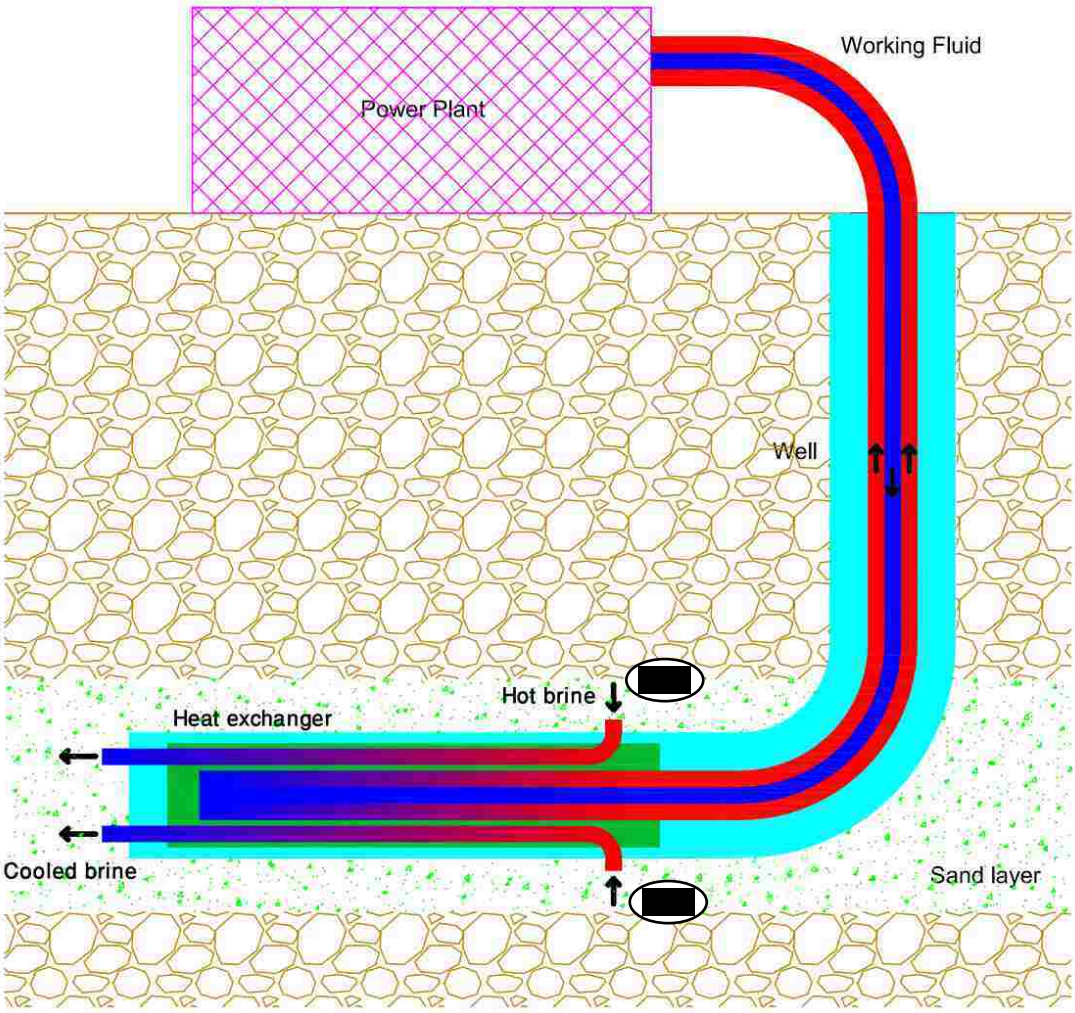

Figure 1-1. The proposed geothermal research project by the LSU geothermal research group. Instead of production of hot brine on the surface, heat exchangers will be transferred to the reservoir and the heat exchanging process will happen inside the reservoir.

Chapter 2
Rock Characteristics

2-1 Study area

In the late 1970s, a program was started by the U.S. Department of Energy (DOE) to investigate the geothermal-geopressured formations in southwest Louisiana. This program included "identification, qualification, acquisition, planning and conducting of geothermal-geopressured formation tests in oil or gas prospective wells about to be drilled, being drilled, or being abandoned" (Dobson et al., 1980). This study included data collected from the Beulah Simon No. 2 well. The tests on this well were conducted by Gruy Federal, Inc., under a contract with the DOE (Dobson et al., 1980). The Beulah Simon No. 2 is located in the Cossinade field area, Vermilion Parish, Louisiana, about 5 miles (8 kilometers) northeast of the town of Kaplan and 30 miles (50 kilometers) southeast of Lafayette (Fig. 2-1) (Dobson et al., 1980). The reason for choosing this area is that the reservoir temperature and permeability seem to be suitable for a binary geothermal power plant. In addition, the possible re-operation of the available depleted oil wells in this area can potentially save considerable amount of money by avoiding drilling of new wells.

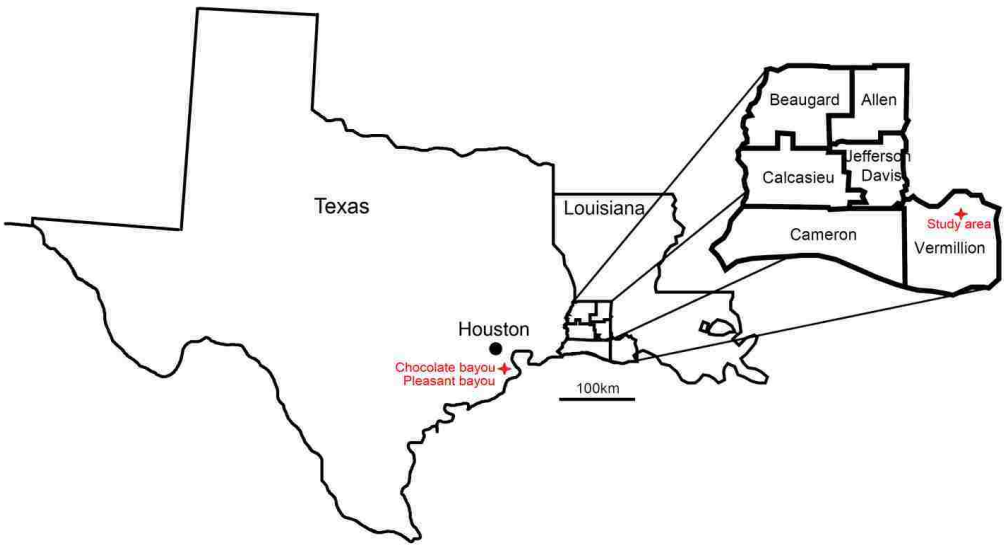

Figure 2-1. Approximate location of the study area. The data collected from Beulah Simon No. 2 well have been used for this study (adapted from Szalkowski, 2003 and Dobson et al., 1980).

Diapiric salt of Jurassic age and sediments of Recent to Cretaceous age have been encountered in the DOE's study (Dobson et al., 1980). This area has a regional dip of about 3 percent at 10,000 to 12,000 feet (3,000 to 3660 m) toward the south (Dobson et al., 1980). The "mother" layer of the salt domes in this area, the Louann Salt, underlies the area at an estimated depth of at least 40,000 feet (Dobson et al., 1980).

The maximum reservoir pressure gradient is about 1 psi per foot in the geopressured environment and it has a normal hydrostatic value of 0.465 psi per foot in the sand and sand-shale facies (Dobson et al., 1980). The target formation, which is geopressured-geothermal, consists of a thick bed of Camerina A sand, a member of the Frio formation. The net sand thickness for the Camerina A section at the Beulah Simon No.2 is 266 feet (80 m) (Dobson et al., 1980). Some of the geological and petrophysical information of this area has been summarized in Table 2-1 (Dobson et al., 1980).

Table 2-1. Geological and petrophysical information of study area (Dobson et al., 1980).

Total depth	15,265 ft
Formation	Camerina (Upper Oligocene)
Perforated interval	14,674-14,770 ft
Original reservoir pressure	13,015 psi at 14,722 ft
Original reservoir temperature	130 °C (266 °F)
Total dissolved solids	103,925 ppm
Net sand thickness	266 ft
Porosity	17.4 percent
Permeability	12 md

The rock mineralogy composition of Camerina A sand in Vermilion Parish has not been reported in the Beulah Simon No.2 well investigations. The Frio formation is one of the major oil and gas producing formations in the Texas and Louisiana Gulf Coast. For this study, two rock compositions were used. One rock composition was assumed based on studies performed by other researchers on the Frio formation of the Texas Gulf Coast (Chocolate Bayou, Texas) with similar reservoir temperatures and depths (Land and Millikan, 1981, Lynch, 1996 and 1997). The second rock composition is based on analysis of three core samples from the Pleasant Bayou

field, Texas obtained for the purpose of the present study from the Bureau of Economic Geology (BEG) Core Research Center (CRC). These samples were taken from different depths (Fig. 2-2), but close to the desired depth of the study area in Vermilion parish, Louisiana. These samples also belong to the Frio formation, thus were used to build the pore network model and study the impact of rock-brine geochemical interactions on permeability in the study area. In this chapter, procedures performed to understand the composition of the core samples will be discussed. To refer to the samples, the last two digits of the sampling depth were used as the sample name.

(a) (b) (c)

Figure 2-2. The core samples from Pleasant Bayou, Texas, from different depths: (a)14759 ft, (b)14761 ft, (c)14762 ft.

2-2 Porosity measurement

The porosity of samples was measured with the fluid saturation method (Torsæter and Abtahi, 2000). In the fluid saturation method, pore volume is calculated by subtracting the weight of the saturated sample from the dry weight. The bulk volume is calculated by subtracting the weight of saturated sample immersed in water from the weight of saturated sample. The porosity is equal to the pore volume divided by the bulk volume. The results of the porosity tests are shown in Table 2-2.

Table 2-2. The porosity tests results, percent.

Sample	fluid saturation method
59	20.66
61	21.62
62	18.87

2-3 Permeability measurement

The permeability measurements were done using a gas permeameter, Ruska model (Fig. 2-3) (Ruska Permeameter Operating Manuals). After mounting the sample to the instrument, an upstream pressure of 0.25 atm is applied to the system by adjusting the regulator. The barometric pressure (mmHg, corrected for temperature and latitude), pressure (atm), gas temperature (°C) and flow rate tube reading (cm) are recorded for this upstream pressure. The measurements are repeated for upstream pressures of 0.5, 0.75 and 1.0 atm. The gas flow rate can be obtained from the available graphs. With the flow rate in hand, the permeability can be calculated using the Darcy equation and corrected for slippage using the Klinkenberg equation (Klinkenberg, 1941).

Figure 2-3. Gas permeameter (Ruska permeameter).

The permeability of samples is shown in Table 2-3. To confirm the accuracy, the samples were sent to the Weatherford Laboratories Co. and the permeability measurement was performed again. Although the results of two measurements are close, the Weatherford lab results were used for the rock characterization studies.

Table 2-3. The permeability tests results, mD.

Sample	LSU Lab		Weatherford Lab	
	To air	Klinkenberg corrected	To air	Klinkenberg corrected
59	1568	1454	1760	1690
61	629	562	650	612
62	208	190	117	105

2-4 Scanning Electron Microscope (SEM)

The scanning electron microscope (SEM) is a sophisticated analytical equipment which is increasingly used to answer complex questions in the energy industry (Welton, 2003). In this study, the SEM was used to investigate the type of clay minerals present in the samples and to study the effect of these minerals on the possible reservoir permeability damage.

In the electron microscope, an internally generated electron beam is used to form the SEM image (Welton, 2003). To form the SEM images, the coated samples are placed in the sample chamber. The sample chamber then is evacuated to high vacuum.

The rock samples should be large enough that a fresh uncontaminated surface can be obtained. The SEM sample, however, should be small enough to fit into the sample chamber (Welton, 2003). In this study the cut samples were attached to a SEM specimen plug and dried overnight in a low temperature oven (Fig. 2-4). Then samples were gold coated in a SEM sputtering coating machine (made by Electron Microscopy Sciences) (Fig. 2-5).

Figure 2-4. SEM gold coated samples.

Figure 2-5. SEM sputter coating machine.

The SEM images were obtained with 50X, 80X, 500X, 1000X, and 3500X magnification for each rock sample. Fig. 2-6 shows the FEI Quanta 3D FEG FIB/SEM dual beam system at the Socolofsky Microscopy Center (SMC) of LSU, which was utilized in this study.

The obtained SEM images were compared to demonstrated types in SEM Petrology Atlas by Welton (2003) and the type of crystal morphology of clay minerals were identified.

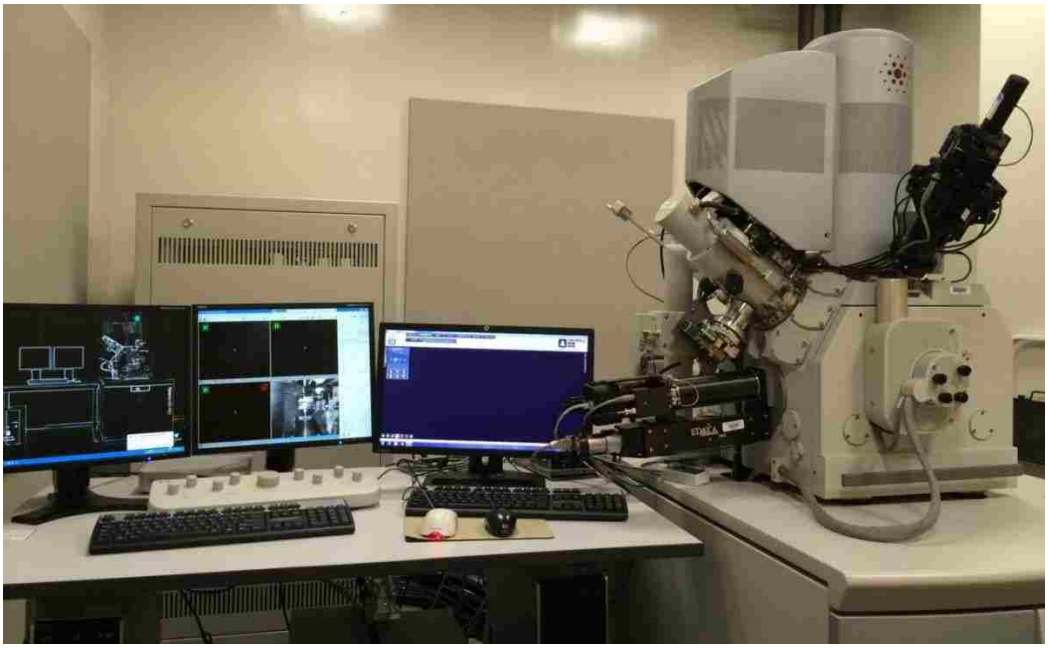

Figure 2-6. The SEM machine utilized in this study.

2-4-1 Sample 59

The comparison of the images obtained for sample 59 (Fig. 2-7) with Welton (2003) indicates that pore-lining authigenic chlorite can be found in this sample. This chlorite forms a thin, uniform layer around the grains. Individual crystals, which are 2 to 5 µm, are oriented edge to face.

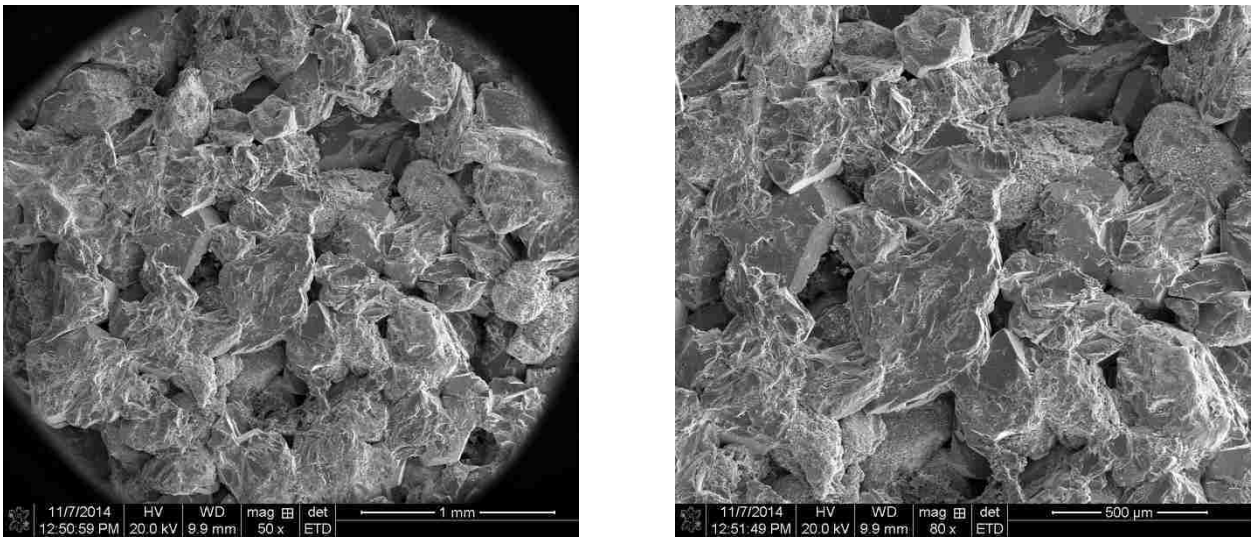

(a) (b)

Figure 2-7. The SEM images for sample 59, (a) 50X, (b) 80X, (c) 500X, (d) 1000X, and (e) 3500X. Pore-lining authigenic chlorite mixed with quartz can be found in this sample.

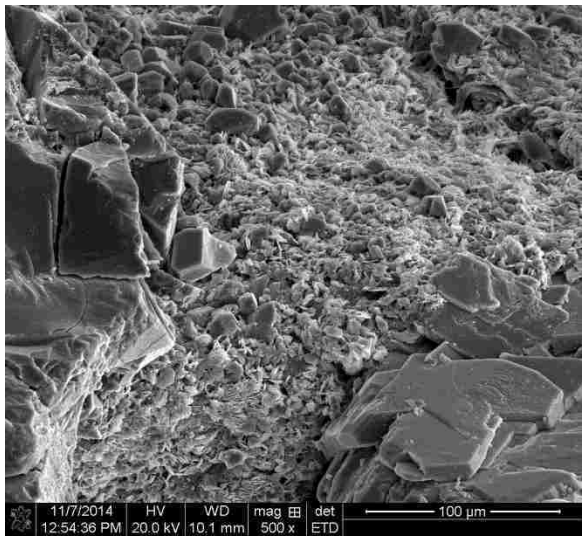

(c)

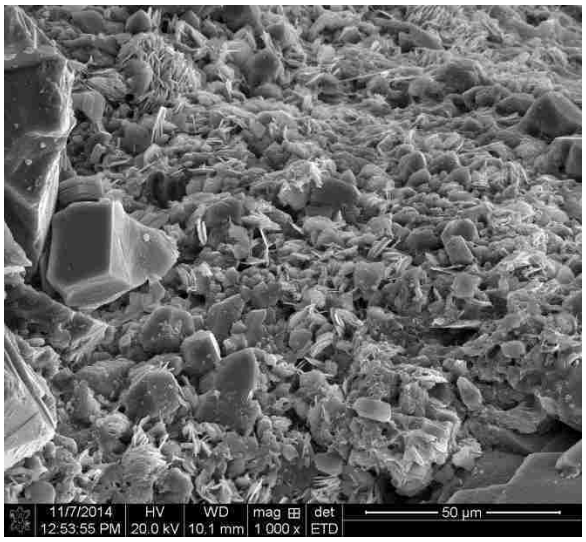

(d)

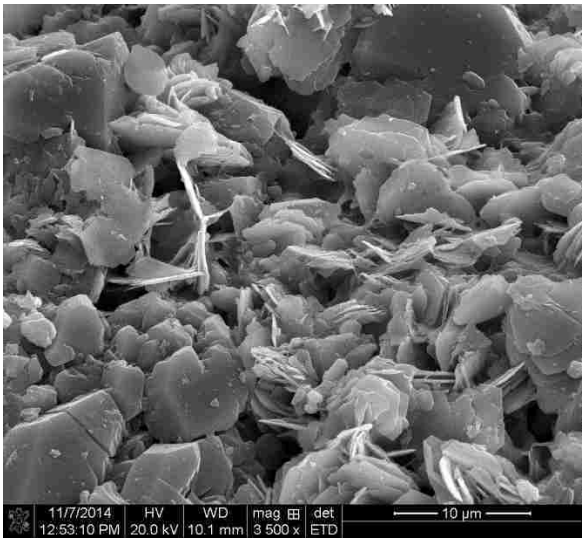

(e)

Figure 2-7 (continued). The SEM images for sample 59, (a) 50X, (b) 80X, (c) 500X, (d) 1000X, and (e) 3500X. Pore-lining authigenic chlorite mixed with quartz can be found in this sample.

2-4-2 Sample 61

The comparison of the obtained images for sample 61 (Fig. 2-8) with Welton (2003) indicates that well-crystallized, authigenic kaolinite can be found in this sample. This kaolinite partly fills the pores. The kaolinite occurs as face-to-face stacks of pseudohexagonal plates or books (Welton, 2003). Individual crystals range from 5 to 15 µm diameter (Fig. 2-8(e) is a close-up of kaolinite books).

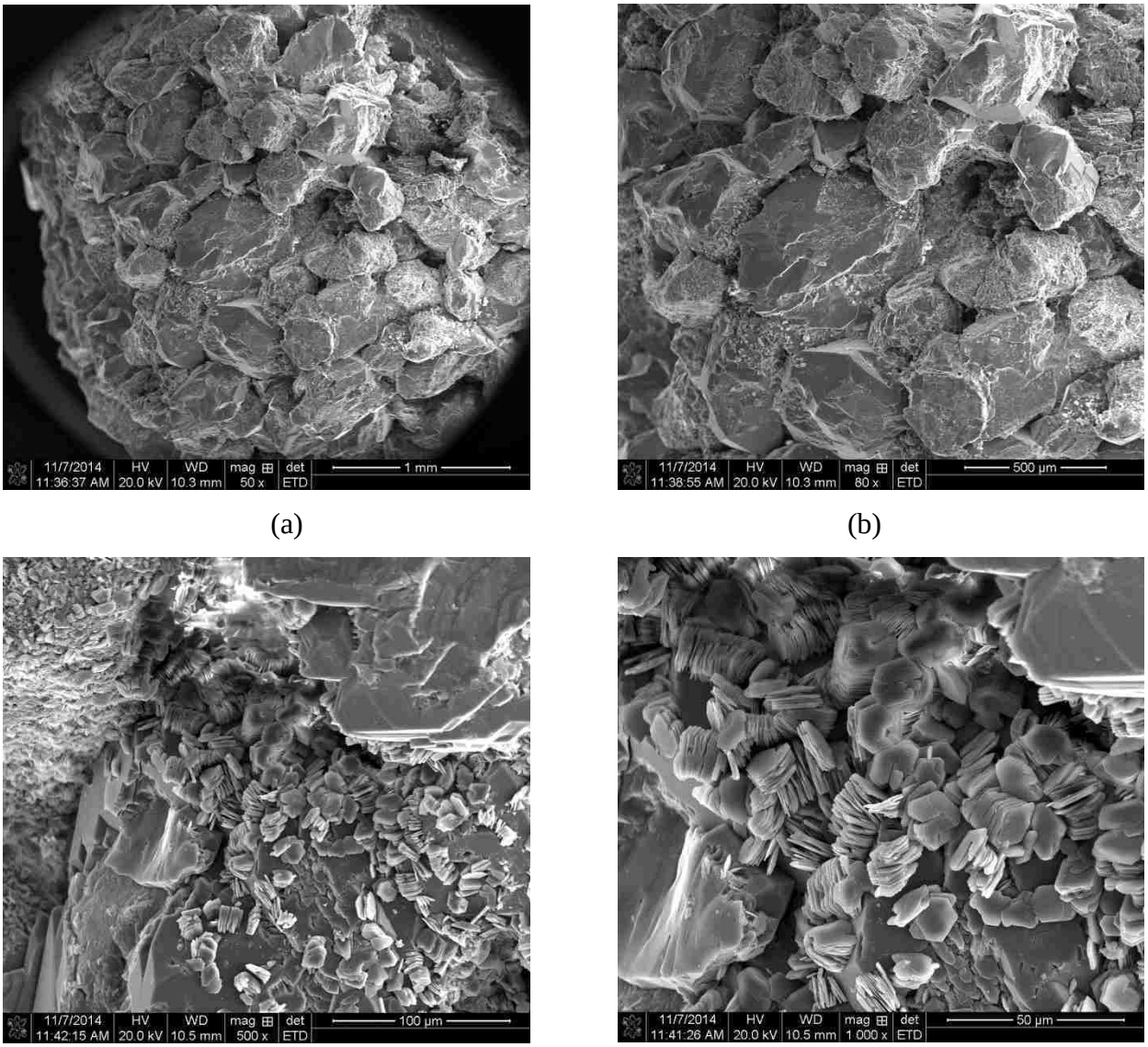

Figure 2-8. The SEM images for sample 61, (a) 50X, (b) 80X, (c) 500X, (d) 1000X, and (e) 3500X. Well-crystallized, authigenic kaolinite can be found in this sample.

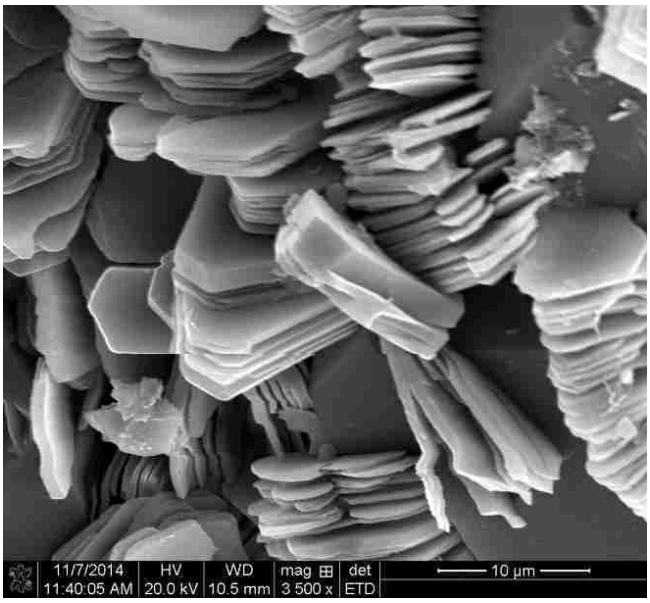

(e)

Figure 2-8 (continued). The SEM images for sample 61, (a) 50X, (b) 80X, (c) 500X, (d) 1000X, and (e) 3500X. Well-crystallized, authigenic kaolinite can be found in this sample.

Chlorite crystals, similar to sample 59, can also be found in the sample 61 (Fig. 2-9).

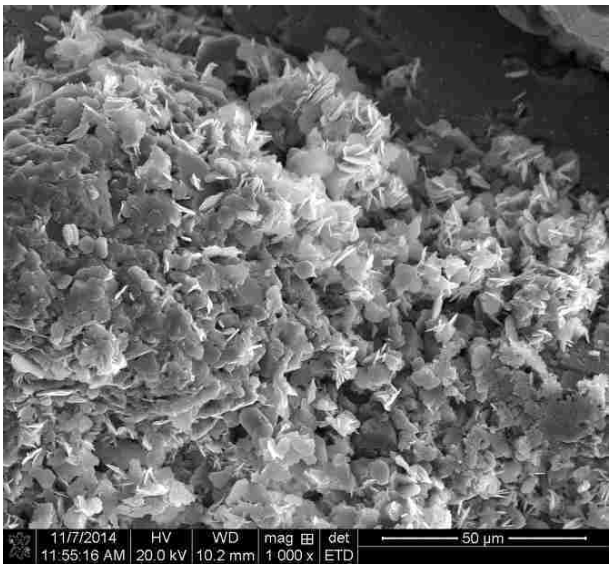

(a)

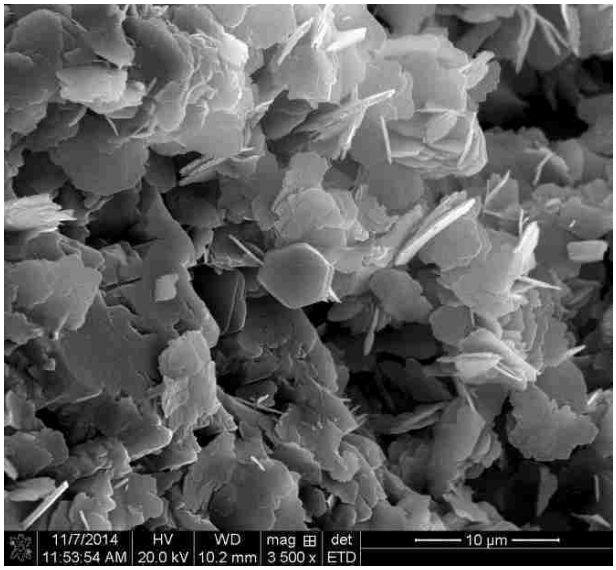

(b)

Figure 2-9. The SEM images for sample 61, (a) 1000X, and (b) 3500X. Pore-lining authigenic chlorite mixed with quartz can be found in this sample.

2-4-3 Sample 62

The comparison of the obtained images for sample 62 (Fig. 2-10) with Welton (2003) indicates that well-developed, webby pore-lining authigenic smectite can be found in this sample.

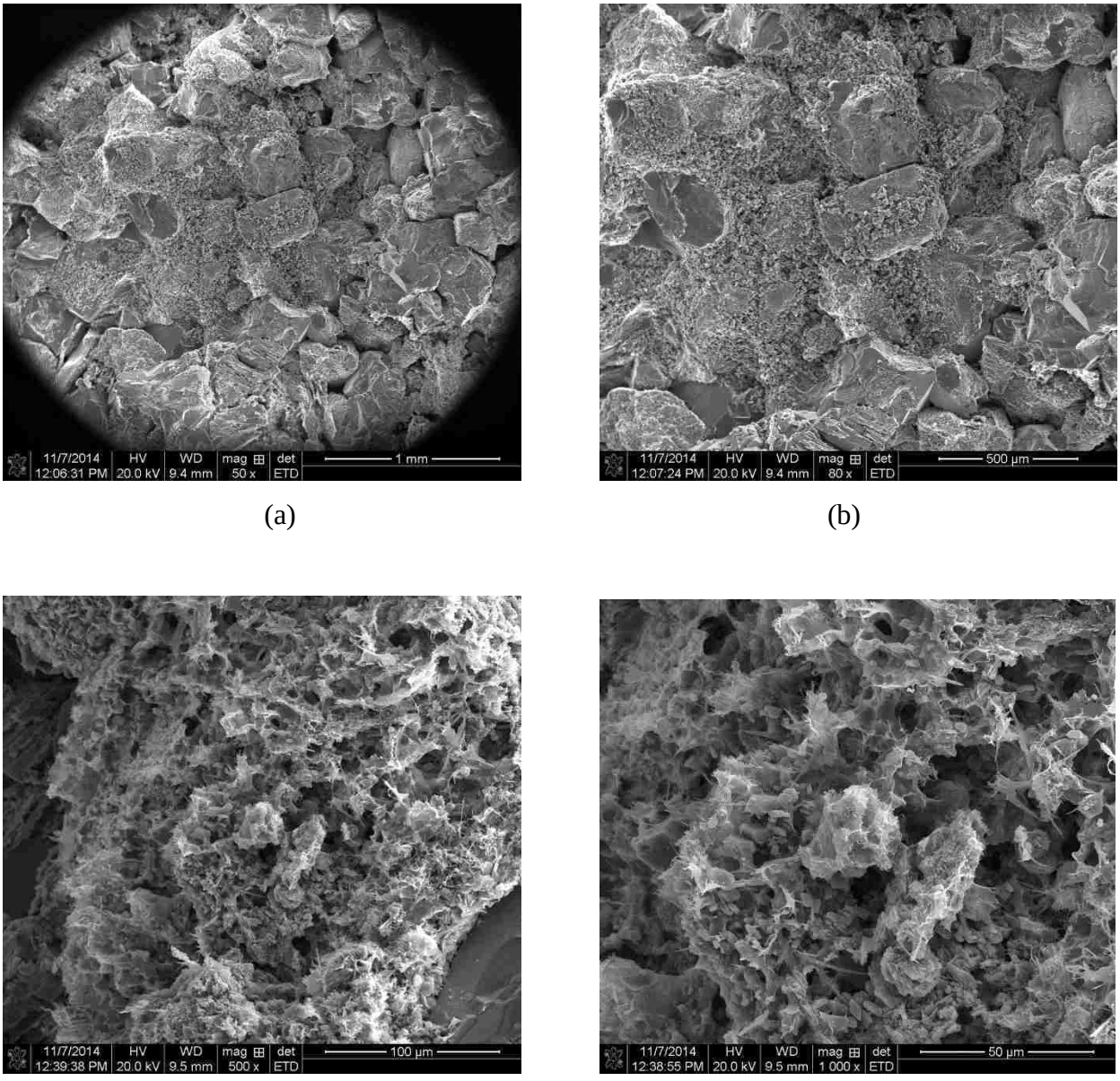

(a) (b)

(c) (d)

Figure 2-10. The SEM images for sample 62, (a) 50X, (b) 80X, (c) 500X, (d) 1000X, and (e) 3500X. Well-developed, webby pore-lining authigenic smectite can be found in this sample.

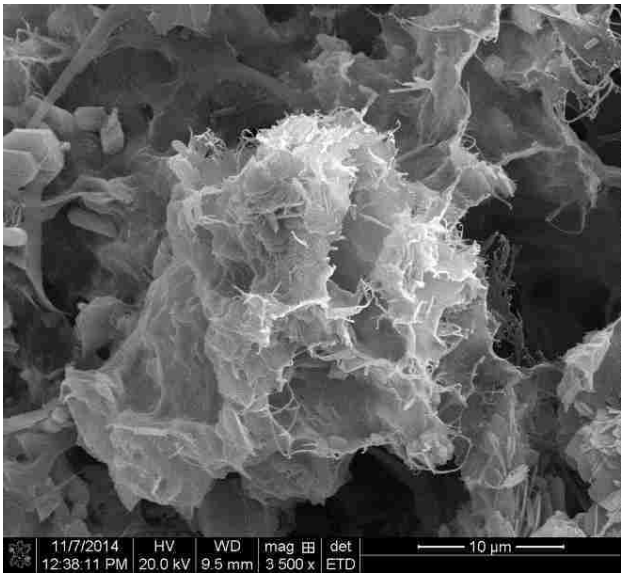

(e)

Figure 2-10 (continued). The SEM images for sample 62, (a) 50X, (b) 80X, (c) 500X, (d) 1000X, and (e) 3500X. Well-developed, webby pore-lining authigenic smectite can be found in this sample.

Kaolinite crystals, similar to those found in sample 61, were also found in sample 62 (Fig. 2-11).

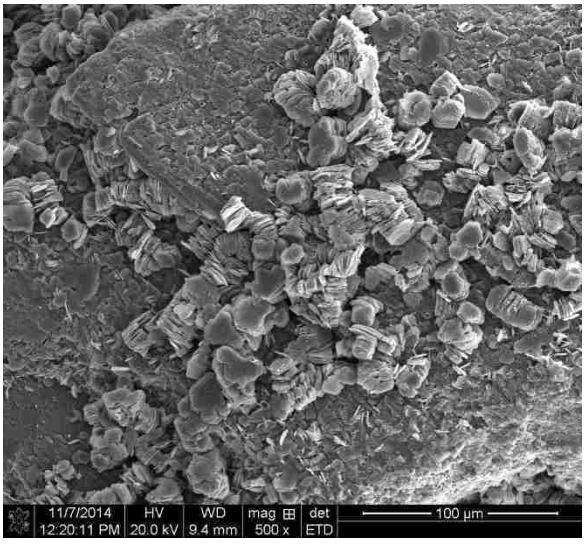

(a)

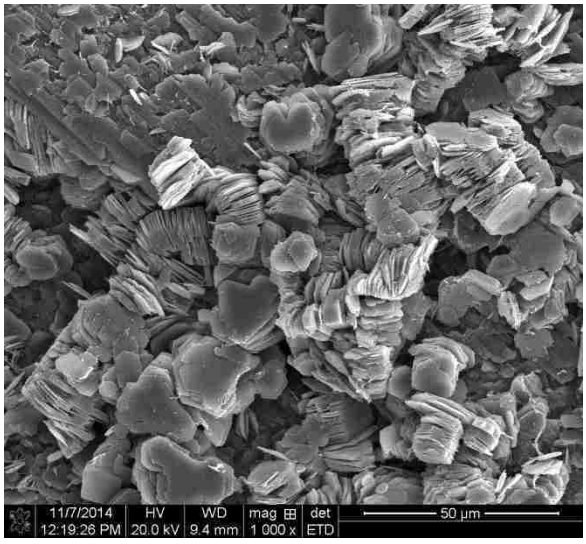

(b)

Figure 2-11. The SEM images for sample 62, (a) 500X, (b) 1000X, and (c) 3500X. Well-crystallized, authigenic kaolinite can be found in this sample.

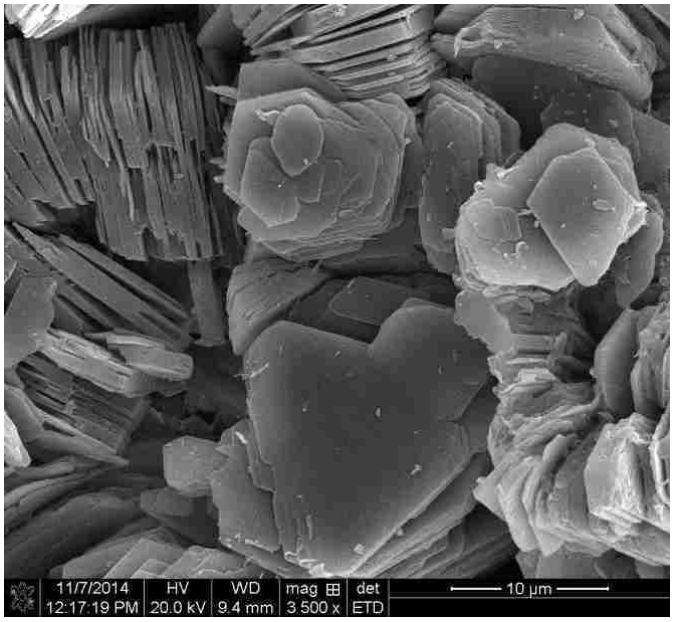

(c)

Figure 2-11 (continued). The SEM images for sample 62, (a) 500X, (b) 1000X, and (c) 3500X. Well-crystallized, authigenic kaolinite can be found in this sample.

2-5 Petrographic Microscope (Thin Section Analysis)

Thin section analysis was done with two goals: (1) investigating the type of minerals, (2) determining the quantitative mineralogy of samples. The thin section sample preparation was done by Weatherford Lab Co. A blue color epoxy was used to dye the void space. Alizarin Red-S dye has been used to identify carbonate minerals. The color of carbonate minerals are turned red using this indicator.

2-5-1 Type of minerals

Petrographic photographs were taken using a Leica DM 2500 P polarizing microscope with 10X, 20X, and 40X magnification. Quartz and feldspar are frequently seen in all samples. Both grains show first-order grey-white interference colors (Raith et al., 2011). These minerals are not easily distinguishable due to color and textural similarity. Quartz, however, can be identified from absence of cleavage and alteration (Federal Highway Administration, 1991). In this study, the shining bright white grains are recognized as quartz and white grains with corrosion trace are considered as feldspar (Fig. 2-12).

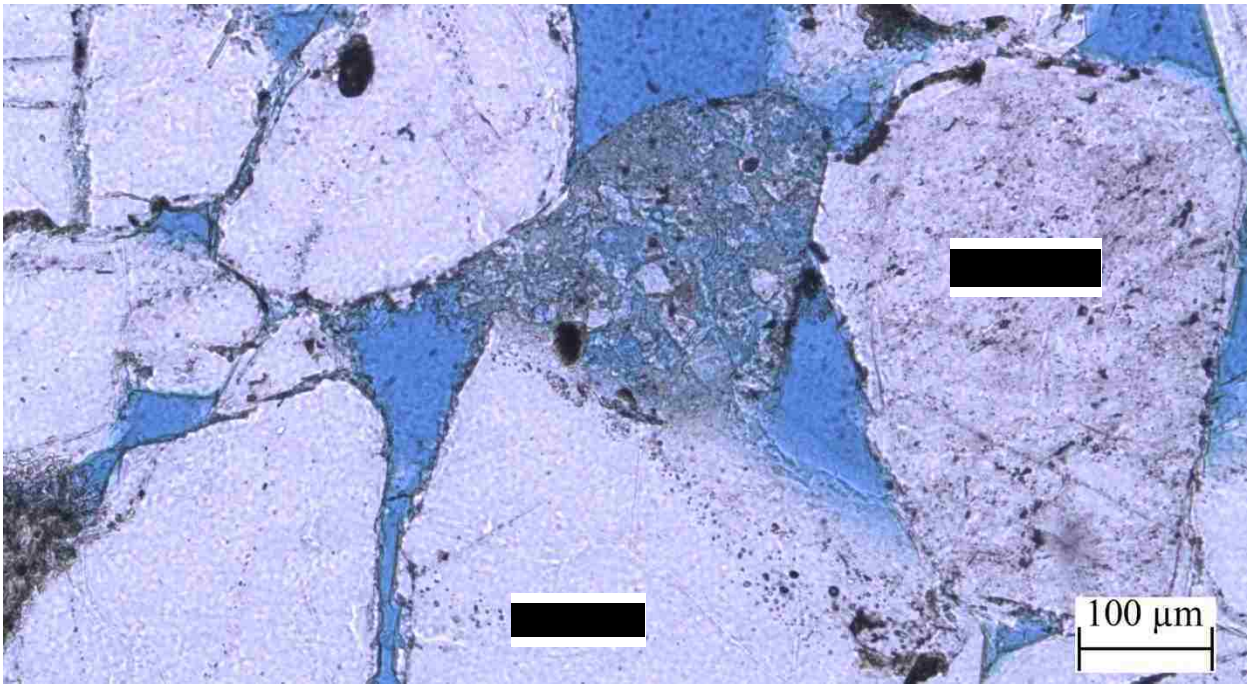

Figure 2-12. Quartz and feldspar grains in a petrographic image from sample 59. Brighter white grains were recognized as quartz and rusty white grains are feldspar.

Calcite is easily recognizable due to the added indicator to the thin section samples which turns the color of grains to red. This mineral is mostly seen in sample 59 and its amount is very low (Fig. 2-13).

Kaolinite is expected to convert to illite in this sampling depth and temperature (Lynch, 1996). Kaolinite crystals, however, are abundant in all samples. The lack of potassium in the adjacent environment is a possible reason for the lack of kaolinite to illite transformation. Kaolinite crystals, which fill the voids between grains, can be recognized from their nicely arranged book stack shape (Fig. 2-14).

Rock fragments are present as grains and can be seen in three different conditions: (1) unaltered rock fragments, (2) partly-altered rock fragments, and (3) completely-altered rock fragments. In the not-altered rock fragments (Fig. 2-15), the fragments still have their source rock minerals and have not been converted to a new type of mineral. Depending on the source rock, these fragments can have different mineralogy. In the partly-altered rock fragments (Fig. 2-16), the minerals of some fragments are altered to a new type of minerals while some parts of the grain stay unaltered. In the completely-altered rock fragments (Fig. 2-17), the full grains have

been transformed to a new type of mineral, which is a different type of clay. As it can be seen in Fig. 2-17, the rock fragment has been completely converted to kaolinite and just the shell of the grain is remained.

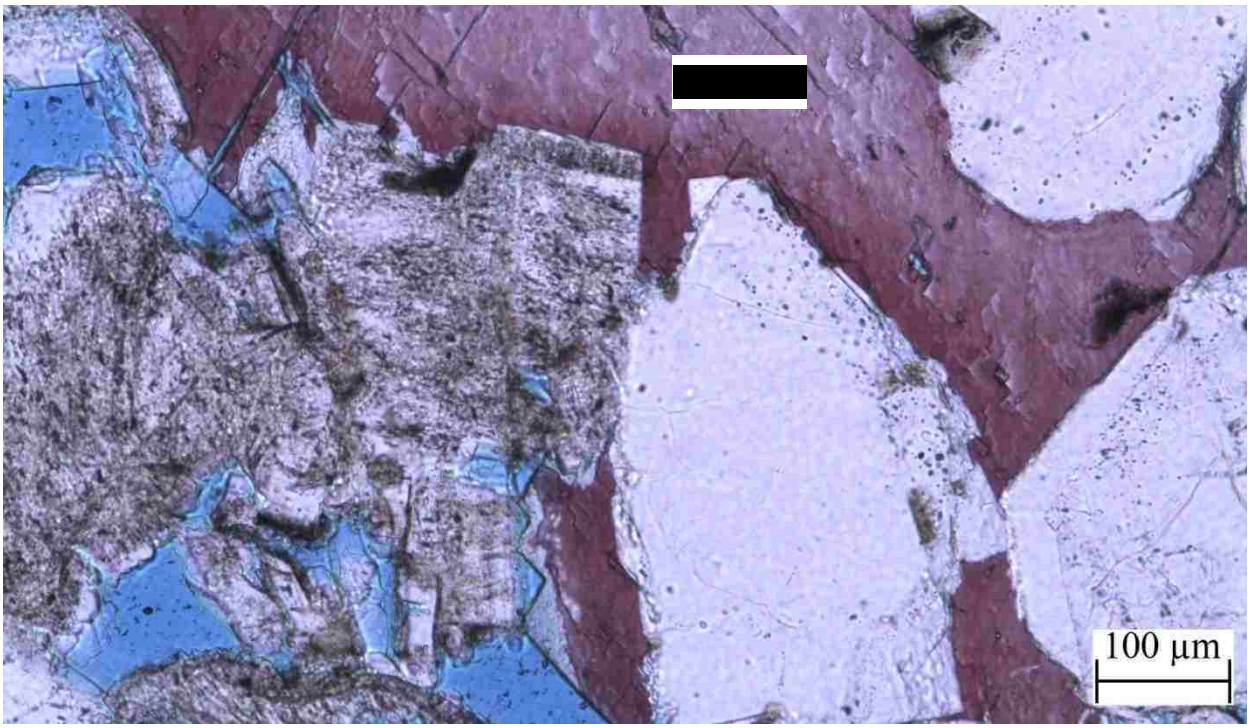

Figure 2-13. Calcite grains in a petrographic image from sample 59. The red color is because of the added indicator to the thin section samples.

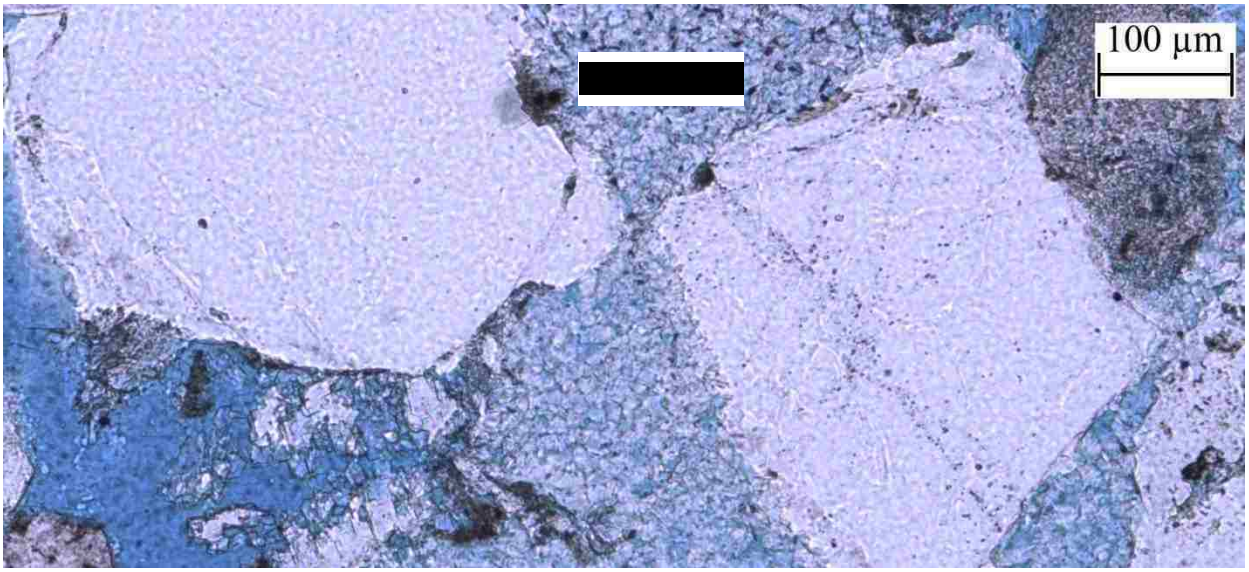

(a)

Figure 2-14. Kaolinite crystals in a petrographic image from sample (a) 62, (b) 61. Kaolinite can be recognized from its book stack shape.

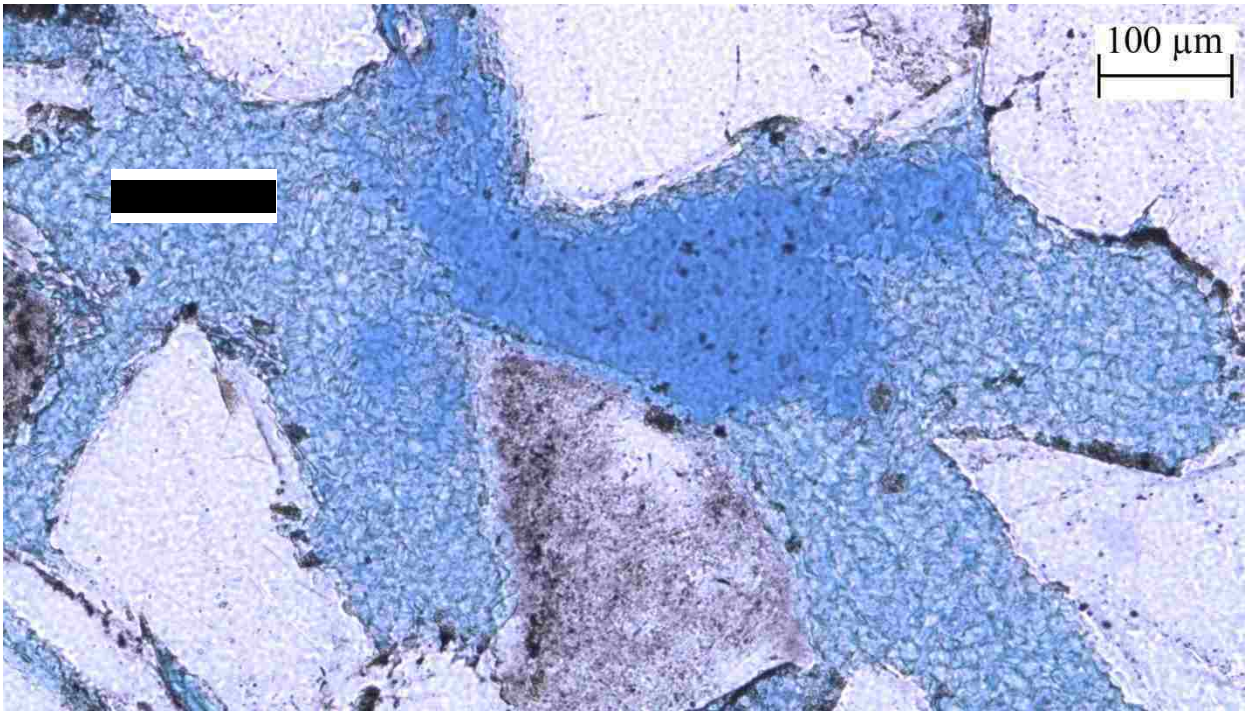

(b)

Figure 2-14 (continued). Kaolinite crystals in a petrographic image from sample (a) 61, (b) 62. Kaolinite can be recognized from its book stack shape.

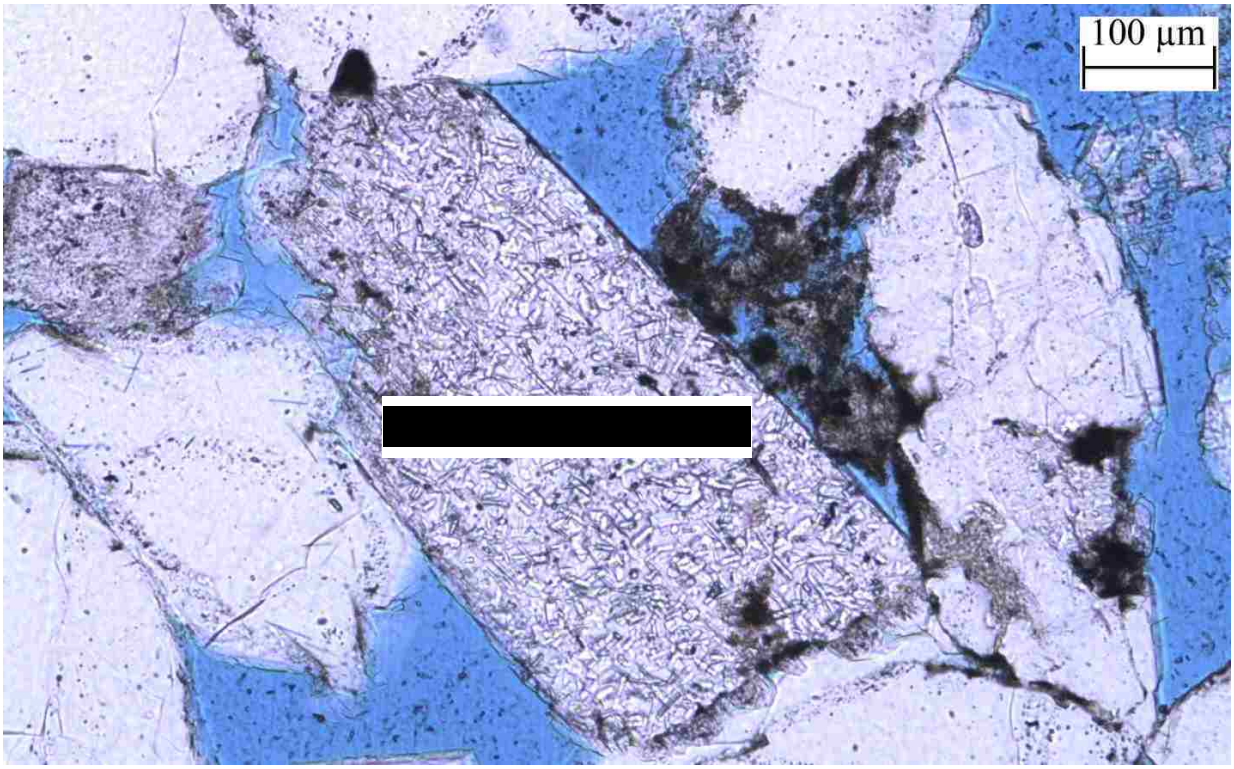

Figure 2-15. An unaltered rock fragment in a petrographic image from sample 61.

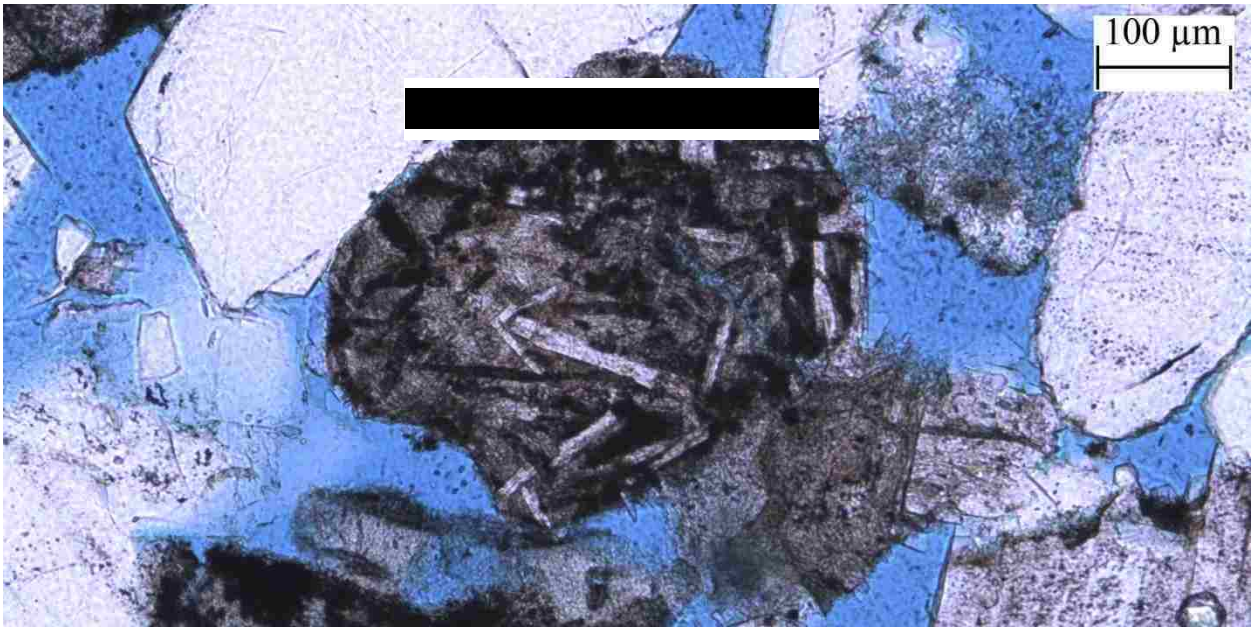

Figure 2-16. A partly-altered rock fragment in a petrographic image from sample 61.

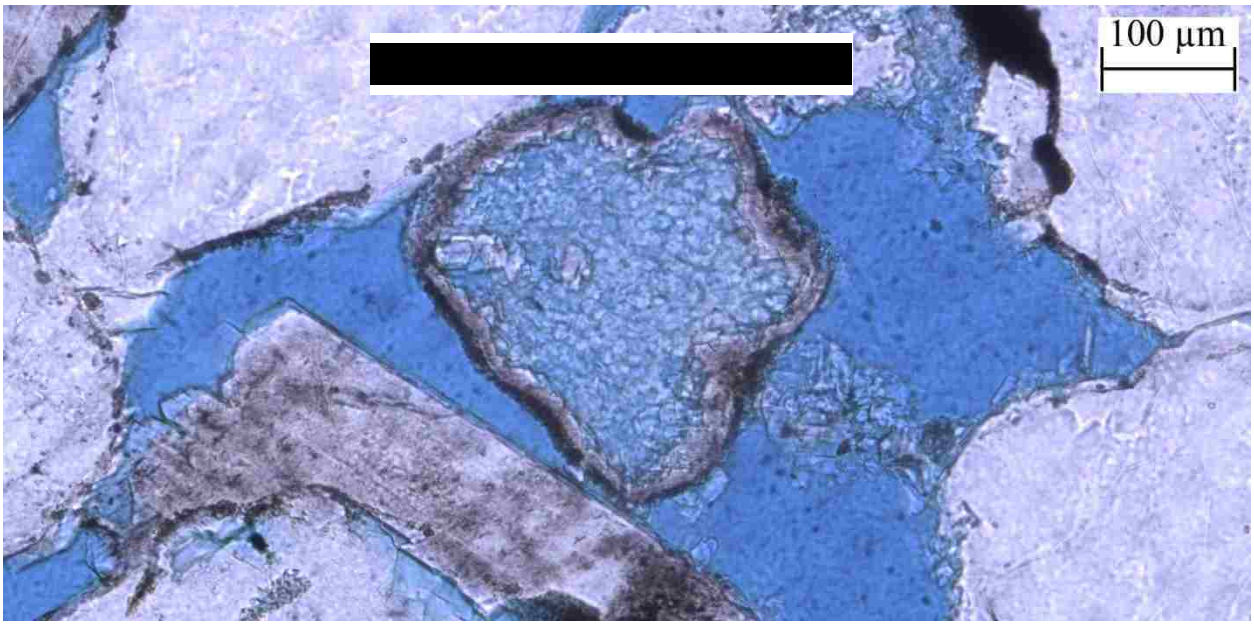

Figure 2-17. A completely-altered rock fragment in a petrographic image from sample 59. The rock fragment has been completely converted to kaolinite

As it mentioned in 2-4-1, chlorite forms a layer around some grains. Chlorite layers can also be seen in the thin section images (Fig. 2-18). Chlorite is seen in all three samples.

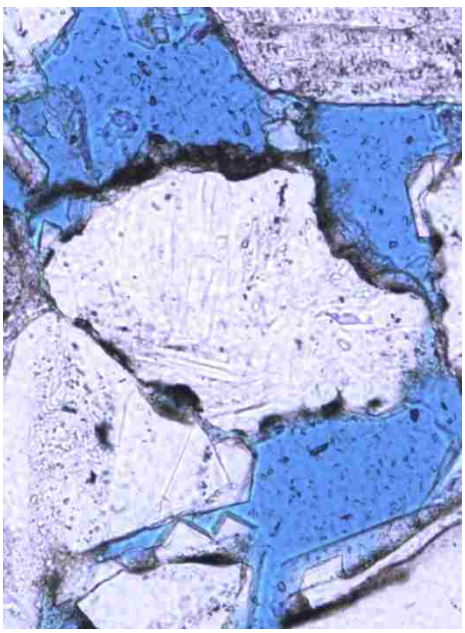

(a)

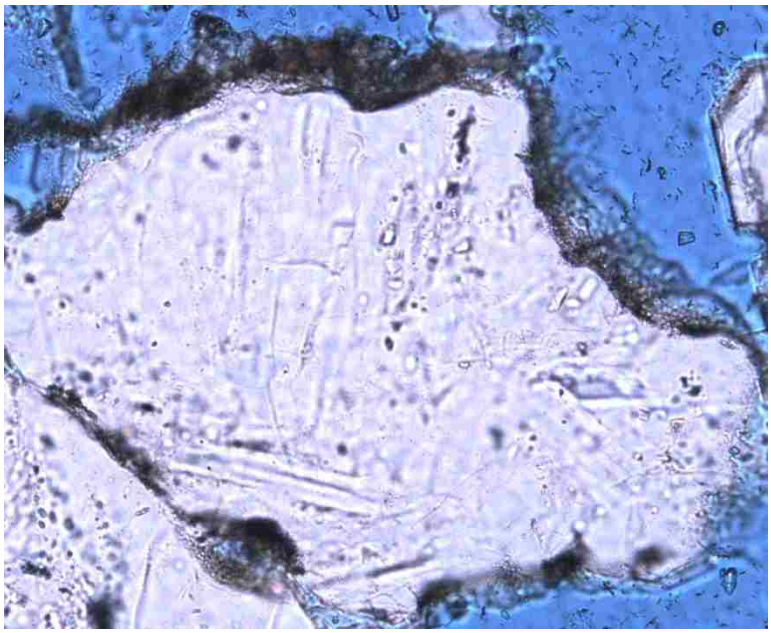

(b)

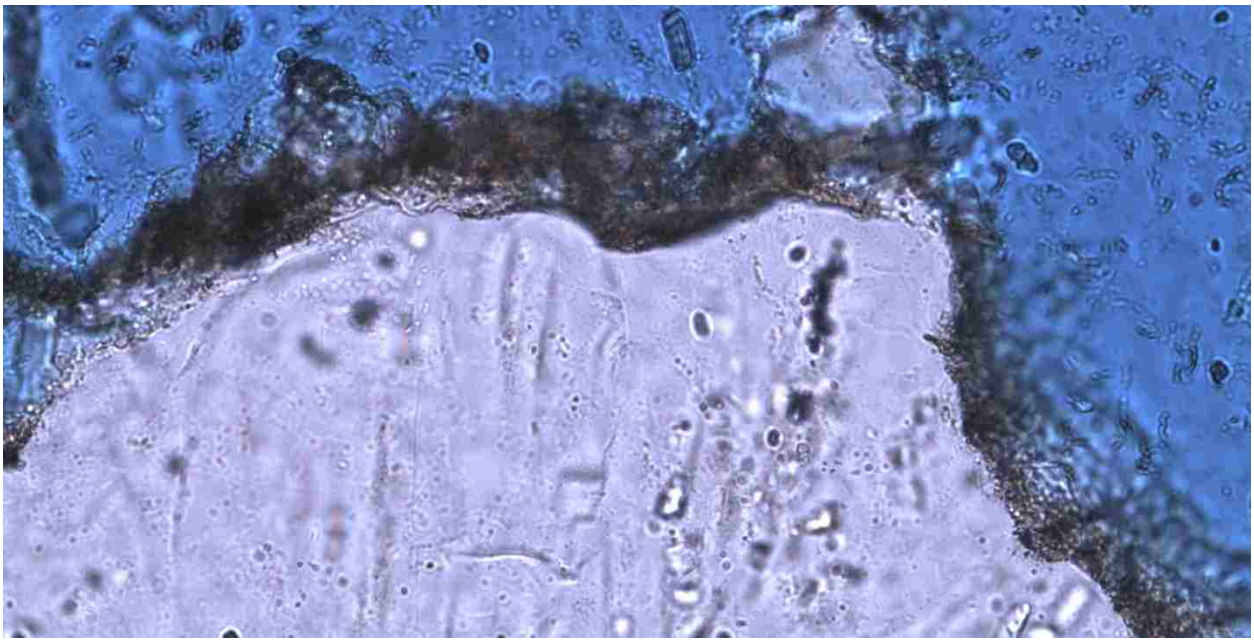

(c)

Figure 2-18. Chlorite layer on a quartz grain in a petrographic image from sample 61 with different magnifications; (a) 10X, (b) 20X, (c) 40X.

2-5-2 Quantitative mineralogy of samples

Determining the quantitative mineralogy of samples was done using the point counting technique. Point counting is based on the fact that there is a relationship between area percentages of various minerals in a section and their volume percentage in a rock. This relationship can be stated as follows. In a randomly chosen area of a rock, the ratio of the area of a particular mineral to the total area is an estimate of the volume percentage of that mineral in the rock (Carver, 1971).

In this study, the point counting has been done using the Glagolev-Chayes method (Carver, 1971). In this method, the intersection of the cross-hairs of microscope is taken as the point and the mineral beneath it is identified, and one count is recorded for that particular mineral. Then the thin section is moved a specific distance and the mineral at the new point is identified and recorded (Carver, 1971). The ratio of the counted points for a particular mineral to the total number of recorded points shows the volume percentage of that particular mineral. Six hundred points were recorded for each sample for an error of 1-2 percent at 50 percent confidence level, 2-4 percent at 95 percent confidence level. The result of the point counting is shown in Table 2-4. The completely altered rock fragments are counted as clay.

Table 2-4. The point counting results which shows the bulk volume percentage of each mineral.

Sample No.	Quartz	Feldspar	Calcite	Unaltered rock fragment	Kaolinite	Chlorite	Partly-altered rock fragment	Porosity
59	50.96	8.44	0.16	10.03	1.27	3.82	8.28	17.04
61	44.27	11.62	0.00	13.03	2.04	5.34	9.58	14.13
62	42.06	9.68	0.00	13.97	3.02	3.81	14.92	12.54

2-6 XRD

XRD was only done on the clay fraction of the samples to identify the type and quantity of the clay minerals. To separate the clay fraction from the rest of the rock sample, 10 ml ethanol was added to 2 grams of mortar ground samples and the solution placed in the micronizer machine (McCRONE micronizing mill). The micronizing process takes place for 3 minutes and sample particles are homogeneously grinded to micron size.

To disperse the clay particles, Na_3PO_4 solution was added to the samples and they were kept for at least 3.5 hours at room conditions. The suspended liquid is then collected from the samples and centrifuged with 12500 rpm for 35 minutes using a SORVALL LEGEND XT centrifuge machine. After centrifuge, the liquid part is discarded and the solid part is smeared on a glass plate to form the XRD samples.

The XRD tests were done with four different conditions of (1) air dried, (2) treated with ethylene glycol, (3) heated to 300 °C, and (4) heated to 550 °C, on each sample using a PANalytical Empyrean XRD machine. The smectite peak usually increases from 14 Å to 17 Å with ethylene glycol treatment. This peak collapses to 10 Å when heated to 400 °C. In this way, the presence and amount of smectite can be determined in the samples. The kaolinite peak is in 7 Å, which is destroyed when sample is heated to 550 °C. Heating chlorite to 550 °C increases the intensity of its main peak which is at 14 Å (Moore and Reynolds, 1989). The XRD graphs are shown in Fig. 2-19, which shows the XRD pattern for all four test conditions for each sample. Chlorite, kaolinite, illite, and smectite were identified in the studied samples, which their quantity is given in Table 2-5.

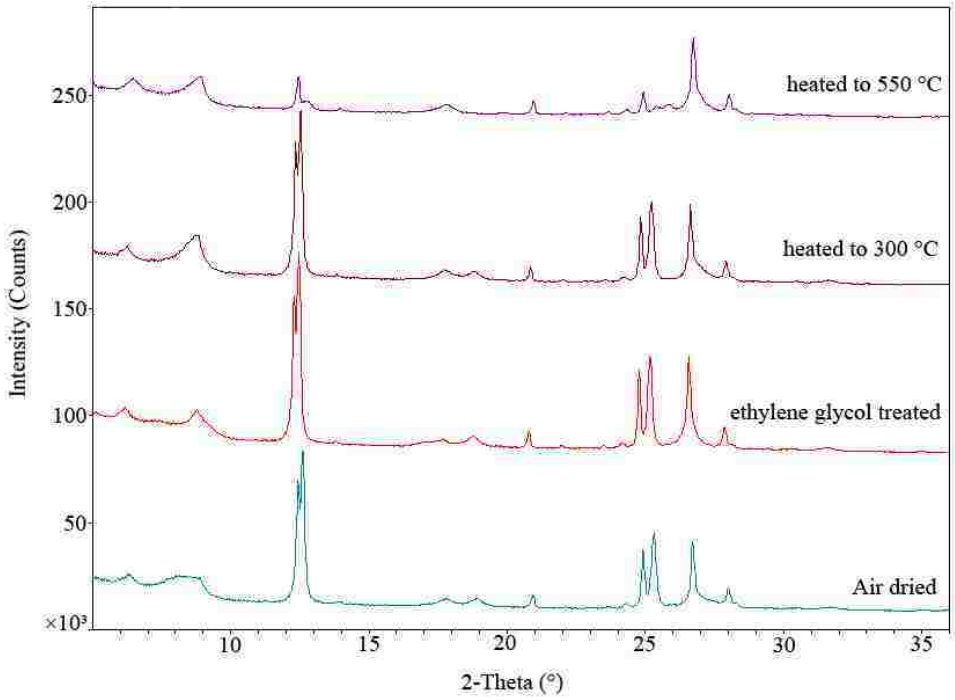

(a)

Figure 2-19. The XRD pattern for; (a) sample 59, (b) sample 61, (c) sample 62, for all four test conditions of air dried, treated with ethylene glycol, heated to 300 °C, and heated to 550 °C.

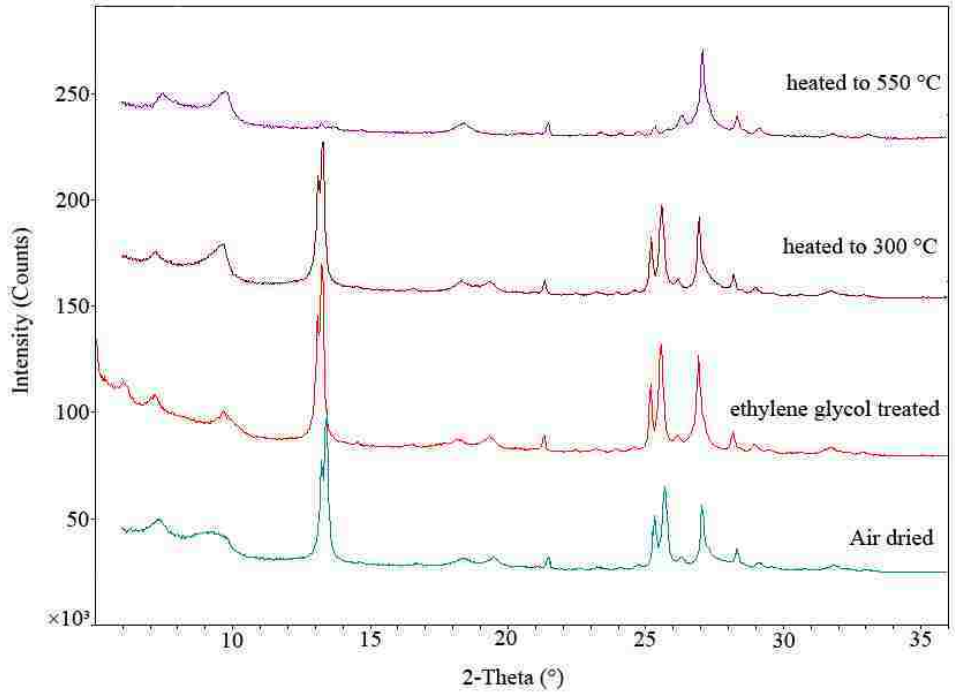

(b)

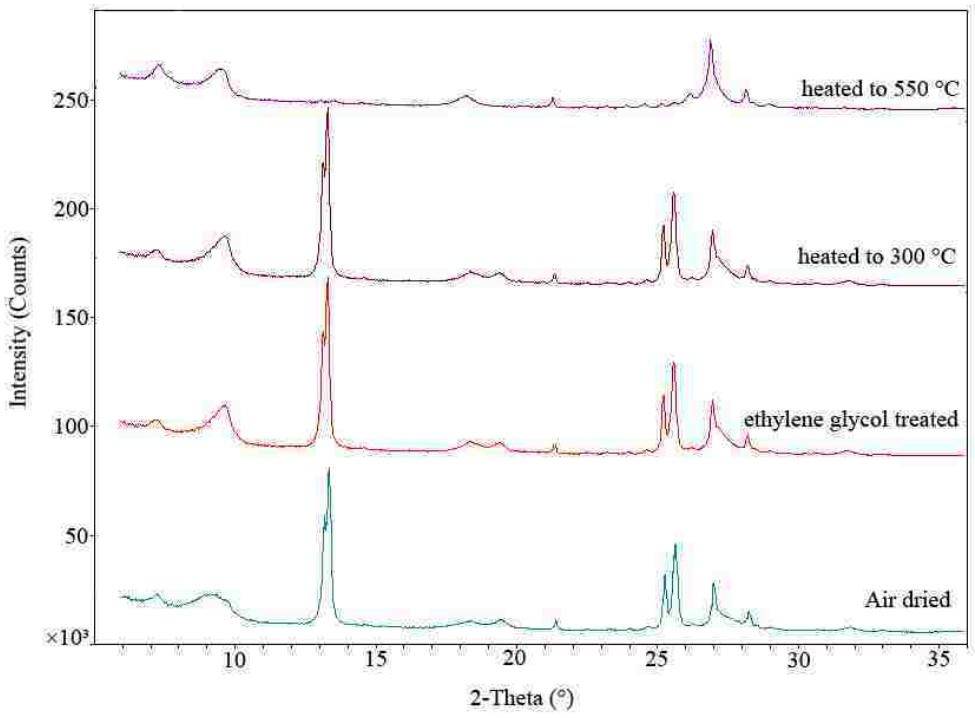

(c)

Figure 2-19 (continued). The XRD pattern for; (a) sample 59, (b) sample 61, (c) sample 62, for all four test conditions of air dried, treated with ethylene glycol, heated to 300 °C, and heated to 550 °C.

Table 2-5. The quantitative percentage of clay minerals in the studied samples.

Sample No.	Smectite	Chlorite	Illite	Kaolinite
59	0	50.42	22.38	27.20
61	5.12	57.61	15.81	21.46
62	1.06	57.15	20.50	21.29

2-7 Rock composition

The rock composition of the core samples was determined by combining the results of the rock characterization tests. The composition obtained from thin section point counting is used as the start point. It has been assumed that 50 percent of the partly-altered rock fragment section is clay and the other 50 percent is unaltered rock fragment. It also has been assumed that the unaltered rock fragment has the same rock composition of the total rock and its amount, hence, was proportionally added to the other rock sections. The rock mineral composition after these modifications is shown in Table 2-6.

Table 2-6. The rock composition after adding the rock fragment to the other parts.

Sample No.	Quartz	Feldspar	Calcite	Clay	Porosity
59	63.11	10.45	0.18	9.24	17.04
61	59.56	14.15	0.00	12.17	14.13
62	60.45	12.73	0.00	14.29	12.54

The porosity obtained from the fluid saturation porosity test (Table 2-2) is higher than the porosity achieved by thin section point counting. The reason is that in the fluid saturation measurements both micro porosity and macro porosity are taken into account, however, in the point counting the micro porosity of the clay section cannot be observed. In other words, some fraction of the clay portion in the point counting results is pore space and should be considered as porosity. Therefore, the fluid saturation measurements results were considered as porosity and the difference between these results and point counting porosity was deducted from the clay amount. After the porosity adjustment and applying the results of XRD analysis, the total rock composition of the core samples will be as Table 2-7.

Table 2-7. The rock composition of the studied core samples.

Sample No.	Quartz	Feldspar	Calcite	Smectite	Chlorite	Illite	Kaolinite	Porosity
59	63.11	10.45	0.18	0	2.82	1.25	1.52	20.66
61	59.56	14.15	0.00	0.23	2.70	0.74	1.00	21.62
62	60.45	12.73	0.00	0.08	4.55	1.63	1.69	18.87

2-8 Rock composition from previous studies

In addition to the real core sample composition, a rock composition was determined based on studies performed by other researchers on the Frio formation in Texas Gulf Coast, Chocolate bayou, with similar reservoir temperatures and depths. A study in the Frio formation conducted by Land and Milliken (1981) in the Chocolate Bayou Field, Brazoria County, Texas, shows that 65 volumetric percent of the rock consists of mineral grains and the remainder is pore space and diagenetic products. The grains include quartz (40 percent), albite (10 percent) and rock fragments (15 percent). The subsurface temperature is approximately 150 ºC.

Lynch (1996) studied the Frio sandstone diagenesis near Corpus Christi, Texas. This study showed that the illite/smectite matrix (4.4 percent), chlorite (3.2 percent), quartz overgrowths (1.5 percent), calcite (11 percent) and kaolinite (1.3 percent) are the diagenetic products in the Frio sandstone. Percentages are bulk volume. At the target depth, around 14,000 ft., no kaolinite was found. The absence of kaolinite in the most deeply buried sandstones is probably the result of diagenetic loss of kaolinite in favor of highly illitic I/S, chlorite, and albite (Lynch, 1996) at higher temperatures. In another study on the smectite to illite reaction in Frio shale, Lynch (1997) showed that the illite and smectite percentage in illite/smectite matrix is 80 and 20 percent, respectively. Based on these studies and assuming that the composition of the rock fragment is the same of the remainder of the reservoir sandstone, the theoretical rock composition, which is based on the previous studies, is presented in Table 2-8. For comparison, the rock composition of sample 59 is also given in Table 2-8.

2-9 CT scan imaging

As it stated in the introduction, in this research pore network modeling was utilized to quantify the permeability changes due to simulated geochemical alterations. The first step in building a pore network model is to take CT scan images from all three samples. For this study,

the micro-CT imaging was done at the GSECARS 13-BMD beamline at the Advanced Photon Source (Argonne National Laboratory) by Dr. Clinton Willson and Godfrey Mills. Cylindrical samples, with the dimension of 7 mm diameter and 15 mm height, for micro-CT scan were drilled from the larger core samples. One core from each sample was imaged at an energy of ~33 keV using 900 projections and a voxel resolution of 4.1 micron. The micro-CT scan image for sample 59 is shown in Fig. 2-20. Image processing and pore network generation are discussed in more detail in chapter 4.

Table 2-8. The rock composition by volume percentage, assumed based on the previous studies. Illite/smectite mixed layer has been stated as end members.

	Composition from previous studies	Core sample 59
Pore volume	17.4	20.66
Quartz	47.9	63.11
Albite	11.5	10.45
Calcite	12.7	0.18
Illite	5.6	1.25
Smectite	1.1	0
Chlorite	3.8	2.82
Kaolinite	0	1.52

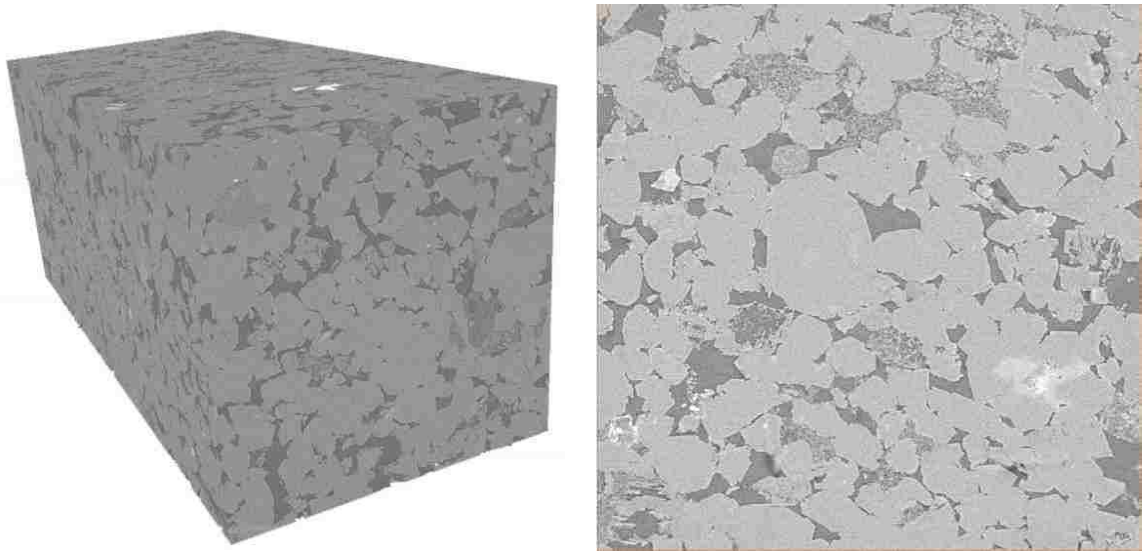

(a) (b)

Figure 2-20. The CT scan image of sample 59; (a) 3D, (b) 2D. The image dimensions are 1100×1100×2439 voxels which means the physical dimensions are 4.51×4.51×9.99 mm.

Chapter 3
Geochemical Modeling

3-1 Introduction

The first part of this research was to anticipate the possible geochemical reactions and alterations in the studied geothermal reservoir. The target formation of this reservoir consists of a thick bed of Camerina A sand, a member of the Frio formation. In order to fulfill this objective, the geochemical reactions of rock-brine were modeled utilizing a geochemical modeling software.

Two sets of rock and brine compositions were used to model the potential geochemical interactions. A brine composition from Chocolate Bayou, TX, (Table 3-1), with the rock composition of the three core samples from Pleasant bayou, TX, (Table 2-7), were used for the first set of the reaction modeling. A brine composition from Vermilion Parish, LA, (Table 3-2), with a rock composition inferred from the Frio Formation at similar depths and temperatures from other wells (Table 2-8) was used for the second set of the geochemical modeling. Kinetics modeling and sensitivity analysis were also performed on this second set of brine and rock compositions.

3-2 Previous work

Possible water-rock reactions in South Louisiana were studied by Ausburn and Hanor (2013). They used water sample data from six oil and gas fields located in Vermilion, Iberia, and St. Mary parishes, Louisiana. In their study, water compositions were found to be partially buffered by calcite/dolomite and chalcedony. It also was found that there is potential for barite precipitation due to mixing of barium and sulfate rich waters (Ausburn and Hanor, 2013).

The impact of brine-rock interactions on geothermal reservoir properties has been investigated in a study by Safari-Zanjani et al., (2013). In that study, interactions between

geothermal fluid and reservoir rocks in the West Hackberry field, Cameron Parish, Louisiana were examined using geochemical modeling. A porosity change about 5 percent was anticipated by geochemical reaction models (Safari-Zanjani et al., 2013).

3-3 Brine composition

The brine composition (Table 3-1) obtained from the USGS produced water database (Blondes et al., 2014), for Chocolate bayou, was used to model the reaction with the core sample rock compositions (Table 2-7).

The brine composition reported by Southern Petroleum Laboratories (Dobson et al., 1980), collected from the Beulah Simon No.2, Vermilion Parish, Louisiana, (Table 3-2), was used for modeling the geochemical reactions with the assumed rock composition from previous studies (Table 2-8).

Table 3-1. The brine composition of Chocolate bayou, Texas. All concentrations are in mg/l (USGS produced water database).

pH	6.3
Total Dissolved Solids	68,500
Calcium (Ca)	2,000
Magnesium (Mg)	235
Bicarbonate (HCO_3)	520
Chloride (Cl)	40,500
Total Iron (Fe)	8
Manganese (Mn)	2.7
Boron (B)	30
Ammonium (NH4)	26
Sodium (Na)	24,000
Potassium (K)	300
Rubidium (Rb)	0.8
Strontium (Sr)	380
Sulfate (SO_4)	0.6

Table 3-2. The brine composition of Cossinade field, Vermilion Parish, Louisiana. All concentrations are in mg/l (Dobson et al., 1980).

Density (gr/ml)	1.066
pH	6.61
Total Dissolved Solids	103,925
Calcium	7,869
Magnesium	910
Bicarbonate (HCO_3)	606
Chloride (Cl)	50,300
Total Iron (Fe)	33
Dissolved Silicate (SiO_2)	92
Boron (B)	89.6
Lead (Pb)	7.73
Sodium (Na)	32,190
Potassium (K)	454
Barium (Ba)	30.4
Sulfate (SO_4)	444

3-4 Simulation of fluid-rock interaction

The modeling software package, Geochemist's Workbench, developed by Bethke (2008) has been used in this research. This software can model chemical reactions, trace reaction processes, model reactive transport and plot the results of these calculations.

Geochemist's Workbench (GWB) is able to use different thermodynamic databases. Each database contains the properties of minerals, aqueous species, and gases, equilibrium constants for reactions to form these species, and data required to calculate activity coefficients (Bethke and Yeakel, 2012). The default dataset employed by GWB is the LLNL thermodynamic database. This dataset was compiled by the geochemical modeling group at Lawrence Livermore National Laboratories (LLNL). The temperature range in LLNL thermodynamic dataset spans from 0 to 300 °C and it contains data related to high temperature minerals like saponite and nontronite. The bulk of the modeling was performed using this dataset.

GWB is also able to employ the database designed by the U.S. Geological Survey for the PHREEQC software package. The PHREEQC database does not include saponite and nontronite minerals and only goes up to 100 °C. This dataset was utilized for comparison purposes.

3-5 Equilibrium modeling process

The rock-brine reactions have been modeled with both titration and kinetic paths. In the titration reaction path, the program repeatedly adds a small aliquot of reactants and then recalculates the equilibrium state the system. There is no time component in this reaction path. In the kinetic reaction path, kinetic rate laws control the rates at which reactions proceed (Bethke and Yeakel, 2012).

In accordance with the planned heat exchanger specifications (Feng et al., 2015), the initial and final temperatures of the brine as it travels through the exchanger have been assumed to be 130 and 100 °C, respectively. To investigate the precipitation risk inside the heat exchanger brine was assumed to cool from 130 to 100 °C.

To combine geochemical reaction with brine flow in the reservoir, rock-brine geochemical reactions were modeled in consecutive steps. After the earliest rock-brine interaction, the resulting minerals are separated and the next reaction step happens between the minerals remaining from previous reaction step and the initial brine composition (i.e. the brine composition does not change). Figure 3-1 shows a schematic drawing for this modeling method. Reactions have been modeled for five steps, since the results for total minerals in the system show only minor changes after five consecutive steps. Chemical equilibrium between the brine and the minerals occurs at each step.

The first rock-brine interaction happens in the vicinity of the heat exchanger where brine at 100 °C encounters reservoir rock with 130 °C. Assuming a constant temperature of 130°C for the reservoir, the subsequent rock-brine interactions happen with constant temperature of 130 °C. Kinetic modeling is discussed in section 3-12.

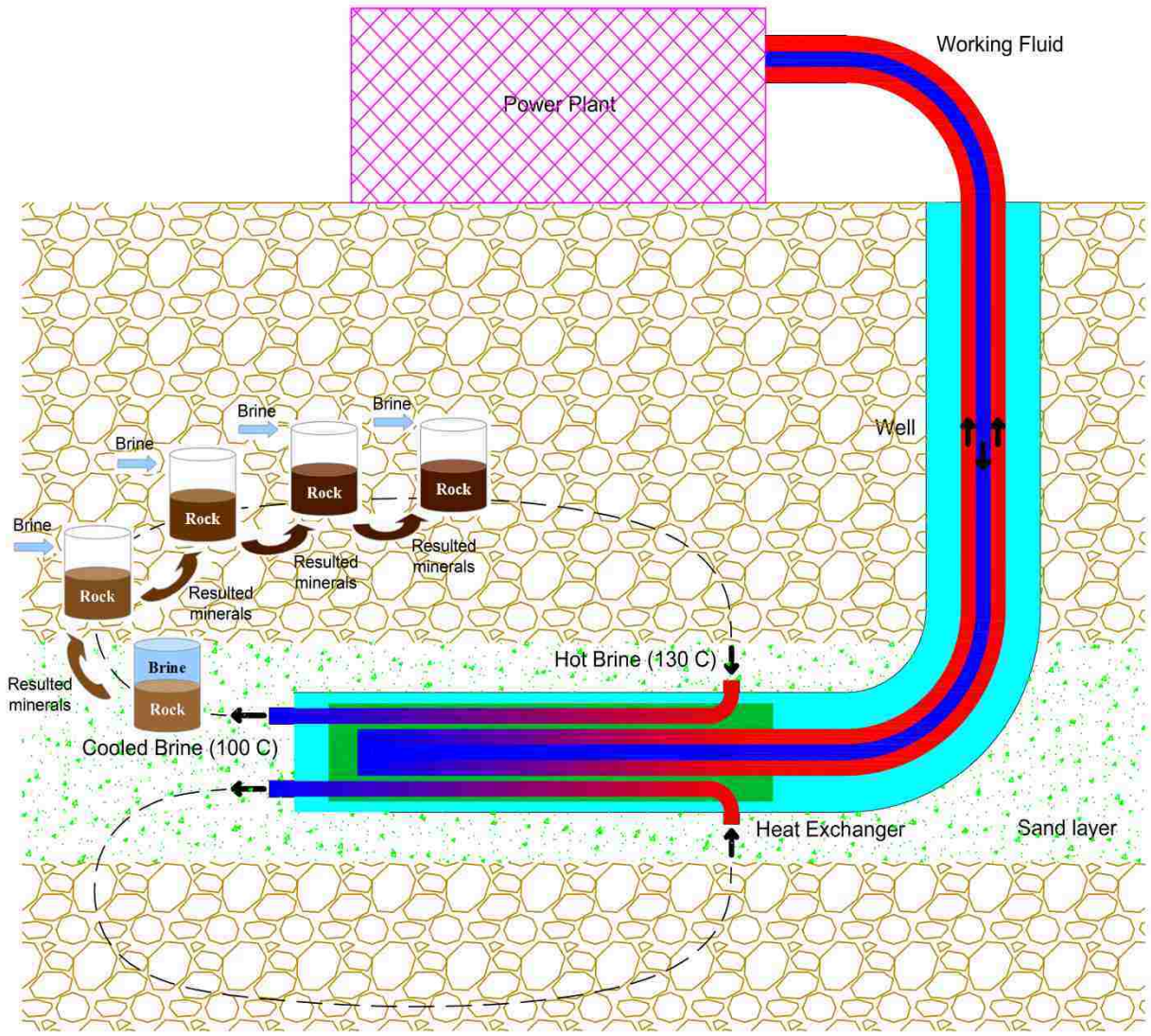

Figure 3-1. Consecutive steps in rock-brine geochemical reactions models. After the earliest rock-brine interaction, the resulting minerals are separated and the next reaction step happens between the minerals resulting from the last reaction step and the initial brine composition.

3-6 Reaction of cooled brine with reservoir rock

Geochemical reactions between rock and brine have been modeled in five consecutive steps as shown in Fig. 3-1. Although two sets of rock and brine compositions were used to model geochemical reactions, only the results belong to the rock composition shown in Table 2-8 (composition from previous studies) and the brine composition of Cossinade field, Vermilion Parish, Louisiana, Table 3-2, is shown in this section. The changes in the mass of major minerals with reaction steps are shown in Fig. 3-2. Run A is the base case for the system and consists of

100 °C rising to 130 °C after the first titration cell. Temperature of the reaction models stays constant at 130 °C for the subsequent rock-brine interactions. Considering the 17.4 percent initial reservoir porosity, the rock to brine volume ratio is 4.75. Minerals shown in step 0 of this graph indicate the initial rock composition.

The main change in rock composition can be seen in the first reaction step (Fig. 3-2). In this step, the brine temperature rises from 100 °C to reservoir temperature, 130 °C. Quartz (not shown here), which is the dominant mineral in the initial rock composition, shows a slight increase after five reactions increasing from an initial value of 8046 g to 8227 g after the fifth reaction. Calcite also shows no noticeable change, decreasing from an initial value of 2183 g to 2177 g after the fifth reaction. Albite, however, shows a sharp drop in the first reaction step and this reduction is continued until the last reaction step. In the first rock-brine interaction, illite, smectite, and chlorite are transformed to muscovite, saponite-Ca, nontronit-Ca and paragonite.

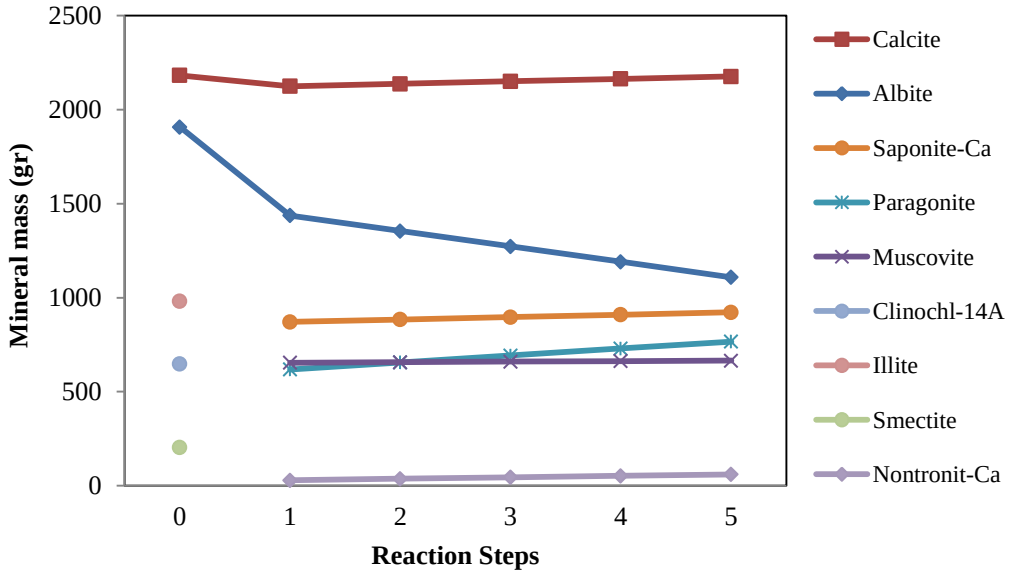

Figure 3-2. The changes in major minerals mass with reaction steps in run A. Reaction step 0 shows the initial rock composition. The main change happens in the first reaction where the temperature changes from 100 to 130 °C. In steps from 2 to 5, temperature is constant and equal to 130 °C.

Illite is a non-expanding, clay-sized, micaceous mineral which structurally is similar to muscovite. Transformation of illite to muscovite has been shown by many studies (Gharrabi et al. 1998, Hunziker et al., 1986, Verdel et al., 2012). Muscovite, $KAl_3Si_3O_{10}(OH)_2$, and paragonite, $NaAl_3Si_3O_{10}(OH)_2$, both are micaceous minerals. The crystal structures of paragonite and muscovite are nearly identical (Zen and Albee, 1964). Saponite is the most abundant of the trioctahedral smectites and is found in a number of Mg-rich geologic environments (Whitney, 1983). Nontronite-Ca is the iron-rich member of the smectite group. In the first reaction step, original smectite has been converted to saponite-Ca and nontronite-Ca.

As discussed above, the models show the formation of pure end member layer silicates, such as saponite and paragonite. Different assumptions, including the thermodynamic data base used, result in similar predictions, although the specific pure end members may vary (see appendix B).

We believe that simulated alteration of the initial clay mineral assemblage of chlorite and illite smectite, as well as albite, to clay minerals that more closely resemble the pure end members is likely due to the lower free energy state which would result. However, we do not believe that at these temperatures, rather than the metamorphic temperatures at which the pure end members are found in nature, the transformation will be complete. Rather, new clay minerals that are closer to but not completely represented by the pure end members will be formed. In this chapter, we refer to the formation of muscovite, paragonite, talc, etc. but these are simply proxies for the actual clay minerals formed.

A question that has to be answered is whether the system was initially in equilibrium with the brine and minerals shown in Tables 2-8 and 3-2. To address this question, the brine-rock reactions were modeled with a similar approach but this time without changing temperature. Temperature in all reaction steps was constant and equal to reservoir temperature (130 °C). The results of this case, which is recognized as run “B” here, have been shown in Fig. 3-3.

As it can be seen, results for the constant temperature model (Fig. 3-3) are similar to results obtained from the temperature reduction model (Fig. 3-2). It can be concluded that in addition to temperature change, pursuing a lower free energy state is a reason for the predicted mineral transformations.

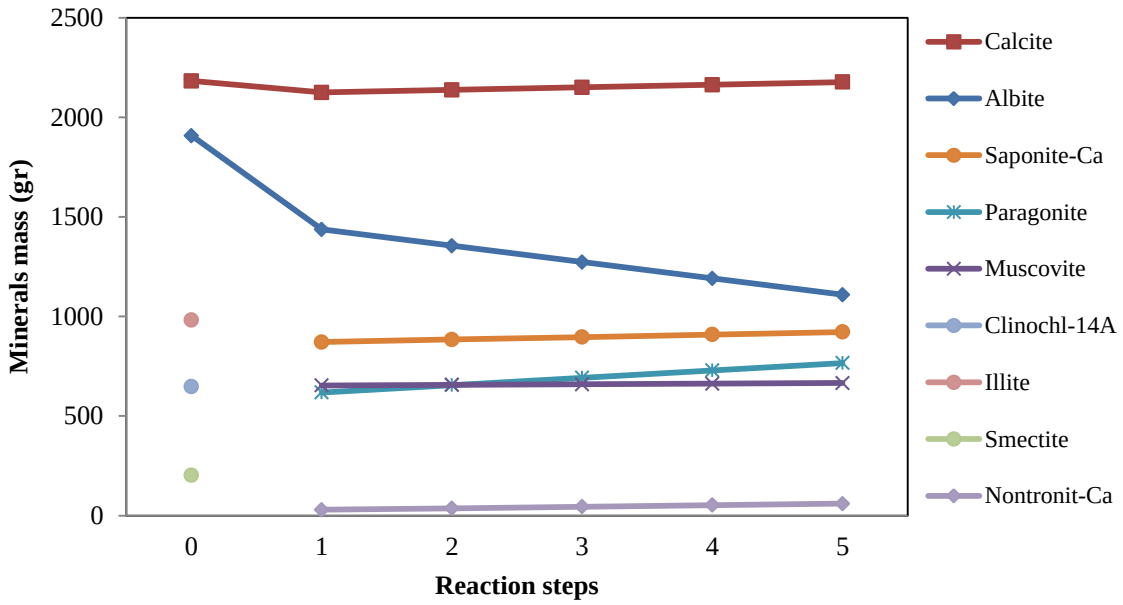

Figure 3-3. The changes in major minerals mass with reaction steps in run B. Reaction step 0 shows the initial rock composition. In all steps temperature is constant and equal to 130 °C.

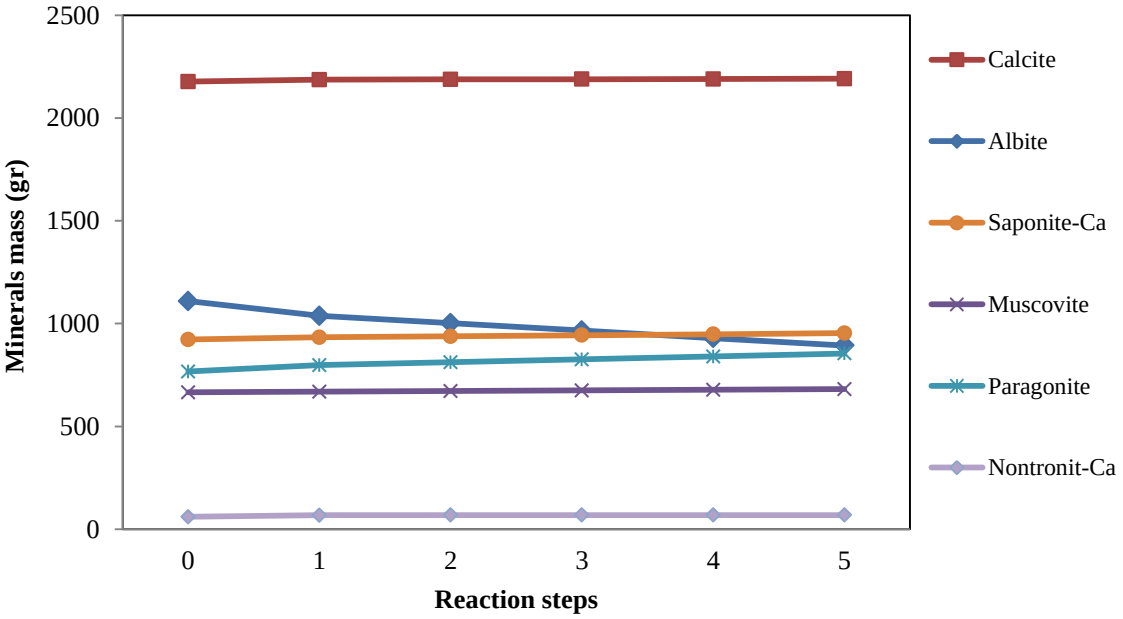

Figure 3-4. The changes in major minerals mass with reaction steps in run C. Reaction step 0 shows the initial rock composition which is the final rock composition in run B. Temperature increases from 100 to 130 °C in first reaction step and stays constant, 130 °C, in the rest of reaction steps.

For further investigation, the final rock composition (rock composition after five consecutive reaction steps) in run B was assumed as the initial rock composition and the rock-brine interaction was modeled with the temperature increasing from 100 to 130 °C. In other words, the final rock composition in run B has been assumed to be close to equilibrium and reactions from that point have been modeled and called run C. The results for this case (run C) have been shown in Fig. 3-4. In this run minerals show small changes. A decrease in albite and an increase in paragonite can still be seen in these results.

3-7 Changes in the amount of clay minerals

Clay minerals usually have negative impact on permeability. Change in clay amount, therefore, is evaluated precisely here. Two sets of modeling have been done in this part. The first set is modeled between the brine composition of Chocolate bayou (Table 3-1) and the rock composition of the core samples (Table 2-7). The second set, however, is modeled between the brine composition of Vermilion Parish (Table 3-2) and the rock composition from previous studies (Table 2-8).

The bulk volume percentage of clay minerals was calculated from their mass from the geochemical models and their grain density. Changes in clay amounts in core sample 59 are shown here (Fig 3-5-a). In this sample the initial clay portion, which consist of illite, kaolinite, and chlorite, is 5.59 percent. Clay volume percentage is increased to 7.86 percent after five reaction steps. Most of this clay is in the illite-like family. Similar results were obtained for the samples 61 and 62 (not shown here). In sample 61, the clay amount changes from 4.67 to 7.16 percent. This change for sample 62 is from 7.95 to 12.03 percent.

In the rock composition from previous studies (Table 2-8), the clay portion forms 10.5 percent of total initial rock volume (Fig 3-5-b). This volume percentage is increased to 13.4 percent after five reaction steps. Most of the initial clay minerals are chlorite and illite which are non-expandable minerals and the share of expandable mineral, smectite, is low. After reactions, however, a considerable amount of expandable clay minerals, saponite-Ca and nontronite-Ca, are formed (Fig. 3-5-b). Transformation of chlorite to smectite has been observed in previous studies (e.g. Senkayi et al., 1981).

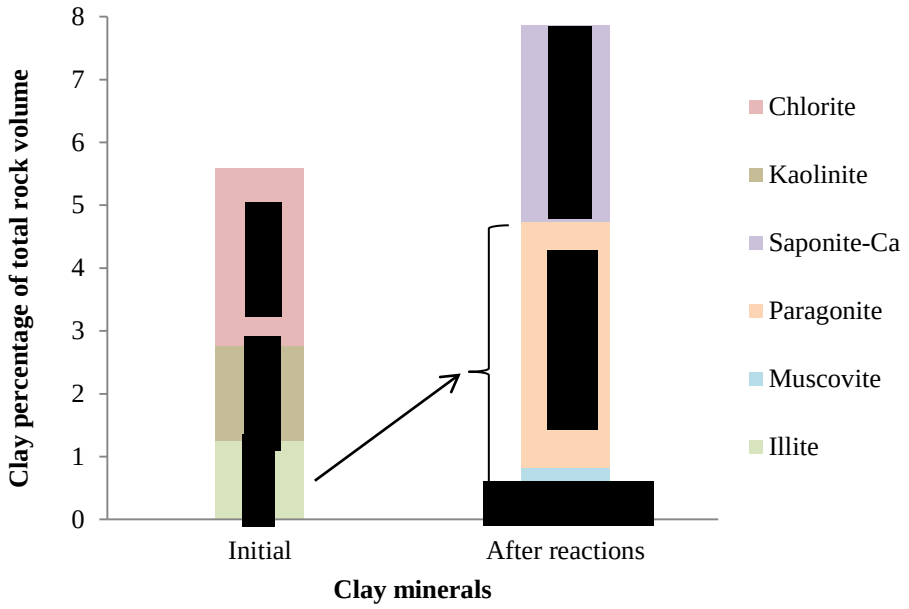

(a)

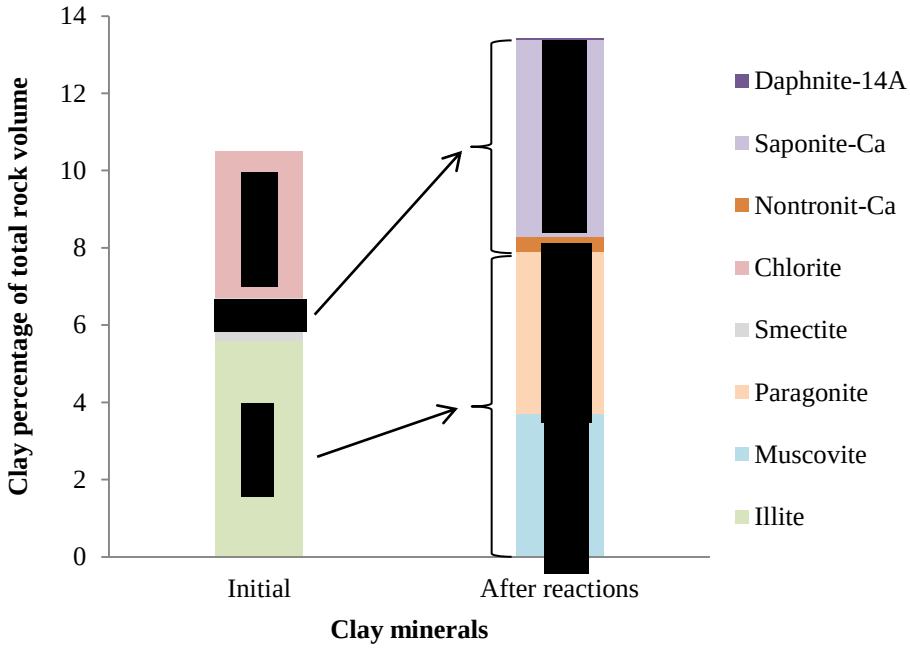

(b)

Figure 3-5. The changes in clay volume percentage after five reaction steps; (a) Chocolate Bayou, core sample 59, (b) rock composition from previous studies. About 2.3 and 3 percent increase can be seen in the clay portion in a and b, respectively. Clay conversions also lead to increase in the amount of more expandable clay minerals.

Albite transformation to clay minerals is the reason for the increase in the clay content. Albite is a member of the feldspar family. The transformation of the plagioclase feldspar to clay minerals has also been reported in previous studies (e.g. Frank-Kamenetskii, 1980). The amount of albite decreases continuously in all runs in different steps. In run with Vermilion Parish data the amount of albite decreases from an initial mass of 1908 grams to 1109 grams. Assuming that aluminum is conserved in all reactions, tracking the location of aluminum in the reaction steps is a useful way to illustrate the change in aluminum silicate minerals. As it can be seen in Fig. 3-6, in reaction steps 1 to 5 the total amount of albite decreases while paragonite increases. Other Al-contained minerals have small changes after the first step.

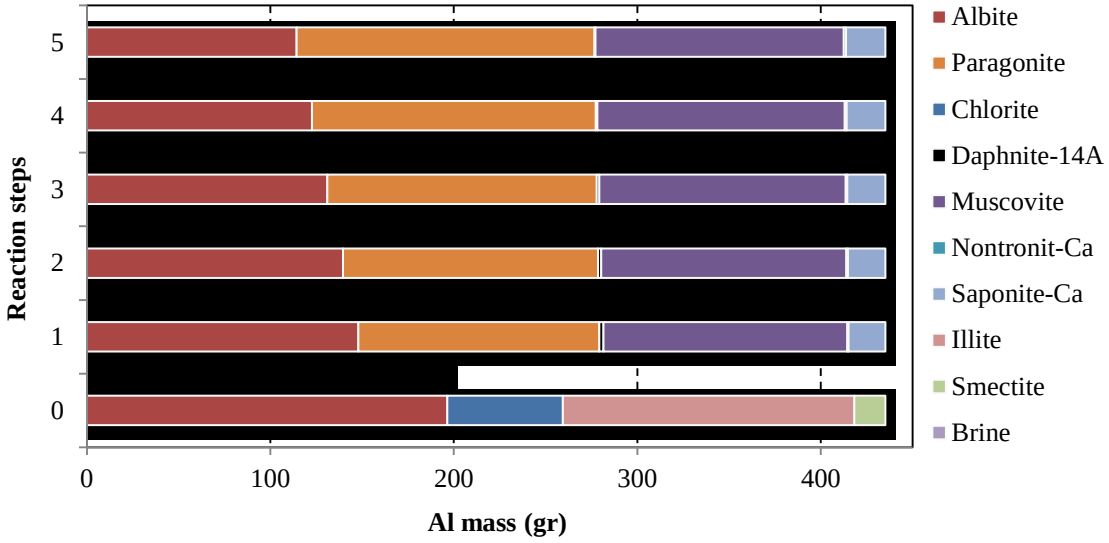

Figure 3-6. The change in total Al mass in run A. In all reaction steps the total amount of albite decreases while paragonite increases. Other Al-contained minerals have small changes after the first step.

Our interpretation of these results is that the combination of repeatedly exposing the rock to fresh brine, and a change in the brine temperature from 100 to 130 °C results in two changes. The first is alteration of smectite, illite and chlorite to purer layer silicates, represented by saponite, nontronite, paragonite and muscovite. The second change is dissolution of albite and the formation of additional paragonite, a sodium-bearing sheet silicate, as well as additional quartz. The combination of these two changes results in an around 3 percent increase in clay volume.

To validate these results, modeling was performed on the brine composition from Vermilion parish, LA, and the rock composition from previous studies (Table 2-8) by varying the change in temperature, the pH, HCO_3 concentration, and sodium concentration in the brine, the amount of albite initially present and the amount of initial clay present. Modeling was also performed using the PHREEQC thermodynamic data base in place of the LLNL data base. In addition, runs were made in which the formation of saponite, nontronite and paragonite was prevented.

The details of these runs are presented in the Appendices A and B. With two exceptions, all the runs showed a similar increase in clay content from approximately 10 to 13 percent, although the specific clay minerals formed varied.

The two exceptions were:

A. A run made with twice the Na^+ concentration present compared to the initial case (64,380 mg/l). In this case, the alteration of albite to paragonite did not occur, as the higher Na^+ concentration stabilized the albite. The total clay concentration decreased from 10 to 9 percent and the amount of albite increased, reflecting a reversal of the reaction albite → paragonite.
B. A run was made which prevented the formation of paragonite. In this case, no sodium containing layer silicate formed, and the amount of albite stayed constant. The volume of total clay only increased to from 10 to11 percent.

The situation in case A could be expected to occur in the vicinity of salt domes in the area studied, and indicates that the concentration of sodium in the brine could be a variable affecting the suitability of different locations for projects of this type. The exception is case B is not believed to be a realistic scenario – the exclusion of any sodium-bearing sheet silicates is not believed to be a likely occurrence.

3-8 Modeling with kinetics

To this point reactants were added to (or removed from) the system at arbitrary rates by the software. The reaction progress is also measured parametrically in terms of the reaction progress variable, ξ, which is dimensionless and varies from zero to one from the beginning to end of the reaction path (Bethke, 2008).

The results obtained so far are based on thermodynamic calculations which deal with free energies of reactions. On the other hand, kinetics deals with the rate of a chemical reaction and the reaction mechanism. Thermodynamic principles give us an idea of whether a reaction is able to occur in a given system, while kinetics tells us how fast. To investigate how fast the anticipated reactions could happen and whether these changes will be effective in a geothermal power plant life span, brine-rock interactions were modeled with kinetic data. The brine composition for Vermilion parish, LA, (Table 3-2) and rock composition from previous studies (Table 2-8) were used for kinetics modeling.

The first step to model reactions with kinetics is to select the applicable rate law. A rate law reflects the idea of how a reaction proceeds on a molecular scale and requires that a mineral's specific surface area ($cm^2\ g^{-1}$) and rate constant (mole $cm^{-2}\ s^{-1}$) should be assigned. A rate constant depends on temperature and pH and is not the same for dissolution and precipitation. Therefore, it is not uncommon to find different rate constants for a specific mineral.

The rate constants used here for modeling the anticipated reactions have been adopted from other research work (Table 3-3). For all minerals, except paragonite and muscovite the dissolution rate constant was also used for precipitation. For nontronite the constant for saponite was used.

Table 3-3. The rate constants used for kinetics modeling.

Quartz	$1.93\times10^{-14*}$	Rimstidt and Barnes, 1980
Albite	6.3×10^{-13}	Knauss and Wolery, 1986
Illite	2×10^{-18}	Alekseyev, 2007
Smectite	4×10^{-17}	Alekseyev, 2007
Calcite	2×10^{-8}	Pokrovsky et al., 2009
Chlorite	4×10^{-16}	Smith and Carroll, 2014
Saponite-Ca	1×10^{-14}	Savage et al., 2002
Paragonite	1.02×10^{-13}	Soler and Lasaga, 1998
Muscovite	1.02×10^{-13}	Soler and Lasaga, 1998

**The rate constant unit for all minerals is mole $cm^{-2}\ s^{-1}$*

Based on the rate-limiting step and precipitation rate constant assigning, models have been run with three different approaches.

3-8-1 Assuming reactants dissolution as rate-limiting step – First Approach

In this case reactants dissolution has been assumed to be the rate-limiting step of whole process. In other words, it is assumed that the reactant dissolution happens slowly whereas product precipitation occurs instantaneously. Therefore, there is no need to set the precipitation rate constants for products. The first rock-brine reaction was modeled with a time span from 0.5 year to 5000 years (Fig. 3-7). Titration results have also been shown on the graph. As it can be seen after almost 50 years most of the reactions have been completed, but for illite and muscovite almost 100 years are needed to complete the reaction.

After 100 years there is almost no change in the products and results are similar to the titration results, for example albite changes from 1460 at 100 years to 1437 g in titration. Quartz shows small changes, from initial amount of 8046 to 8115 g in titration, and has not been shown on the graph. Based on these results, the anticipated changes which lead to a 3 percent increase in the clay volume will be achieved in almost 70 years. This is within the life span of a geothermal power plant.

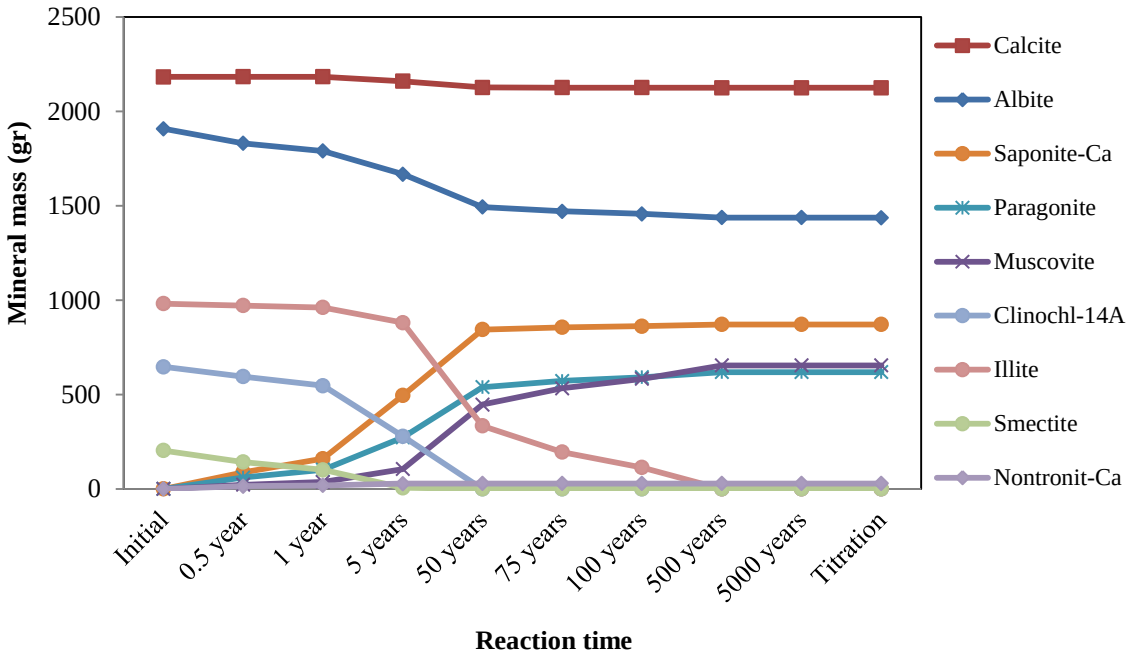

Figure 3-7. The changes in major minerals mass with time in the first approach of kinetics modeling. The reactants dissolution has been assumed to be the rate-limiting step in kinetics reaction path. Titration results also have been shown on the graph. Almost 50 years are needed for most reactions to become completed. After 100 years, results are almost the same as titration path.

3-8-2 Specifying a very small initial mass of products – Second Approach

In the second approach, precipitation rate constants were also considered in the kinetics. Setting a rate constant for products before formation is a challenge. A supersaturated mineral that has not yet formed will have no surface area, and as a result its precipitation rate would be zero. This problem was solved by assuming a very small mass of products in the initial rock composition. From the titration path results it was determined that the products which are not present in the initial rock composition are saponite-Ca, nontronite-Ca, paragonite and muscovite. By including 0.01 gram of these minerals among reactants, their precipitation rate constant can be set in the model.

Small differences can be seen in the results of this case in comparison with the first approach (Fig. 3-8). In the early stages of the reaction, up to 5 years, increases in the amount of albite can be seen whereas in the first approach the albite amount decreases continuously from the beginning of the reaction. The rate of forming other products is also slower than the first approach. For instance, after 0.5 year from the reaction's initiation 88.1 gram saponite-Ca will be formed while this amount will be 64.67 grams in the second approach. After 50 years, however, most of the products will be formed. The formed saponite-Ca amounts after 50 years are 844.2 and 840.2 grams in the first and second approaches, respectively. According to titration path modeling, the total amount of saponite-Ca which can potentially be formed is 871.2 grams. Quartz shows small changes and has not been shown on the graph.

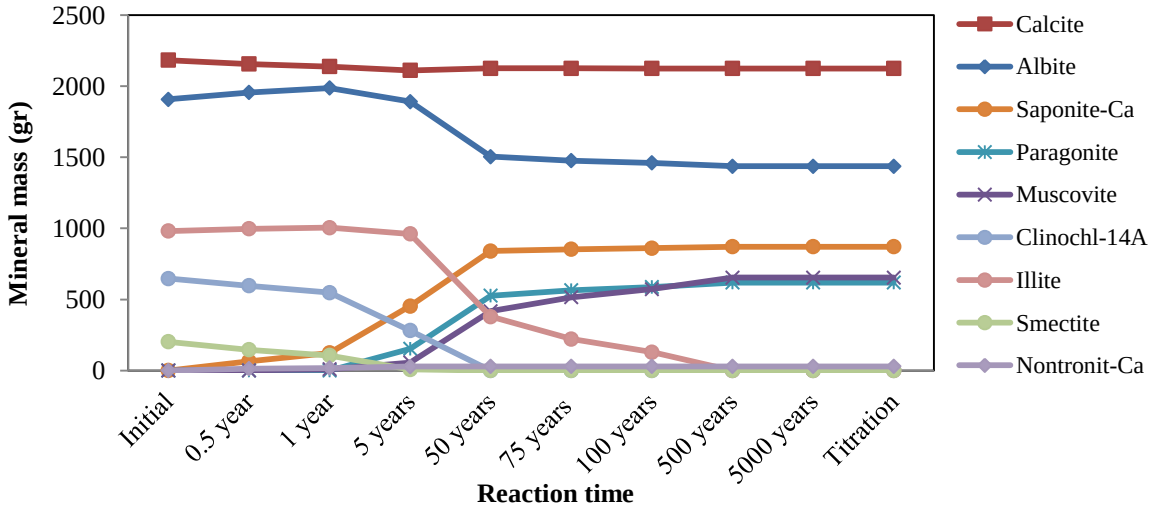

Figure 3-8. The changes in major minerals mass with time in the second approach of kinetics modeling. The reactants precipitation rate constants were also included in the models.

3-8-3 Setting a nucleus density for products – Third Approach

Another method to include the precipitation rate constant in models is by setting a nucleus density for products. Nucleation is the formation of a new phase, here the formation of a solid phase from a supersaturated solution.

An increase in albite can be seen here also (Fig. 3-9). Albite decline, however, starts sooner than the second approach. The product minerals formation in this approach is a little faster than the second approach, but still slower than the first approach. 50 years is still enough to form most of the products. The saponite-Ca amounts formed after 0.5 year and 50 years are 67.51 and 841.4 grams, respectively. Quartz shows small changes and has not been shown on the graph.

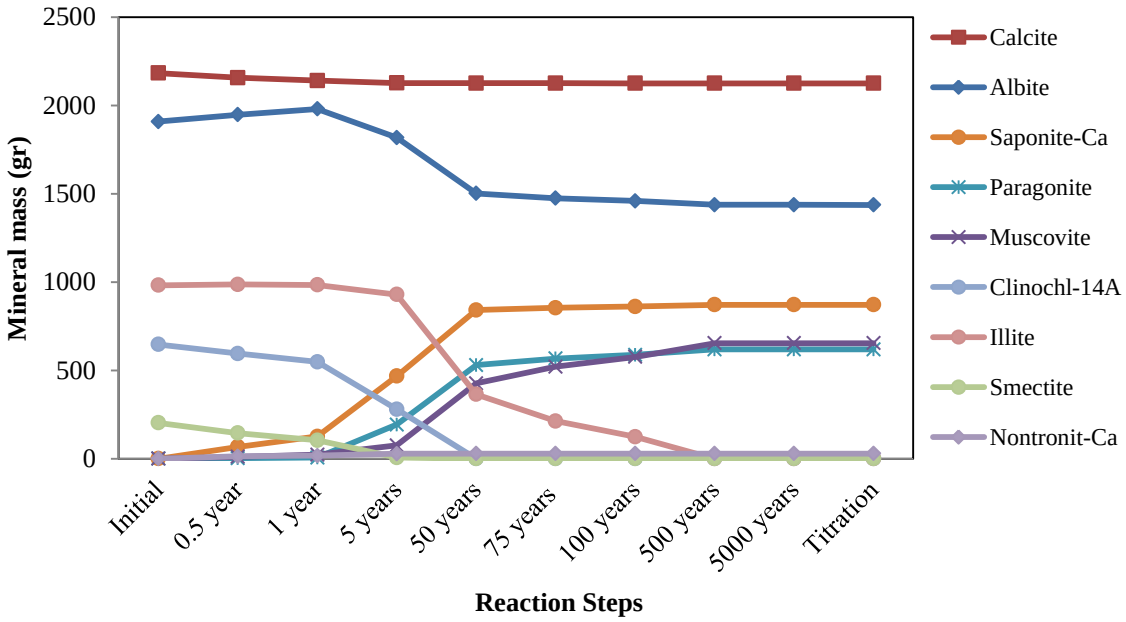

Figure 3-9. The changes in major minerals mass with time in the third approach of kinetics modeling. The reactants precipitation rate constants were also included in the models. Setting a nucleation density makes it possible to include precipitation rate constants in the models. Almost 50 years are needed for most reactions to become completed.

3-9 Scaling in the heat exchanger due to a reduction in temperature

To investigate the precipitation risk inside the heat exchanger, a temperature drop from reservoir temperature, 130 °C, to heat exchanger output temperature, 100 °C, has been modeled. The brine composition shown in Table 3-2 has been used for this section. Results show that the

total precipitated mineral mass is about 0.47 gram for every 1122 grams of solution. Therefore, the mass of precipitation inside the heat exchanger is close to 0.42 g per kg brine.

Most of this precipitate is dolomite (Table 3-4). Quartz, barite and nontronite are other formed precipitates. Assuming 5 kg per second (adopted from Feng et al, 2015) as the brine flow rate to the heat exchanger and 70 years as the anticipated life time of a geothermal power plant, 4.64×10^{6} kg of precipitate is expected to be formed, which is 68 times the heat exchanger volume. Although due to high flow rates much of this precipitation may be carried outside the exchanger to the reservoir rather than form scale in the heat exchanger, the potential of scaling inside the heat exchangers should be considered carefully in heat exchanger design.

Table 3-4. Expected precipitates in heatexchanger due to the temperature drop (gr per kg brine).

Dolomite	0.31
Quartz	0.062
Barite	0.048
Nontronite-Mg	2.65×10^{-5}

3-10 Discussion

The theoretical modeling results discussed above show that equilibrating the initial rock composition with the brine from Vermilion Parish and also core samples rock composition with brine from Chocolate Bayou, causes a transformation of the initial clay compositions to a mixture of purer clay end members with lower free energies. This is accompanied by dissolution of albite to further increase the amount of clay present. Varying the starting fluid composition over a wide range of pH, HCO_3, and Na^+ does not affect the overall results. The reactions do not require a change in temperature, but occur when exposing the fluid to the rock. While the exact clays formed vary, an overall increase in clay content occurs using two different thermodynamic data bases and regardless of whether specific clay minerals are prevented from forming during the modeling. Kinetic modeling shows that this transformation and increase in the clay minerals present should occur in a time span of approximately 70 years.

An apparent contradiction in these results is the expected time span of the reaction from the modeling (approximately 70 years) compared to the fact that the brine has had millions of years to equilibrate with the rock mineralogy. Previous studies (Land and Milliken, 1981, Hanor, 2001, Ausburn and Hanor, 2013) show that fluid composition in similar formations are partially buffered by the rock mineralogy. There are several possible explanations:

1) The fluid composition is erroneous, especially the pH, which is very difficult to determine at subsurface conditions. However, varying the initial fluid composition substantially still leads to the same results.
2) The thermodynamic data are not appropriate, predicting the formation of unlikely pure, higher-temperature phases. However, two different data bases, and suppressing different minerals in the modeling, show similar results. A possibility is that mixed layer illite/smectite is a distinct phase with a specific free energy which was not included. However, the data utilized are the best available from the aqueous geochemical community.
3) Pore waters in isolated layers in the rock are at equilibrium, but the sample obtained from the well mixed fluids from several of these layers together, resulting in a water sample that is not in equilibrium with the rock. However, the results of varying the initial fluid composition still makes this an unlikely reason.
4) The rock composition assumed here is not the exact rock composition in the studied field. The results of varying the initial rock composition, however, show similar results. In addition, the comparison of applied rock composition with similar fields assures that the assumed rock composition here should be close enough to reality.
5) The kinetic modeling predicts a much shorter time span than should be expected. This should be resolved by experimental work with the actual fluid composition and rock compositions.
6) Pore water is in equilibrium with meta stable phases when stagnant. This includes concentration differences between micropores in clay and larger intergranular pores due to double layer effects. Flow through the larger pores at the high rates required by the project may disturb this equilibrium and initiate dissolution of the original clay minerals and albite and precipitation of new clay phases to achieve a lower free energy state.

From an engineering viewpoint, the most important alteration of the rock is a change from the original morphology of clay largely contained in partially altered rock fragments and authigenic grain coating clay to new precipitates, which would be expected to have pore lining or pore bridging morphologies. This change in morphology, accompanied by an increase of approximately 3 percent in total clay content, would be expected to have a substantial negative effect on permeability (Neasham, 1977).

3-11 Expected geochemical alterations

The summary of the geochemical changes predicted by the models are shown in Table 3-5. The next phase of this study will be focused on determining the change in petrophysical rock properties, specifically permeability, due to these expected transformations in the rock mineralogy. Since the creation of additional pore lining and pore bridging clay will reduce permeability and materially impair the project, this is a necessary engineering evaluation.

SEM images indicate that the initial chlorite and smectite minerals in core samples have pore-lining crystal morphology (section 2-4). Based on this natural crystallization environment, it is assumed that the newly generated clay minerals will also have the same type of crystal morphology.

Table 3-5. The geochemical changes expected by the models in volume percentage. The negative values mean decrease in minerals.

Sample No.	Albite	Quartz	Newly generated clay	Porosity
59	-3.46	0.64	**2.27**	0.57
61	-3.57	0.51	**2.49**	0.56
62	-5.74	1.07	**4.08**	0.60
Vermilion Parish	-4.78	1.32	**2.99**	0.41

Chapter 4
Pore Network Modeling

4-1 Introduction

The main objective of this project is to study the permeability changes due to rock-brine geochemical interactions. In chapter 3, the possible geochemical reactions and products were investigated and the geochemical changes were predicted (Table 3-5). In this chapter, pore network modeling is used to quantify the impact of geochemical changes on permeability.

The coupling of geochemical reactions with hydrological and mechanical processes in porous media has already been investigated from different prospective by other researchers (Yoon et al.,2012 and 2015, Kang et al., 2003). Recent advances in multiscale imaging techniques along with advances in computational power and methods have abled researchers to develop pore-scale models for flow and reactive transport (Yoon et al., 2015). These pore-scale models include lattice Boltzmann (LB) (Kang et al. 2003, 2006, 2010), smooth particle hydrodynamics (SPH) (Tartakovsky et al. 2007, 2008), direct numerical simulation (DNS) (Flukiger and Bernard 2009; Molins et al. 2012, 2014), hybrid LB-DNS (Yoon et al. 2012) and pore network models (Li et al. 2006, Kim et al. 2011).

Yoon et al. (2015) have reviewed approaches based on the lattice Boltzmann method (LBM) for pore-scale reactive transport models relevant to the impact of biogeochemical processes on the dynamic permeability evolution. They presented the recent advances in using lattice Boltzmann based approaches to simulate coupled flow and transport affecting pore structure change and flow feedback.

Li et al. (2006) presented a methodology for using pore-scale network modeling to investigate scaling effects in geochemical reaction rates. They simulated the reactive transport processes at the pore scale, accounting for heterogeneities of both physical and mineral properties. Their work demonstrates the use of pore-scale network modeling as a valuable research tool for examining upscaling of geochemical kinetics.

In another research, Kim et al. (2011) used network flow models to simulate the flow of CO_2-saturated brine in the pore networks corresponding to three different sandstones. They used simulations to study upscaling of anorthite and kaolinite reaction rates from pore to core scales.

Pore network modeling is a technique to model the pore-scale flow in porous media. Using this technique, the pore space is discretized into discrete pores, which are connected through pore throats. Network modeling is less rigorous than the direct solution of the equations of motion in the pore space using an approach such as the finite element, finite volume, or lattice Boltzmann method, but it is dramatically more efficient computationally (Bhattad et al., 2011).

Pore scale models, contrary to continuum-scale models, distinguish the void and solid phases and represent a more fundamental approach to modeling transport in porous media (Lane and Thompson, 2010). Modern pore-scale techniques include image-based models that are mapped directly from 3D digital images of porous media (Thompson et al., 2008).

4-2 Image preparation

As mentioned before, the first step to building a pore network model is to obtain a micro-CT scan image from a relevant sample. Micro computed tomography or micro-CT is a X-ray imaging technique in 3D with a very high resolution. Employing digital images for computational modeling ensures that the pore morphology of the real materials, such as pore size distributions, pore-scale heterogeneity, and spatial correlations, are captured by the models (Lane and Thompson, 2010). For this study, the micro-CT scan imaging was performed at the Argonne National Laboratory. The cylindrical samples for the imaging scan were drilled from core samples studied here, with dimension of 7 mm diameter and 15 mm height. The image resolution was 4.1 microns (voxel size).

4-2-1 Filtration

Image filtration was performed in order to smooth images and remove noise. This image processing step was done with AVIZO software (version 9.0.0) (FEI, 2016). An anisotropic

diffusion algorithm was used for smoothing. Anisotropic diffusion is a technique to remove noises without removing significant parts of the image, typically edges, lines or other details that are important for the interpretation of the image (Perona and Malik, 1990). A comparison of images before and after filtration is shown in Fig. 4-1.

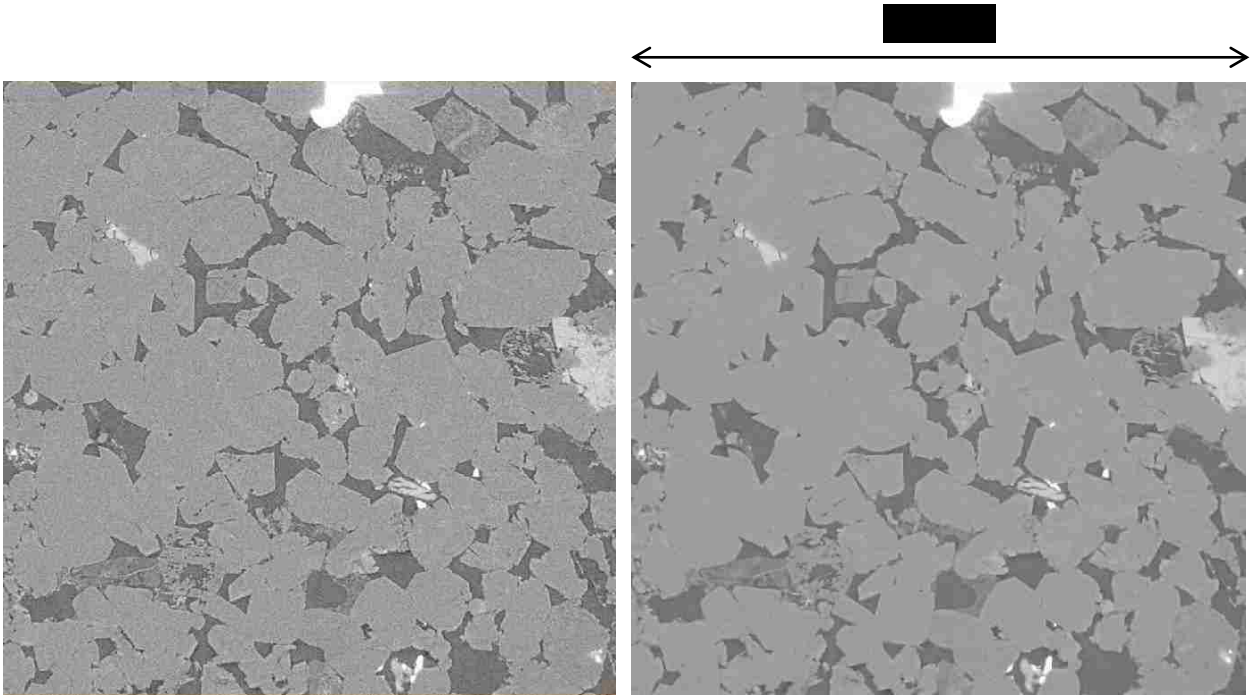

(a) (b)

Figure 4-1. Micro-CT images from core sample 59; (a) before filtration (original image), (b) after filtration. The image dimensions are 1000×1000×1000 voxels.

4-2-2 Segmentation

Segmentation of an image is usually performed to translate the image data from grayscale to discrete in order to identify phases within an image. In this research, because the mineralogy and rock composition were considered, the images were segmented into phases with identifiable mineral composition. In the segmentation process, the initial gray scale image is transformed to a binary image with assigning 0 and 1 to different phases.

As concluded from the rock characteristic studies (Table 2-7), the core samples contain quartz, feldspar, clay and void space. To apply the geochemical changes obtained from Chapter 3, the images should be segmented in a way that each compositional substance is identified and

labeled differently. Quartz and feldspar have similar attenuation characteristics; hence, their segmentation was not possible quantitatively.

The information obtained from thin section images assisted in identifying different phases in segmentation process. Knowing the place and shape of the appearance of different minerals helps to identify them in micro-CT scan images. An example of thin section image including kaolinite is shown in Fig. 4-2, which helps to segment the clay section.

Segmentation was performed using AVIZO software (Version 9.0.0) (FEI, 2016). With each segmentation step, two phases were separated. In the first segmentation process, the image was sectioned as voids-quartz-feldspar and clay minerals (Fig 4-2), in which clay voxels were labeled as 1 and voids-quartz-feldspar voxels were labeled as 0. In the second segmentation process, the image was sectioned as voids-clays and quartz-feldspar (Fig 4-3), in which quartz-feldspar were labeled as 1 and voids-clays voxels were labeled as 0. These two segmented images, then, were combined together changing quartz-feldspar label from 1 to 2. As a result, in the final image (Fig. 4-4) there will be three phases; voids (labeled as 0), clays (labeled as 1), and quartz-feldspar (labeled as 2).

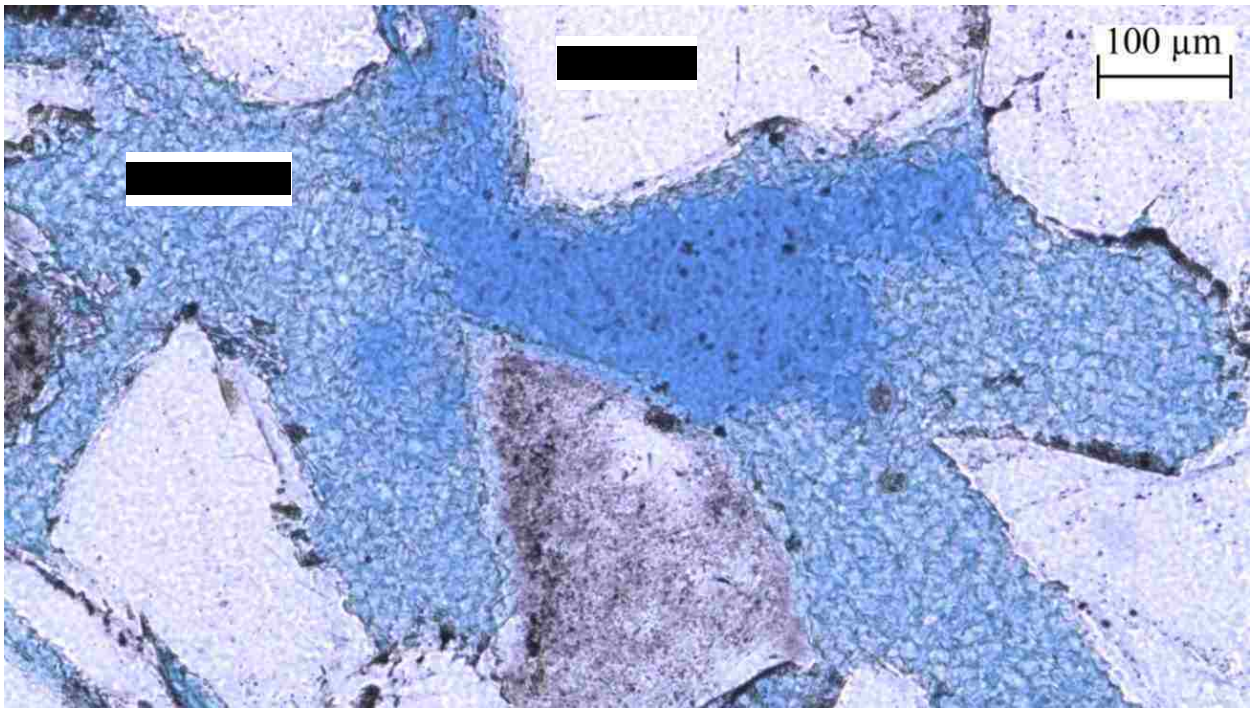

(a)

Figure 4-2. (a) A thin section image from sample 61 including kaolinite, which helps to identify the clay section.

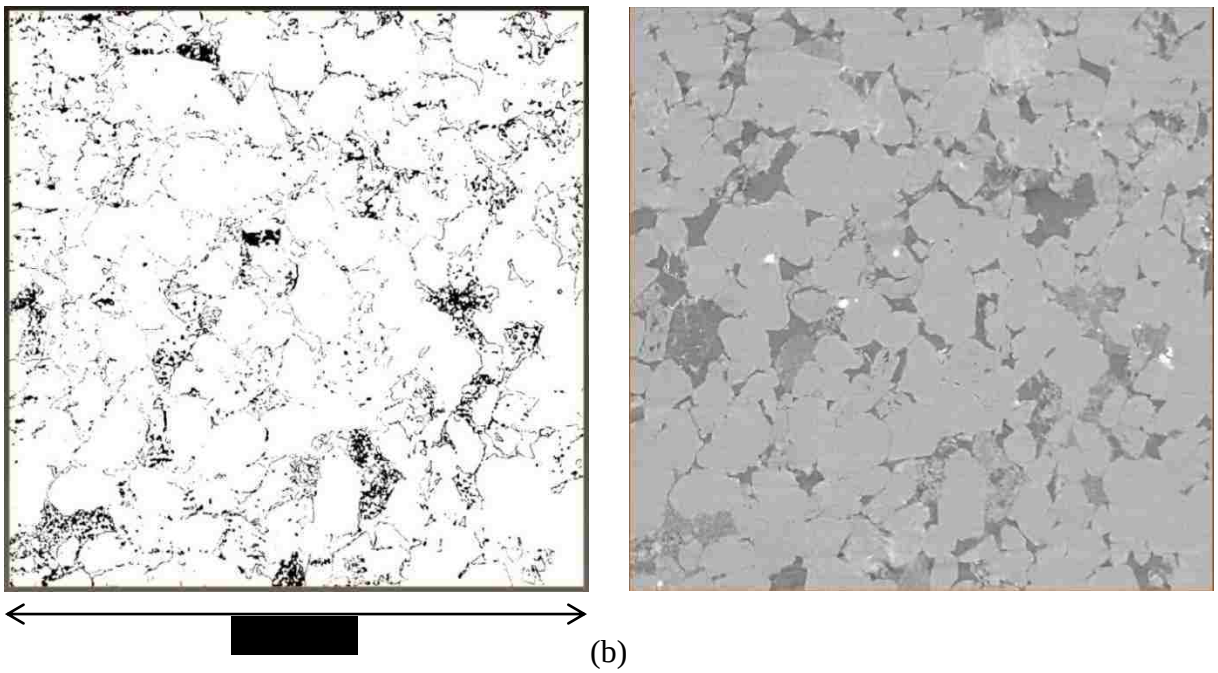

(b)

Figure 4-2 (continue). (a) A thin section image from sample 61 including kaolinite, which helps to identify the clay section. (b) The segmented micro-CT image of sample 61 next to the original grayscale image. The black voxels are clays and the white voxels are voids-quartz-feldspar . The micro-CT image dimensions are 1000×1000×1000 voxels.

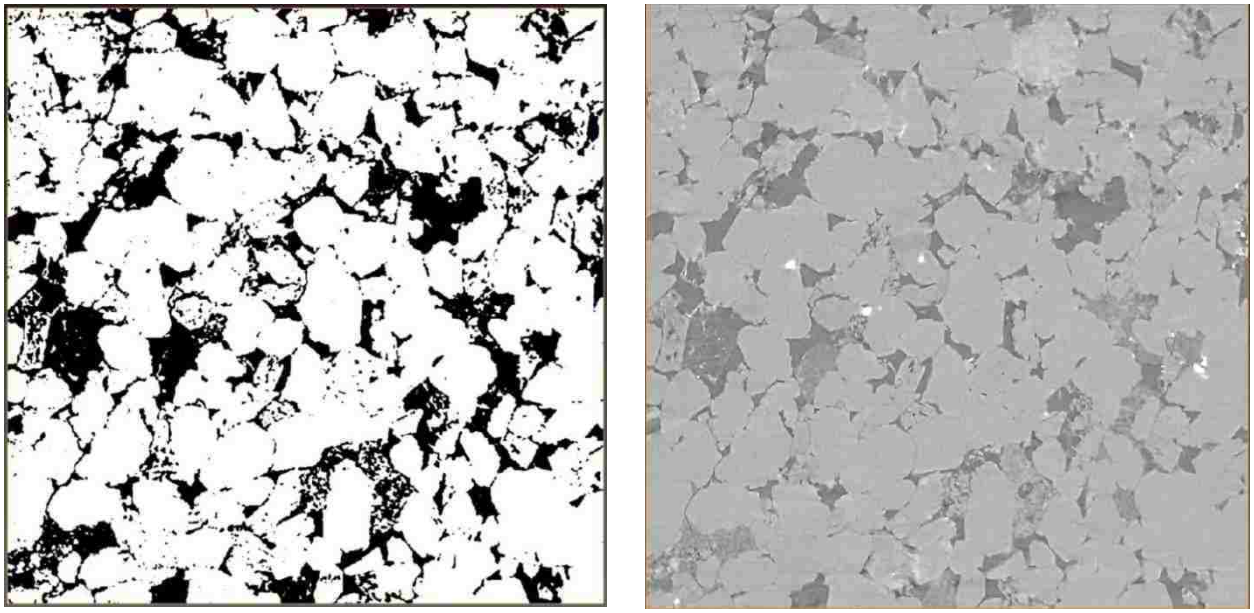

Figure 4-3. The segmented micro-CT image of sample 61 next to the original grayscale image. The black voxels are voids-clays and the white voxels are quartz-feldspar. The image dimensions are 1000×1000×1000 voxels.

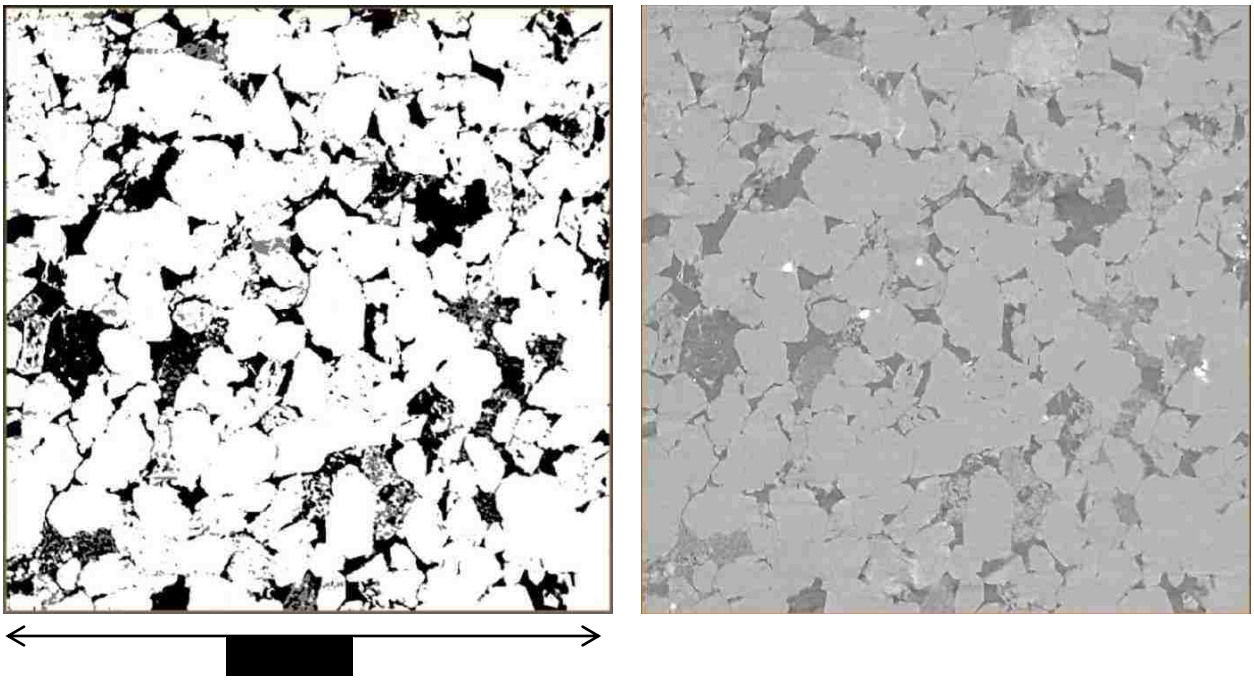

Figure 4-4. The final segmented micro-CT image of sample 61 next to the original grayscale image. The black voxels are voids (labeled as 0), the gray voxels are clays (labeled as 1), and the white voxels are quartz-feldspar (labeled as 2). The image dimensions are 1000×1000×1000 voxels.

An algorithm was developed here to count the number of voxels. The volume percentage of voids, clays, and quartz-feldspar can be identified by knowing the total number of the voxels and counting the number of voxels with values of 0, 1 and 2, respectively. The rock composition of the micro-CT images after segmentation using a subsection with dimensions of 600×600×600 is shown in Table 4-1.

Table 4-1. The rock composition of the micro-CT images after segmentation with dimensions of 600×600×600.

Sample No.	Quartz-feldspar	Clay	Porosity
59	76.64	5.58	17.79
61	75.89	6.40	17.72
62	77.23	8.21	14.58

4-2-3 Ring artifact

Ring artifacts are usually caused by a miscalibrated or defective detector element, which results in rings centered on the axis of rotation (Boas and Fleischmann, 2012). Ring artifacts were recognized in all micro-CT scans of the core samples in this study. These rings were wrongly segmented as clays and/or voids (4-5-a). These artifacts were removed by changing the incorrect labels to the appropriate labels manually using ImageJ software (ImageJ, 2011). An example of the ring artifact removal is shown in Fig. 4-5 for sample 61.

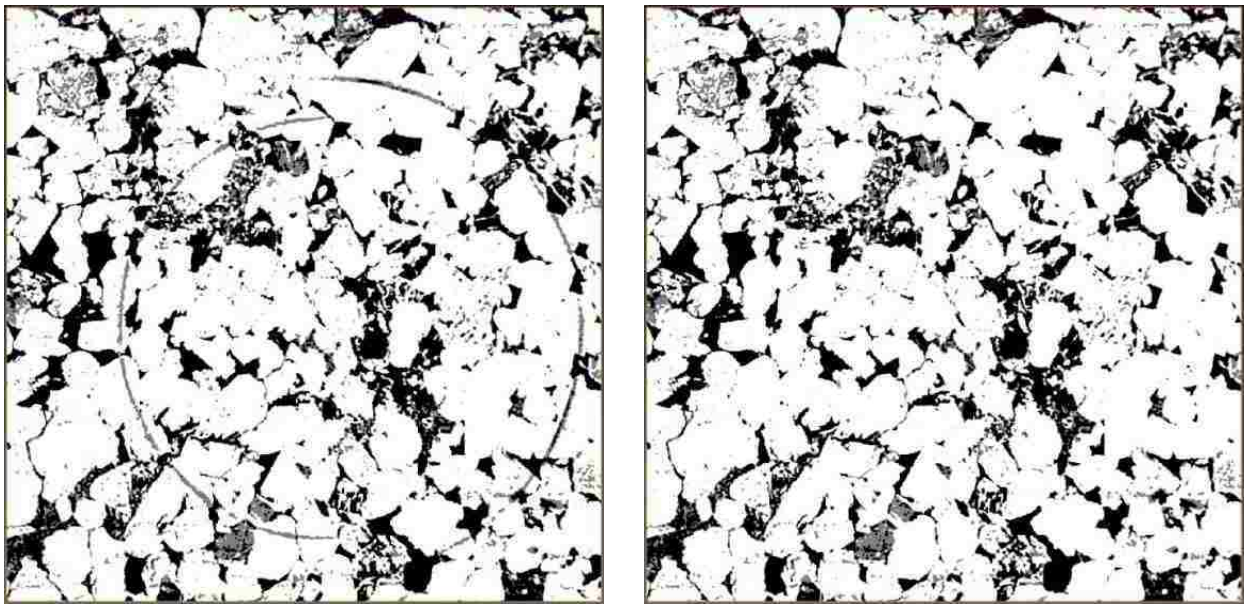

(a) (b)

Figure 4-5. The ring artifacts in the micro-CT scan image of sample 61; (a) before the artifact removal, (b) after the artifact removal. The image dimensions are 1000×1000×1000 voxels.

4-2-4 Grain segmentation

In the segmentation process, the image is partitioned into specific phases with known composition. Within a specific phase, however, we can perform object segmentation to identify distinct grains. This task was done using an available algorithm (Thompson et al., 2006). The code builds the granular structure of the image. In this process the voxels which belong to a specific grain, are labeled by that particular grain number. By completing this process each grain will have its own label which makes is distinguishable from other grains in the data set.

The grain segmentation process was done separately for each compositional phase because for each application of the code, only one phase of the image can be grain-segmented. In other words, clays phase were labeled separately from the quartz-feldspar phase (Fig. 4-6). Some over segmentation can be seen in the results (Fig. 4-6-b). Although, the grain segmentation process algorithm did not do a great job of identifying physical grains, it is acceptable to be used for the rest of the project.

To form the final grain-segmented image, these two separate images should be combined. Before merging the grain-segmented images, feldspar and quartz grains need to be separated.

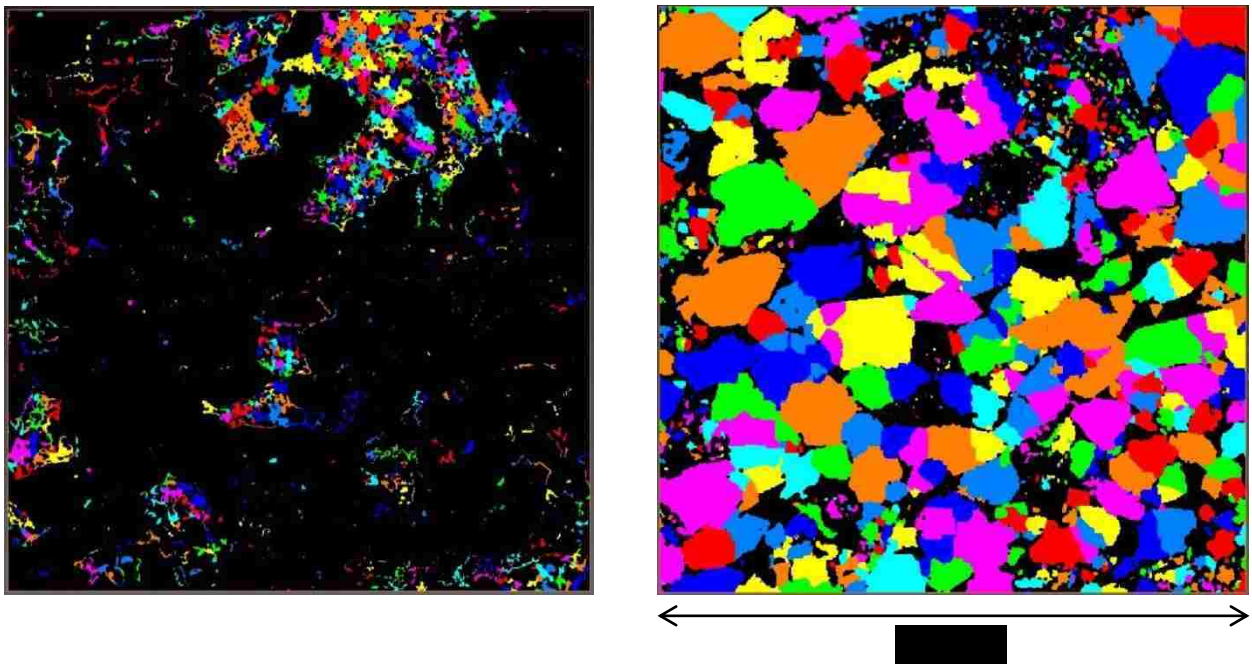

(a) (b)

Figure 4-6. The grain-segmented micro-CT image for sample 62; (a) clay grains, (b) quartz-feldspar grains. The image dimensions are 600×600×600 voxels.

4-2-5 Quartz-feldspar separation

As it mentioned earlier, effective segmentation of quartz and feldspar was not possible because they have similar attenuation characteristics. However, the geochemical modeling revealed that an increase in the clay content will occur due to a feldspar-to-clay conversion. Thus, knowing the content and location of the feldspar grains is an essential piece of information.

To address this limitation, an algorithm was developed in this research to separate feldspar grains from quartz grains. The program generates random numbers and re-labels the voxels with the values equal to the random numbers as feldspar grains. In this way, some of the quartz-feldspar grains will be re-labeled as feldspar grains randomly, but according the known relative abundance in the samples.

In the sedimentary rock formation process, deposition happens when the energy of the transporting medium becomes too low to continue the transport process. In this process, grains with higher density and larger size will deposit sooner. Quartz and feldspar have pretty close density, 2.65 g/cm^3 and 2.56 g/cm^3 respectively, and have similar sizes in sandstone samples here, based on thin section images, therefore assumption of random distribution of quartz and feldspar grains in samples is acceptable.

The fraction of feldspar grains in micro-CT images was obtained from the core sample compositions discussed in chapter 2. The ratio of the quartz to feldspar is known from the thin section analysis results for each sample. Having this ratio, the number of voxels which need to be re-labeled as feldspar can be calculated. In other words, the quartz to feldspar ratio in micro-CT images is similar to this ratio in core samples. Feldspar grains and quartz grains differentiated in the micro-CT image for sample 62 are shown in Figure 4-7.

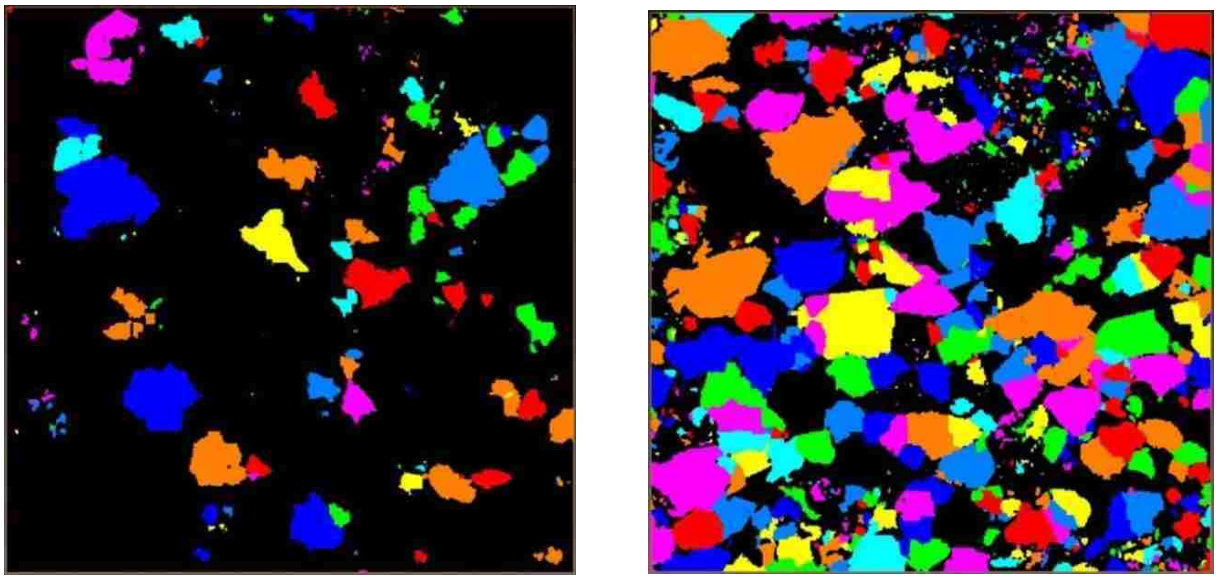

(a) (b)

Figure 4-7. Feldspar grains and quartz grains for sample 62; (a) feldspar grains, (b) quartz grains. The image dimensions are 600×600×600 voxels.

4-2-6 Combining grain-segmented images

To form the final micro-CT images, the grain-segmented images of clay, feldspar, and quartz were merged together. This merging was performed by developing a code here in which the maximum value of the voxels of the first image is added to the voxel values of the second image. The value of the voxels of the third image is also shifted in a similar manner. All three images are then combined.

In this way, the range of the values for each compositional section is known and any change can be applied to an appropriate grain. The final micro-CT images of three core samples are shown in Fig. 4-8. The dimensions of these images are 600×600×600 voxels. The anticipated geochemical changes can be applied to the images at this stage. The rock composition of the micro-CT images are given in Table 4-2. The rock composition based on the rock characterization study (Chapter 2) are also given for the comparison purposes. An acceptable comparison can be seen between these results. Porosity obtained from thin section point counting (Table 2-4) is in agreement with porosity in micro-CT image segmentation (Table 4-2). Because in both thin section and micro-CT scan imaging, microporosity is not taken into account, but in the porosity measurement test this amount is included.

Table 4-2. The rock composition of the final micro-CT images with dimensions of 600×600×600 and the composition based on the rock characterization studied.

	Sample No.	Quartz	Feldspar	Clay	Porosity
Image segmentation	59	65.85	10.78	5.58	17.79
	61	61.39	14.49	6.40	17.72
	62	64.09	13.12	8.21	14.58
Thin section point counting	59				17.04
	61				14.13
	62				12.54
Rock characterization	59	63.11	10.45	5.59	20.66
	61	59.56	14.15	4.67	21.62
	62	60.45	12.73	7.95	18.87

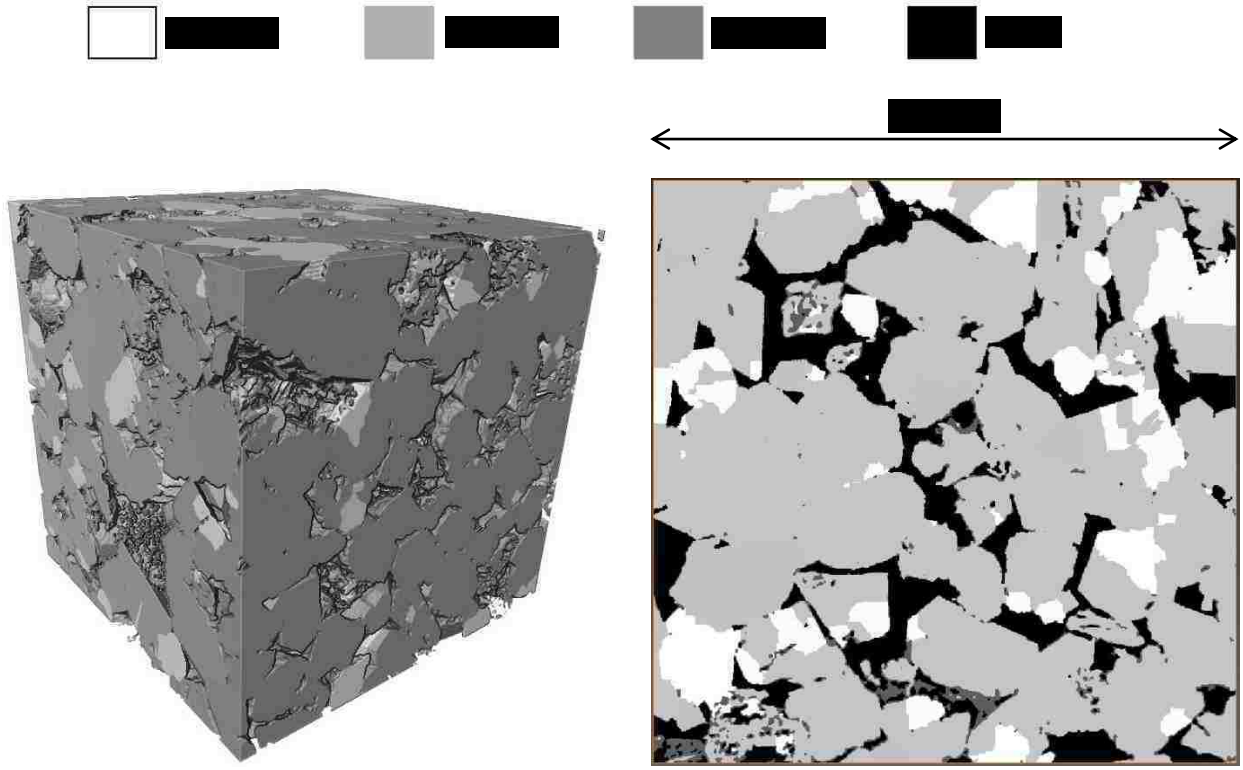

(a) (b)

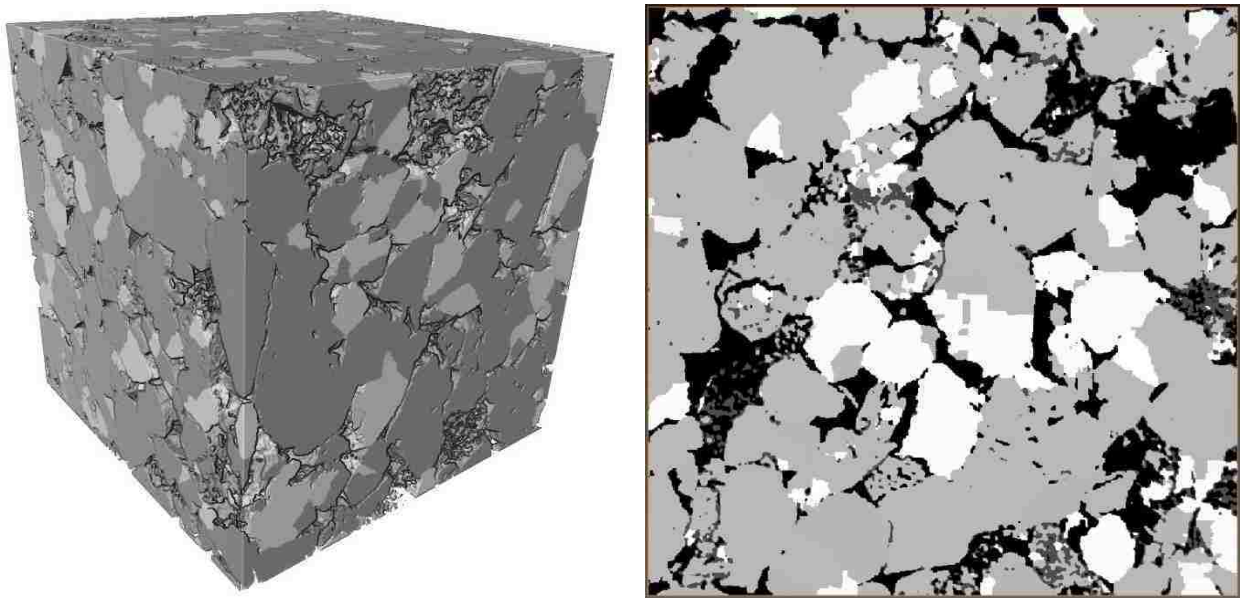

(c) (d)

Figure 4-8. The final micro-CT images of core samples; (a) sample 59-3D, (b) sample 59-2D, (c) sample 61-3D, (d) sample 61-2D, (e) sample 62-3D, and (f) sample 62-2D. The image dimensions are 600×600×600 voxels.

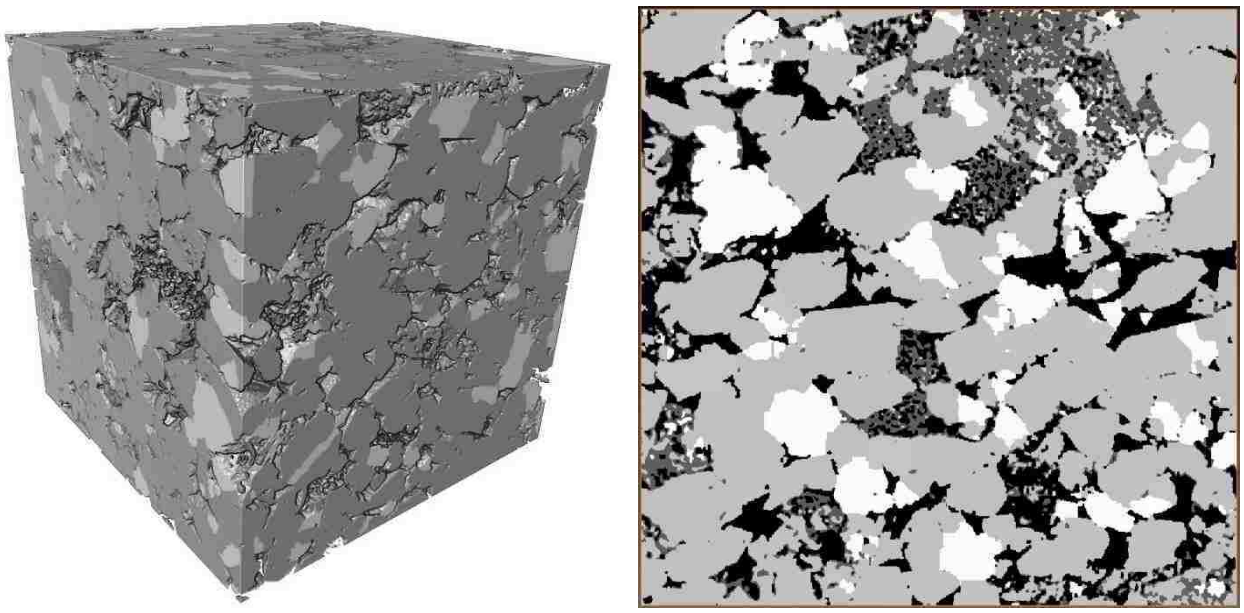

(e) (f)

Figure 4-8 (continued). The final micro-CT images of core samples; (a) sample 59-3D, (b) sample 59-2D, (c) sample 61-3D, (d) sample 61-2D, (e) sample 62-3D, and (f) sample 62-2D. The image dimensions are 600×600×600 voxels.

4-3 Initial permeability calculation

In order to calculate the permeability, the pore network model of the micro-CT image needs to be generated. The .psn extension (PoreSim Network) is used to denote data files created or used with PoreSim research programs and/or software (PoreSim, 2005).

The available Critical Length Finder code CLF_15.05.04 (Thibodeaux et al., 2014) was used to calculate the permeability of the core micro-CT images. In this code a pressure difference is assumed across the sample and using the conductivity of throats the pore-scale flow distribution is calculated. The total flow rate, then, is obtained by summation of the flow rate of all throats. Knowing the total flow rate, the sample permeability can be calculated using Darcy's law ($Q = \frac{-kA(p_b - p_a)}{\mu L}$).

To use the CLF code pore network models of the micro-CT images were generated using the vox2net program (Thompson et al., 2008). The pore network of sample 59 is shown in Fig. 4-9. The initial permeability of the core micro-CT images is given in Table 4-3. In the network of sample 59 the pore number is 24,756 and throat number is 77,439. These numbers for sample 61

are 45,460 and 179,563, respectively. In the network 62 the pore number is 60,538 and throat number is 164,916 (Appendix D). The values of the calculated initial permeability are higher than the permeability test results (Table 2-3, also given here), but still samples 59 and 62 have the highest and lowest permeability, respectively. The samples, which are used for permeability calculations, are much smaller than the permeability test samples. This can be a reason for the difference between calculation and test results.

Table 4-3. The initial permeability of the core micro-CT images in mD.

	Sample No.	k_x	k_y	k_z	k_{avg}
Calculation results	59	3216	2472	2043	2577
	61	1271	1277	1118	1222
	62	608	525	533	555
Lab test results	59	_	_	_	1690
	61	_	_	_	612
	62	_	_	_	105

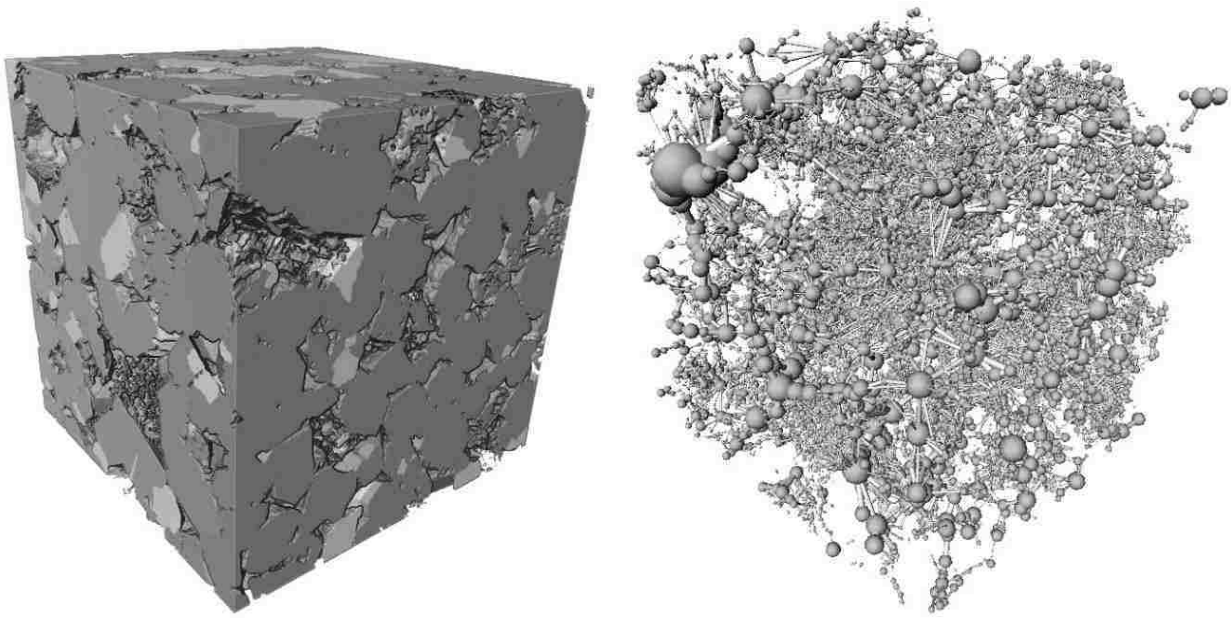

(a) (b)

Figure 4-9. (a) The 3D micro-CT image of sample 59, (b) The AVIZO visualized image of pore network model of sample 59. For this network the pore number is 24,756 and throat number is 77,439.

4-4 Applying the geochemical changes

The anticipated geochemical reactions and products were discussed in Chapter 3. A summary of the geochemical changes is given in Table 3-5. The objective of this chapter is to study the impact of these reactions on petrophysical properties of a reservoir, especially permeability. Accordingly, the expected rock composition alterations, shown in Table 3-5, were applied to the core micro-CT images and the change in permeability was calculated as described below.

The geochemical modeling results show that the quartz content will not change significantly; this change is around one percent increase in the quartz amount in sample 62. On the other hand, feldspar shows around 4 percent decrease. The reason is the feldspar-to-clay conversion process, which is predicted by the geochemical models. A corresponding 2 to 4 percent increase in the clay also can be seen in the results (Table 3-12).

To analyze permeability changes, a new algorithm was developed in this study to apply the anticipated compositional changes to the micro-CT data (Appendix C). It is expected that the reactions happen at locations with highest rock-brine interactions. To increase the amount of quartz, therefore, this program finds the quartz grains which are in the vicinity of pores, and by changing the value of pore voxels from 0 to the value of the adjacent quartz grain, the quartz content is increased to the desired amount.

With a similar process, the amount of feldspar is decreased in the micro-CT images. The program finds feldspar grains that have surfaces exposed to pores, and changes the value of feldspar voxels to 0, which means the feldspar voxel changes to void voxel. This process continues until the appropriate decrease in feldspar content is reached.

Geochemical models show that the feldspar-to-clay conversion process will most probably increase the amount of illite family group minerals in the rock. Although the thickness of coating of clay minerals differs for different type of minerals and their crystal morphology, it usually ranges from 0.1 to 20 microns (Tiab and Donaldson, 2012). This thickness for illite is about 0.1 to 10 micron. For kaolinite, chlorite and smectite this range is about 2-20, 2-10, and 2-12 micron, respectively (Tiab and Donaldson, 2012).

The SEM images of core samples indicate that pore-lining chlorite and smectite can be found in the sandstone studied in this project (section 2-4). Based on this natural crystallization environment, it also assumed that the newly generated clay portion will have pore-lining crystal morphology and this morphology was considered in applying the geochemical changes to the micro-CT images.

To apply the newly generated clay minerals to the micro-CT images two criteria have been considered; (1) Formation of the clay coatings occurs in layers. In the current model, the minimum thickness of a layer can be as low as the voxel resolution, which here is 4.1 microns. Assuming the formation of the illite family of clay minerals, up to two layers (8.2 micron) can be formed on the grain surfaces, (2) Formation of the clay coats occurs in vicinity of feldspar grains. Migration of the formed clay minerals to other pores, however, is possible.

The program developed in this study is designed in a way that adds the newly generated clay minerals to a micro-CT image in layers, up to two layers. It also gives the option of adding clay minerals to feldspar and/or quartz grains. For each type of grains, the program is able to partly cover grains surface to reach close to a target clay percent. With these options, adding the clay layers to a desired point is possible. The uniform distribution of the clay voxels over the micro-CT image is also possible, depending on what is determined to most accurately reflect the chemistry and physics of the process being modeled.

After applying the geochemical changes to feldspar grains, adding the newly generated clay starts from feldspar grain surfaces. The program locates feldspar surfaces that are in vicinity of pores. Then, it changes the value of the adjacent pore voxels from 0 to a negative number equal to the feldspar voxel value. In this way, all the newly generated clay voxels will be assigned negative values and their volume percentage can be calculated and controlled. In a similar manner, clay layers can be added to quartz grains. Adding clay to quartz grains represents downstream deposition of the clay. The process of adding clay voxels to the image continues until the appropriate volume percentage is generated.

According to the results given in Table 3-5, the geochemical changes were applied to the micro-CT images used in this study. For sample 59, the amount of feldspar was decreased from 10.78 to 7.32 percent. Quartz was increased from 65.85 to 66.49 percent. Clay was added as two

voxel layers on feldspar grains and one layer partly covered quartz grains. The net result is addition of 2.35 volume percent newly generated clay voxels. Figure 4-10 shows sample 59 before and after applying the geochemical changes.

In a similar manner, the geochemical changes were applied to samples 61 and 62. Figures 4-11 and 4-12 show samples 61 and 62 respectively, before and after applying the geochemical changes. The permeability of the altered images dataset were calculated using the CLF code (Thibodeaux et al., 2014). In the network of sample 59 the pore number is 36,040 and throat number is 150,907. These numbers for sample 61 are 63,347 and 298,901, respectively. In the network 62 the pore number is 75,745 and throat number is 280,029 (Appendix D). The rock composition and permeability of the samples before and after changing the images to reflect the geochemical changes are given in Table 4-4.

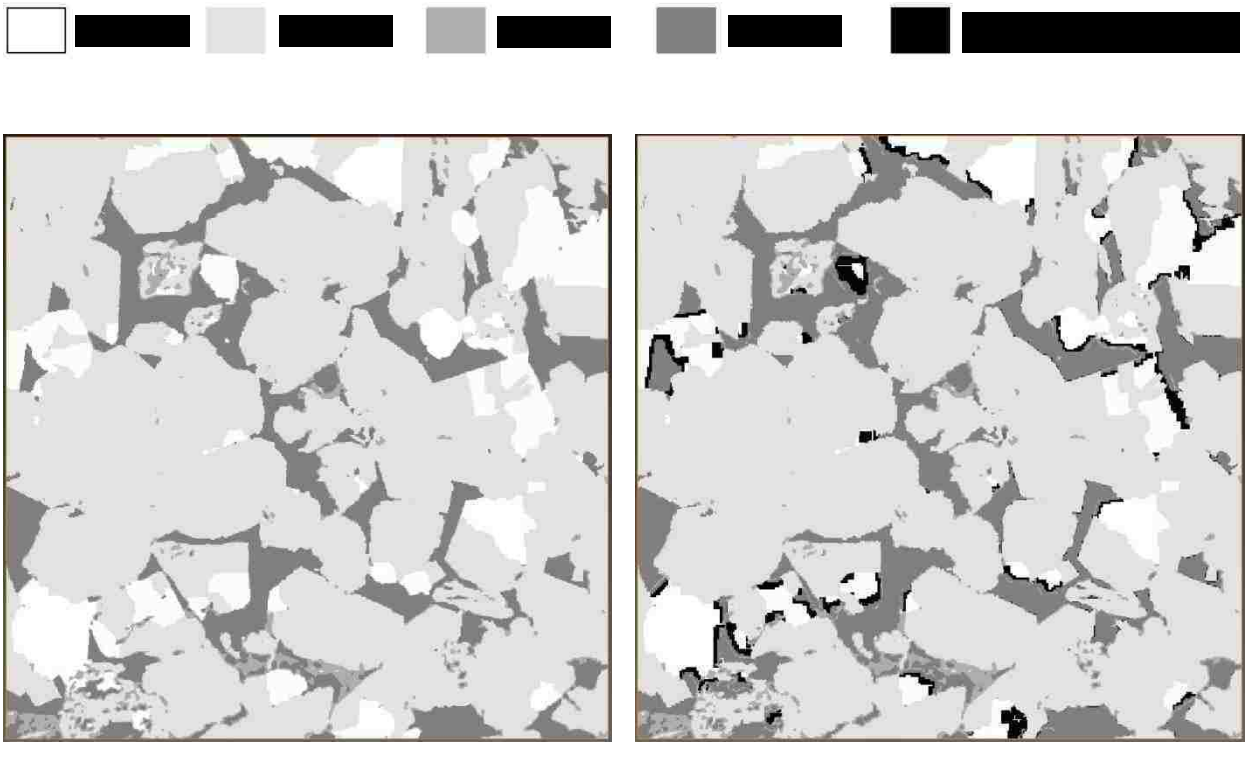

(a) (b)

Figure 4-10. Application of the geochemical changes to the image sample 59 (a) Initial, (b) Altered.

Table 4-4. The rock composition (volume percent) and permeability (mD) before and after alteration.

Sample No.	59		61		62	
	Initial	Altered	Initial	Altered	Initial	Altered
Clays	5.58	5.58	6.40	6.40	8.21	8.21
Feldspar	10.78	7.32	14.49	10.92	13.12	7.38
Quartz	65.85	66.49	61.39	61.90	64.09	65.16
Newly generated clay	0	2.35	0	2.38	0	3.69
Porosity	17.79	18.26	17.72	18.40	14.58	15.56
Permeability	**2532**	**2151**	**1220**	**1067**	**554**	**549**
Permeability ratio (k/k_0)		**0.85**		**0.87**		**0.99**

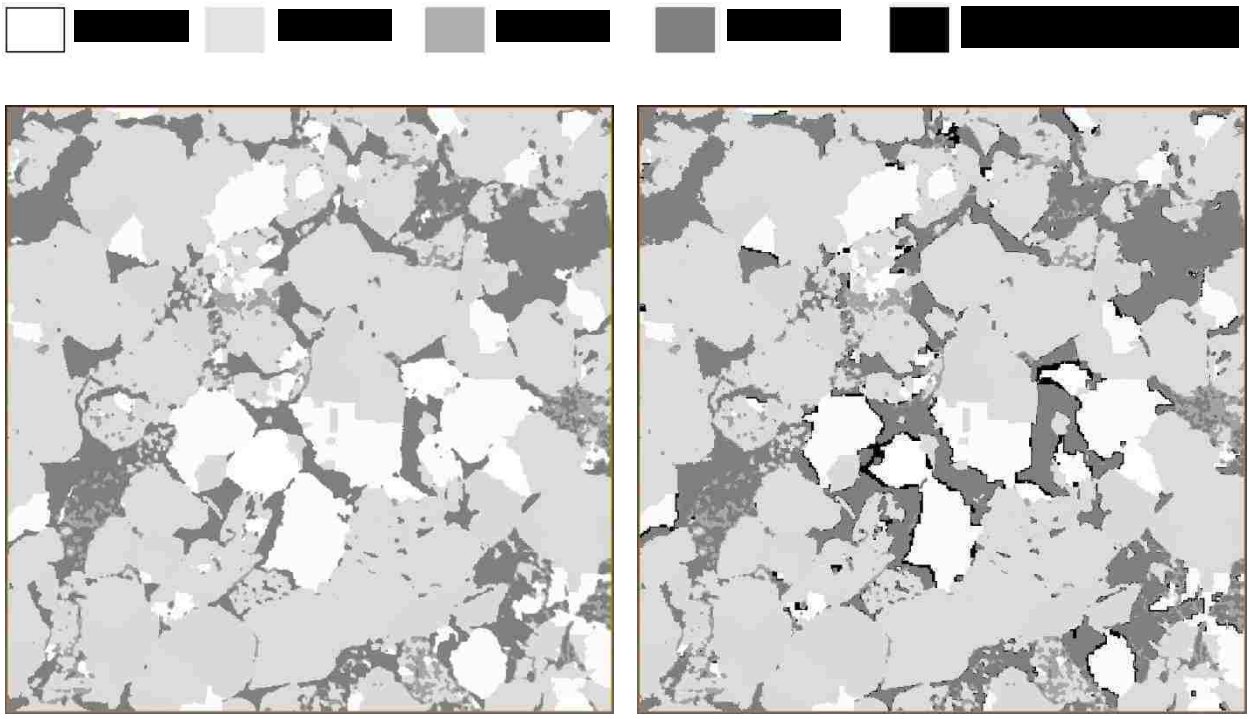

(a) (b)

Figure 4-11. Application of the geochemical changes to the image sample 61 (a) Initial, (b) Altered.

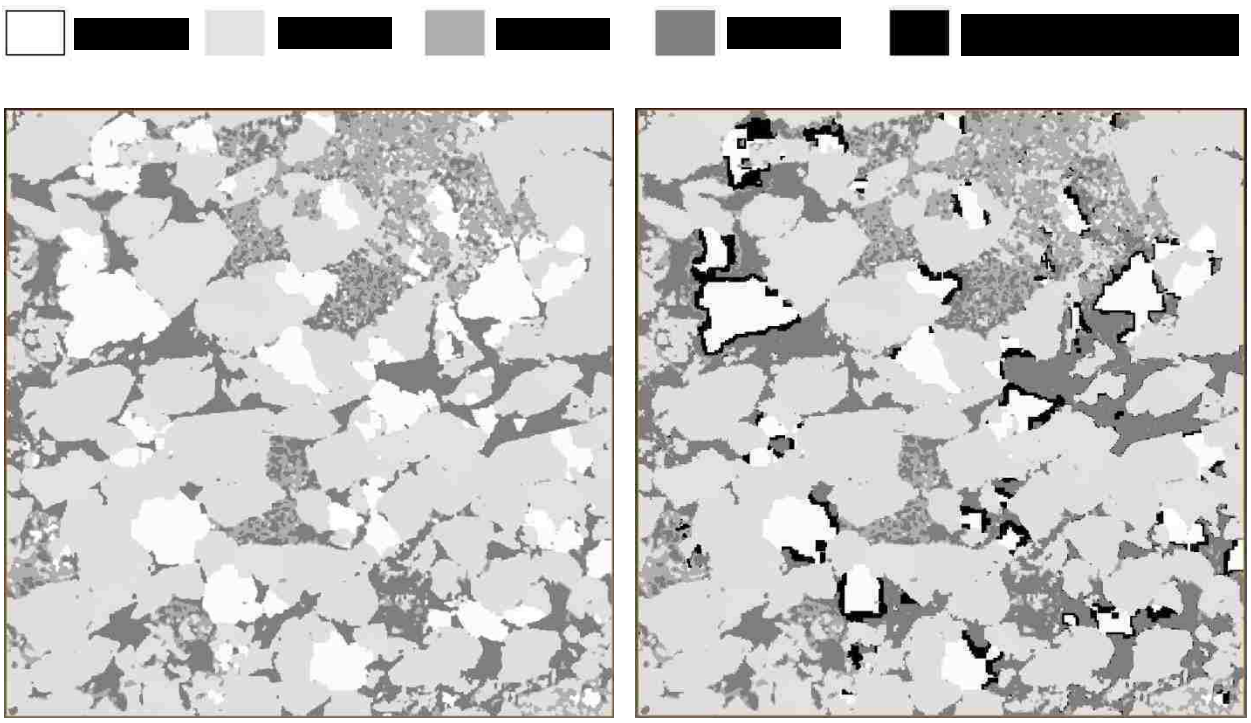

(a) (b)

Figure 4-12. Application of the geochemical changes to the image sample 62 (a) Initial, (b) Altered.

4-5 Clay crystal morphology and microporosity

Neasham (1977) divided dispersed clay particles in sandstones into three general types (Figure 4-13): (i) discrete particles, (ii) pore-lining clays and (iii) pore-bridging clays. Discrete particles is the typical form of occurrence for kaolinite in sandstone. Illite, chlorite, and smectite, however, can occur as both pore-lining and pore-bridging clays (Neasham, 1977). The discrete particles have the lowest negative impact on permeability, while pore-bridging morphology has the most sever permeability damage (Neasham, 1977). The bridging morphology forms partial to complete barrier to fluid flow and even in relatively high porosity sands and low clay content, it can seriously impair rock permeability (Neasham, 1977). While the above is well understood in general terms, the current study gives us the opportunity to quantify the impact that this clay deposition has when it occurs in specific amounts and at specific locations based on the expected geochemistry.

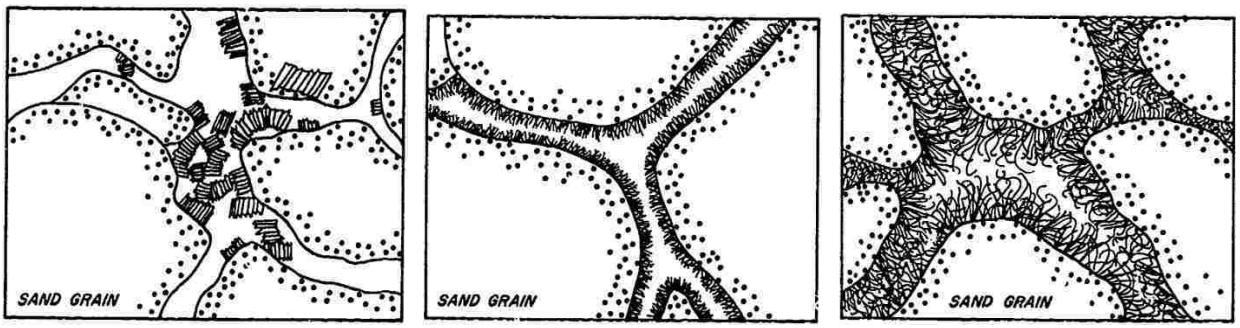

(a) (b) (c)

Figure 4-13. Three general types of clay crystal morphology; (a) Discrete particles, (b) Pore-lining clays, (c) pore bridging clays (Neasham, 1977).

The microporosity of clays also needs to be considered when adding the newly generated clay phase to the micro-CT images. Sears (1983) found that the microporosity constitutes from one-fifth to four-fifths of the total porosity in Southern California Miocene sandstones. The fluid flow through the micropore system is restricted, hence, rocks with large amounts of microporosity have low permeabilities (Sears, 1983).

In order to take the clay microporosity into account, twice the clay volume predicted by geochemical models was added to the micro-CT images, assuming 50% microporosity. This case represents microporous but impermeable clay minerals. The permeability of samples were calculated for this case and given in Tables 4-7, 4-8, and 4-9 for sample 59, 61, and 62, respectively.

A novel method was also used to consider microporous and permeable clay minerals. The objective of this technique is to estimate the restriction caused by clays, accounting for the fact that the precipitated clays may not be a solid phase but instead can be microporous and permeable, which means they could contribute to flow conductivity. In this method, a relation was derived based on the difference between flow rate in a simple duct with solid barriers, representing microporous-impermeable clay sheets, and a simple duct with discrete barriers, representing microporous-permeable clay sheets. Using this equation, the conductivity of the throats containing newly generated clay was modified (Appendix C). The calculated permeability with these modified conductivities serves as the permeability result for the microporous-permeable clay.

The fluid flow through a simple open duct (4-14) was used to model the fluid flow through throats. Flow rates were calculated using an FEM algorithm for low-Reynolds-number flow (Lane and Thompson, 2010). Four different arrangements of barriers which are attached to the side walls were used to model the presence of clay minerals inside the throats. For pore-lining clays, the crystals may be oriented either perpendicular or parallel to the pore wall surface (Neasham, 1977). Therefore, the conductivity correction equation was derived with both parallel and perpendicular barrier orientations.

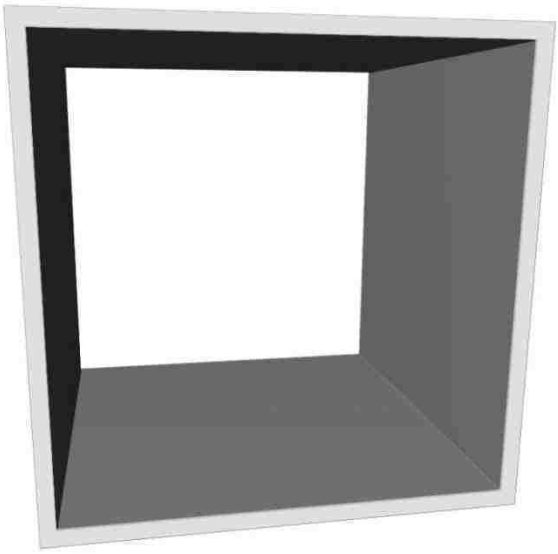

Figure 4-14. A simple open duct which is used to model the fluid flow through throats.

In this study, the original image (no added clay) and the image containing newly generated microporous impermeable clay can be used to compute permeability directly; the cases containing newly generated microporous permeable clay need to be modeled using a new technique. In the following calculations, the parameters related to the original image are shown with subscript of 1 and the parameters related to the cases containing newly generated microporous permeable and impermeable clay are shown with subscript of 2 and 3, respectively.

4-5-1 Perpendicular barrier orientation

In this case barriers are located on four different walls of the open duct where they are perpendicular to the flow direction (4-15). The solid barriers (4-15, a through d) represent the

clay minerals without micropores and the discrete barriers (4-15, a´ through d´) represent the clay minerals containing microporosity.

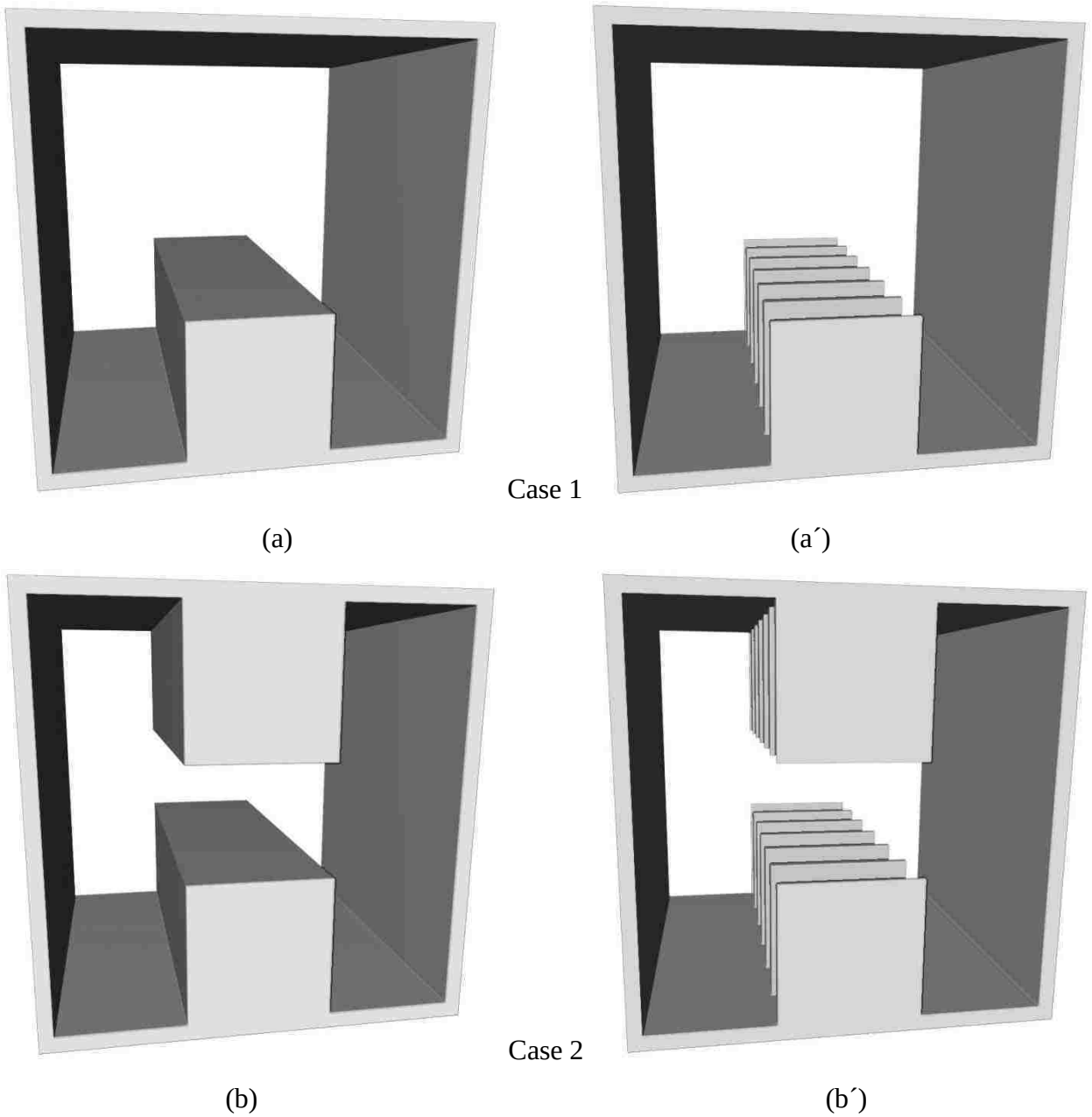

Figure 4-15. Barriers with perpendicular orientation in respect to the fluid flow direction, a through d represent clay minerals without micropores and a´ through d´ represent clays with micropores.

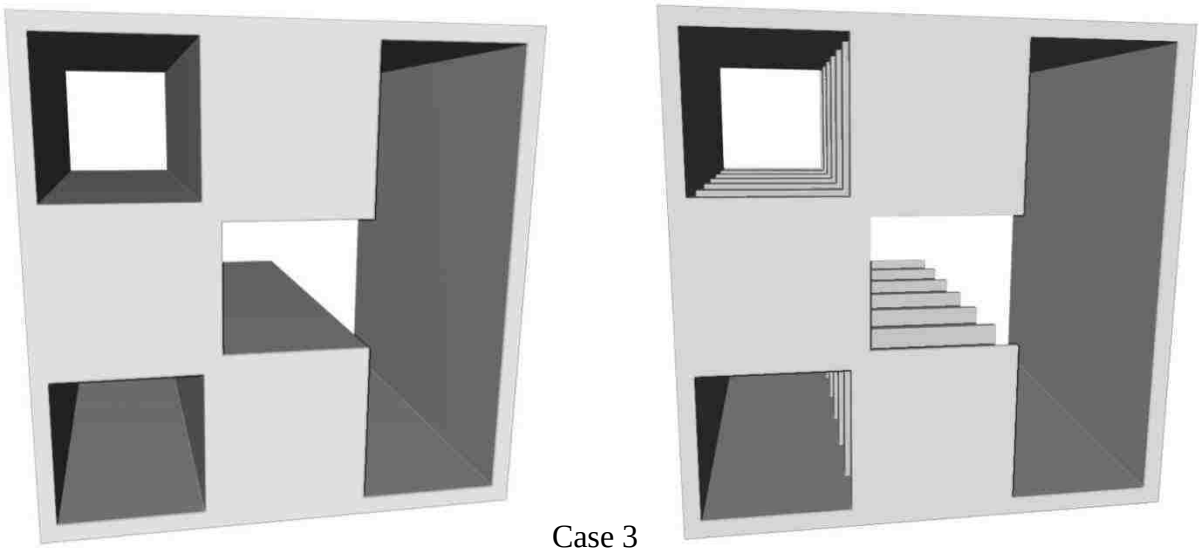

Case 3

(c) (c´)

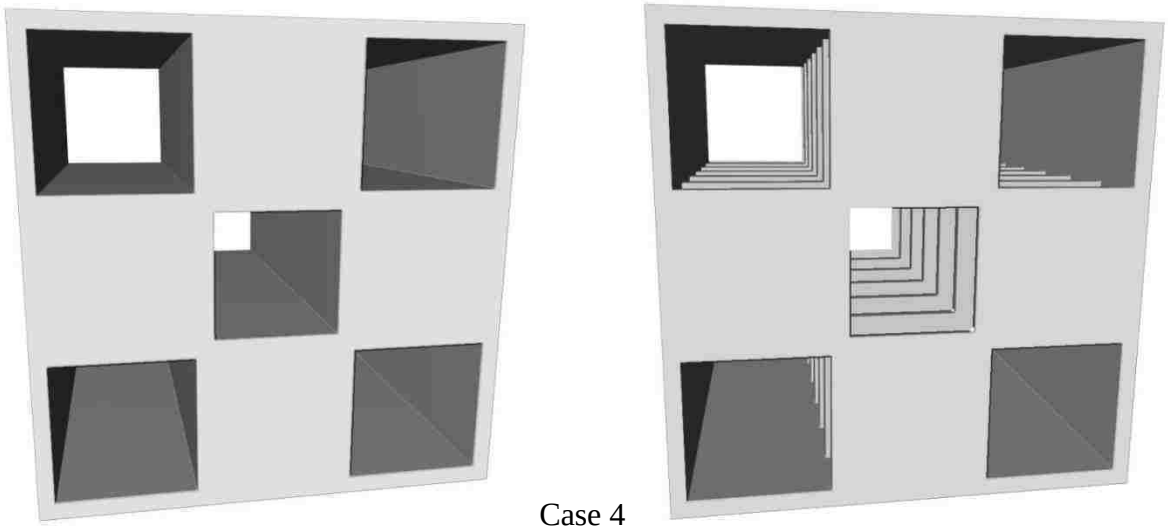

Case 4

(d) (d´)

Figure 4-15 (continued). Barriers with perpendicular orientation in respect to the fluid flow direction, a through d represent clay minerals without micropores and a´ through d´ represent clays with micropores.

To compare the different scenarios and derive a relation that can be applied to general pore throats, two dimensionless parameters were defined here;

$$\text{Dimensionless cross section area} = \frac{A_2}{A_1} \tag{4-1}$$

$$\text{Dimensionless flow rate} = \frac{Q_3 - Q_2}{Q_1} \tag{4-2}$$

1: Original image without clay increment

2: The case containing newly generated clay without microporosity

3: The case containing newly generated clay with microporosity

The dimensionless flow rate parameter actually shows the contribution of the micropores to the total flow rate. The results of flow rate calculations for the perpendicular barrier case are given in Table 4-5. The dimensionless cross sectional area versus dimensionless flow rate is shown in Fig. 4-16. The equation of the linear trend line is used to calculate the normalized flowrate for pore throats with the clay barriers, which is then used to update pore-throat conductances in the porous media with permeable micropores.

Table 4-5. Flow rate and dimensionless parameters for various cases of barrier arrangement. Barriers are perpendicular to the flow direction.

Case number	A_1 ($\times 10^4$ voxel^2)	A_2 ($\times 10^4$ voxel^2)	q_1 ($\times 10^6$ voxel^3/s)	q_2 ($\times 10^6$ voxel^3/s)	q_3 ($\times 10^6$ voxel^3/s)	A_2/A_1	$(q_3-q_2)/q_1$
1	7.84	6.84	7.7	3.5	3.71	0.872	0.023
2	7.84	5.84	7.7	1.28	1.46	0.745	0.023
3	7.84	4.84	7.7	0.81	0.93	0.617	0.016
4	7.84	3.84	7.7	0.35	0.41	0.490	0.009

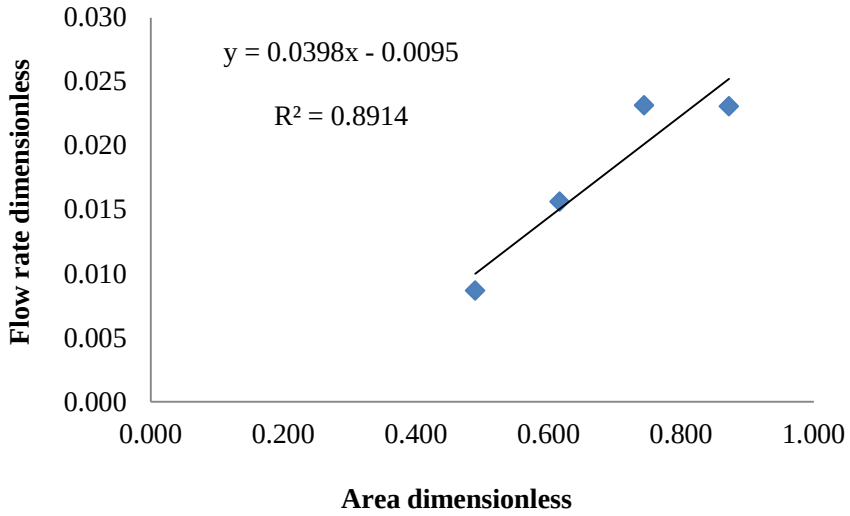

Figure 4-16. Normalized cross section area versus normalized flow rate for various cases of barrier arrangement. Barriers are perpendicular to the flow direction.

$$\frac{q_3 - q_2}{q_1} = 0.0398 \times \left(\frac{A_2}{A_1}\right) - 0.0095 \rightarrow q_3 = q_2 + q_1 \times \left[0.0398 \times \left(\frac{A_2}{A_1}\right) - 0.0095\right] \qquad (4\text{-}3)$$

4-5-2 Parallel barrier orientation

In this set of simulations barriers are located on four different walls of the open duct where they are parallel to the flow rate (4-17). The solid barriers (4-17, a through d) represent the clay minerals without micropores and the discrete barriers (4-17, a´ through d´) represent the clay minerals containing microporosity.

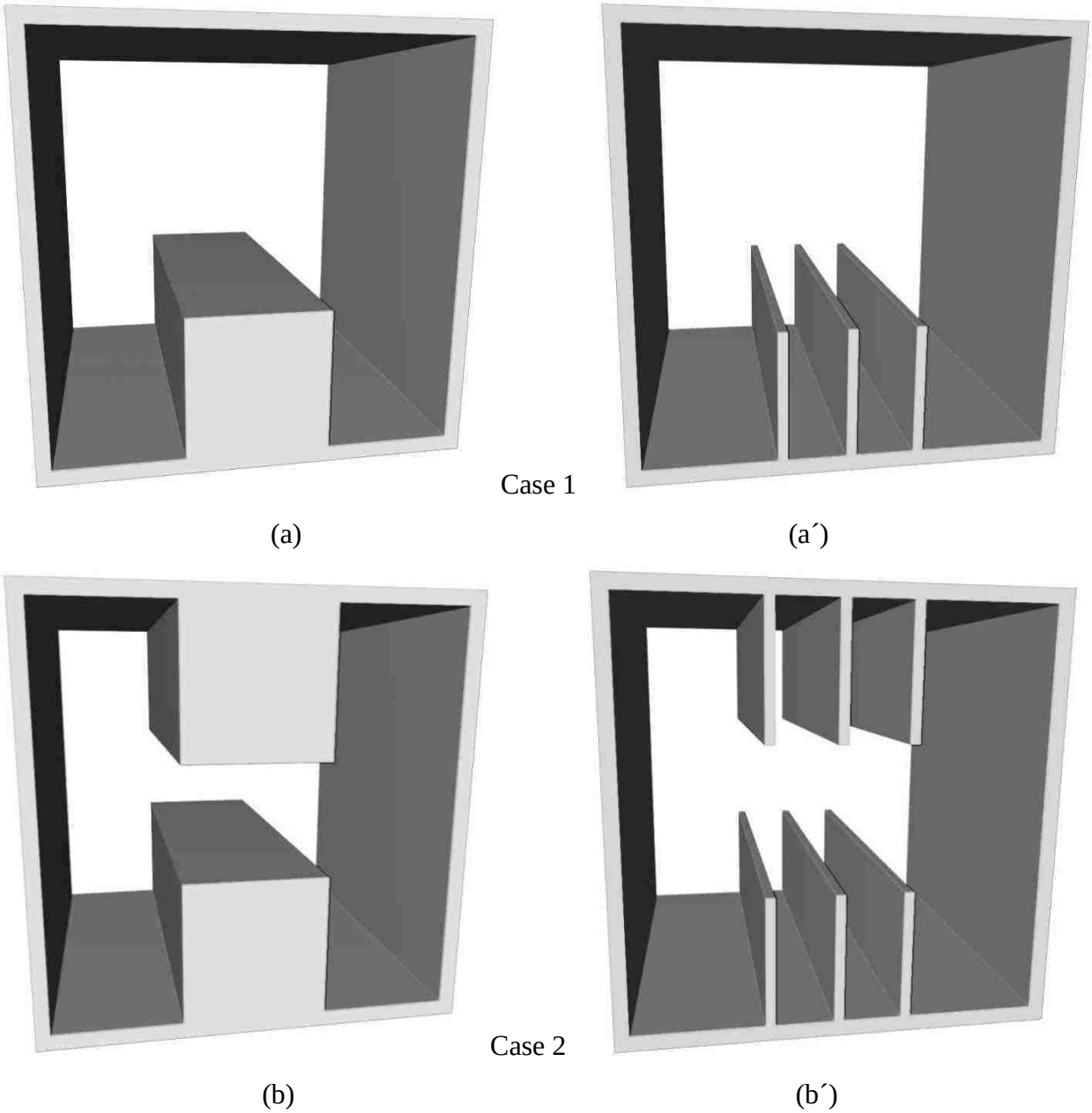

Case 1

(a) (a´)

Case 2

(b) (b´)

Figure 4-17. Barriers with parallel orientation in respect to the fluid flow direction, a through d represent clay minerals without micropores and a´ through d´ represent clays with micropores.

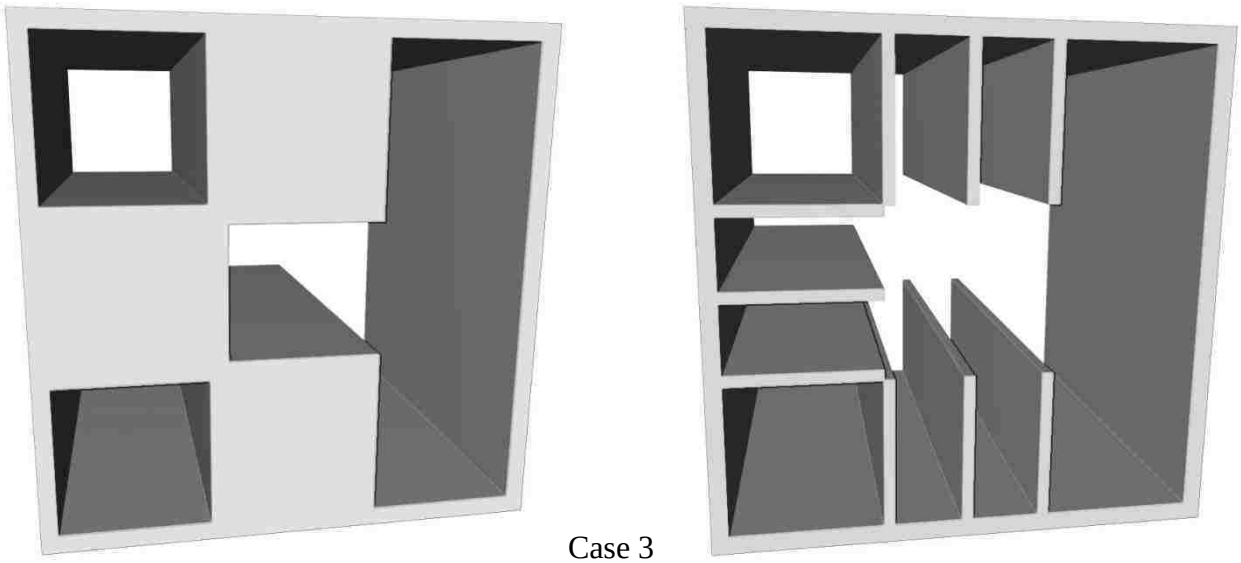

Case 3

(c) (c´)

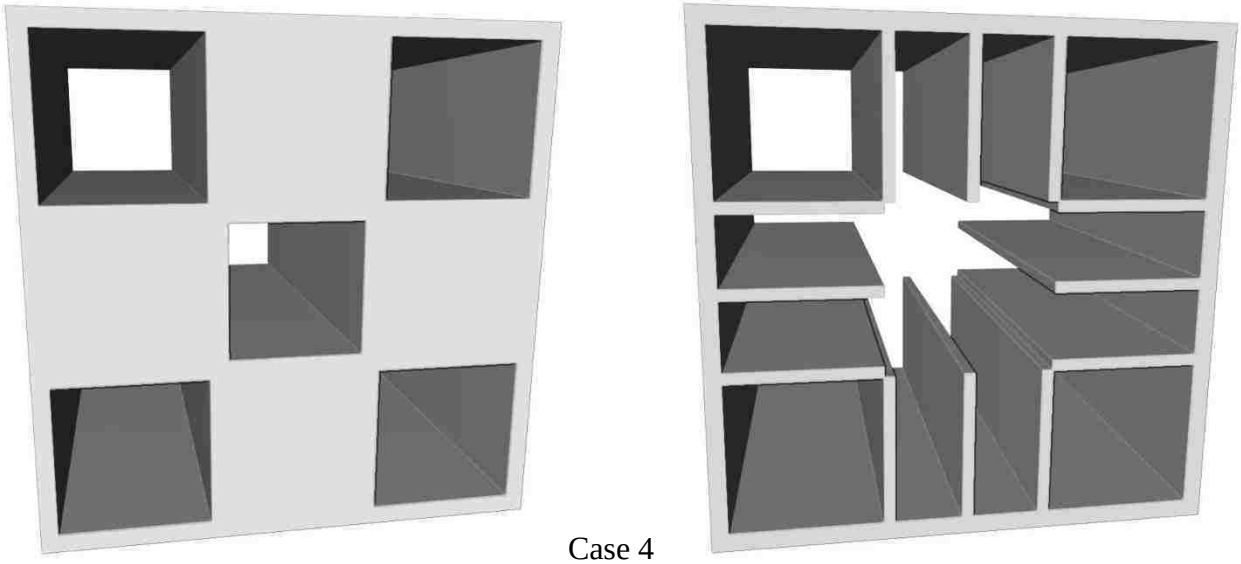

Case 4

(d) (d´)

Figure 4-17 (continued). Barriers with parallel orientation in respect to the fluid flow direction, a through d represent clay minerals without micropores and a´ through d´ represent clays with micropores.

The results of flow rate calculations for the parallel barrier case are given in Table 4-6. Dimensionless cross section area versus dimensionless flow rate was drawn in Fig. 4-18. The equation of the linear trend line is used to calculate the permeability of the case with microporosity.

Table 4-6. Flow rate and dimensionless parameters for various cases of barrier arrangement. Barriers are parallel to the flow direction.

Case number	A_1 ($\times 10^4$ voxel^2)	A_2 ($\times 10^4$ voxel^2)	q_1 ($\times 10^6$ voxel^3/s)	q_2 ($\times 10^6$ voxel^3/s)	q_3 ($\times 10^6$ voxel^3/s)	A_2/A_1	$(q_3-q_2)/q_1$
1	7.84	6.84	7.7	3.5	4.1	0.872	0.080
2	7.84	5.84	7.7	1.28	1.83	0.745	0.071
3	7.84	4.84	7.7	0.81	1.22	0.617	0.054
4	7.84	3.84	7.7	0.35	0.65	0.490	0.039

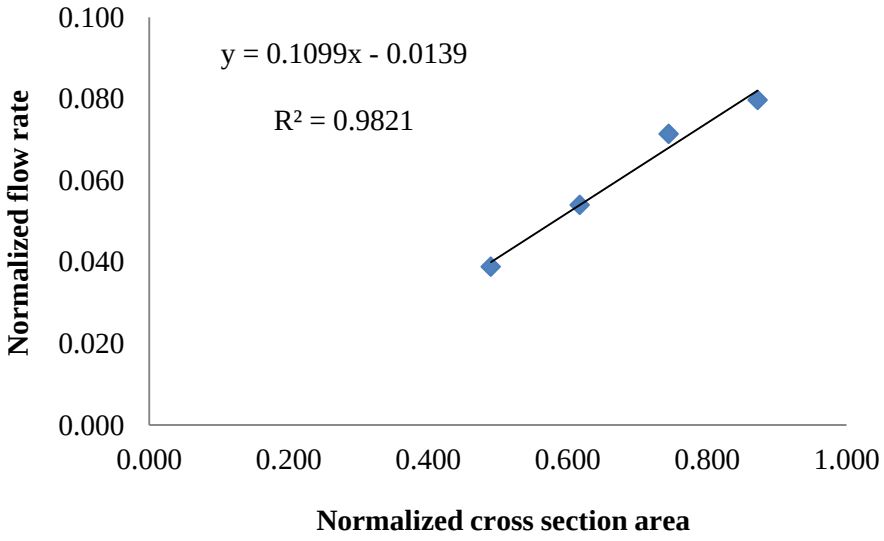

Figure 4-18. Normalized cross section area versus normalized flow rate for various cases of barrier arrangement. Barriers are parallel to the flow direction.

$$\frac{q_3 - q_2}{q_1} = 0.1099 \times \left(\frac{A_2}{A_1}\right) - 0.0139 \rightarrow q_3 = q_2 + q_1 \times \left[0.1099 \times \left(\frac{A_2}{A_1}\right) - 0.0139\right] \quad (4\text{-}4)$$

4-6 Applying the geochemical changes considering microporosity

In the previous section, two relations were derived to relate the contributed flow rate by micropores to the cross section area of throats for two different barrier orientations, equations 4-3 and 4-4. Flow rate is related to the throat conductivity through the following equation:

$$q_{ij} = \frac{g_{ij}}{\mu}(p_j - p_i) \quad (4\text{-}5)$$

Where q_{ij} is flow rate, g_{ij} is conductivity of throat, μ is viscosity, and p is pressure. The flow rate is proportional to the conductivity of the throat. Therefore, equations 4-4 and 4-5 can be rewritten to form equations 4-6 and 4-7 which relate the contributed conductivity from added clays to the cross section area of the throats.

Barriers perpendicular to flow direction: $g_3 = g_2 + g_1 \times \left[0.0398 \times \left(\frac{A_2}{A_1}\right) - 0.0095\right]$ (4-6)

Barriers parallel to flow direction: $g_3 = g_2 + g_1 \times \left[0.1099 \times \left(\frac{A_2}{A_1}\right) - 0.0139\right]$ (4-7)

In order to take the clay microporosity into account, twice the volume of clay predicted by geochemical models was added to the micro-CT images. This case can be viewed as the situation with 50 percent microporosity and zero permeability in micropores. Throat conductivities are then modified to consider the permeability of the clay micropores. In this algorithm the equivalent throats are mapped between the original image and the image containing newly generated clay with zero permeability in micropores. The ratio of cross sectional areas are calculated and using equation 4-6 or 4-7 the contribution of micropores to the throat conductivity is estimated. A new network file containing the modified throat conductivities is then created. This file is then used to calculate the image permeability considering a permeability for the clay micropores. A schematic drawing shown in Fig. 4-19, illustrates the employed procedure to consider the impact of the clay micropores in permeability calculations.

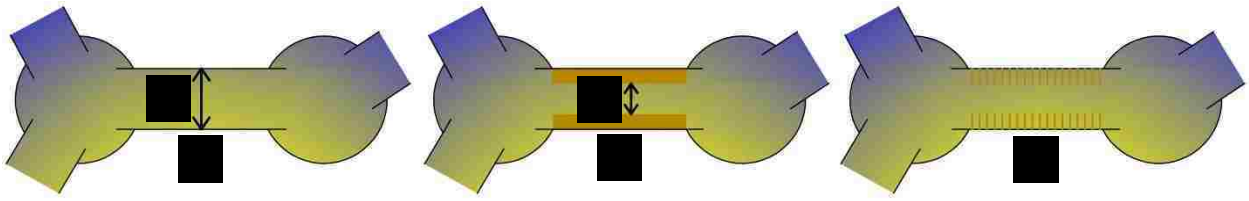

Figure 4-19. A schematic illustrates the employed procedure to consider the impact of clay micropores in permeability calculations.

According to the results given in Table 3-5, the geochemical changes were applied to the core micro-CT images. For sample 59, feldspar was decreased from 10.78 to 7.32 percent. The

quartz fraction was increased from 65.85 to 66.49 percent. Clay voxels were added in two layers on feldspar grains and one layer on quartz grains. This process is led to adding 4.74 percent newly generated clay voxels. Assuming 50 percent microporosity, the actual amount of newly generated clay minerals will be 2.37 percent which is in accordance to the geochemical modeling results (Table 3-12). Figure 4-20 shows sample 59 before and after applying the geochemical changes.

In a similar manner, the geochemical changes were applied to samples 61 and 62. Figures 4-21 and 4-22 show samples 61 and 62 respectively, before and after applying the geochemical changes. The permeabilities of the altered images were calculated using the CLF code. The rock composition and permeability of the samples before and after alteration are given in Tables 4-7 to 4-9.

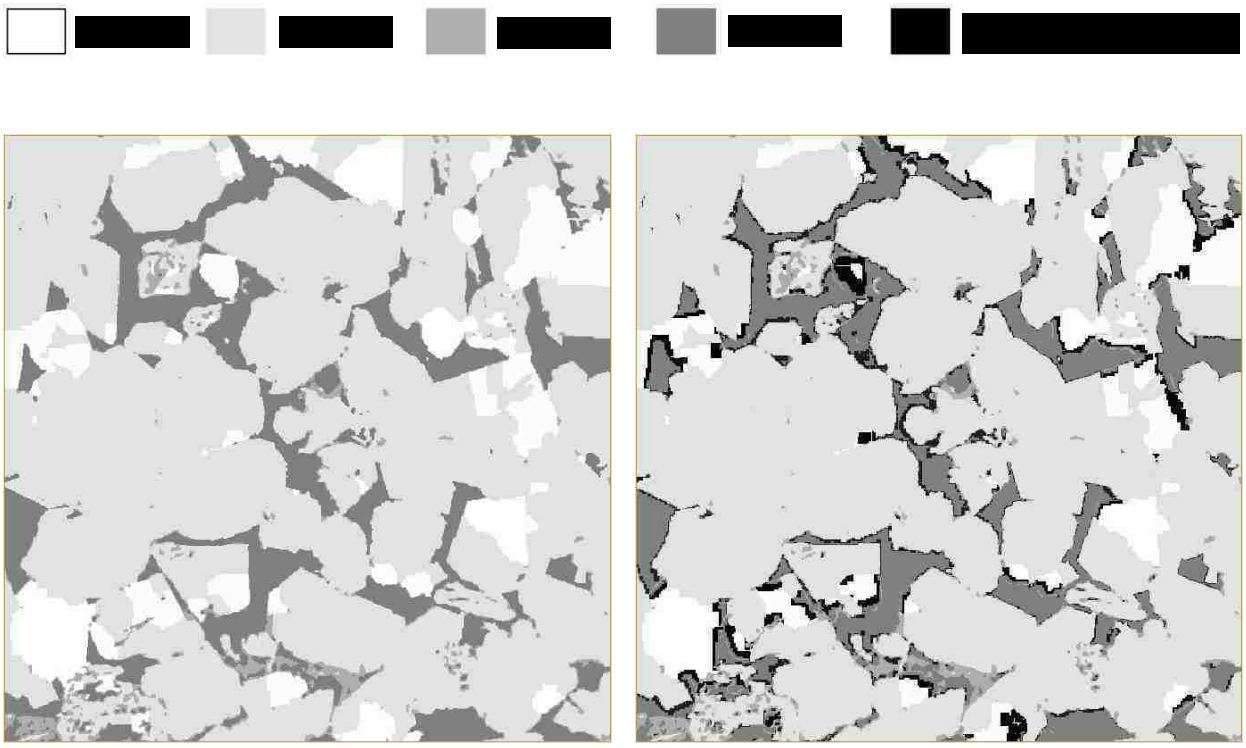

(a) (b)

Figure 4-20. Application of the geochemical changes to the image sample 59 considering clay microporosity. (a) Initial, (b) Altered.

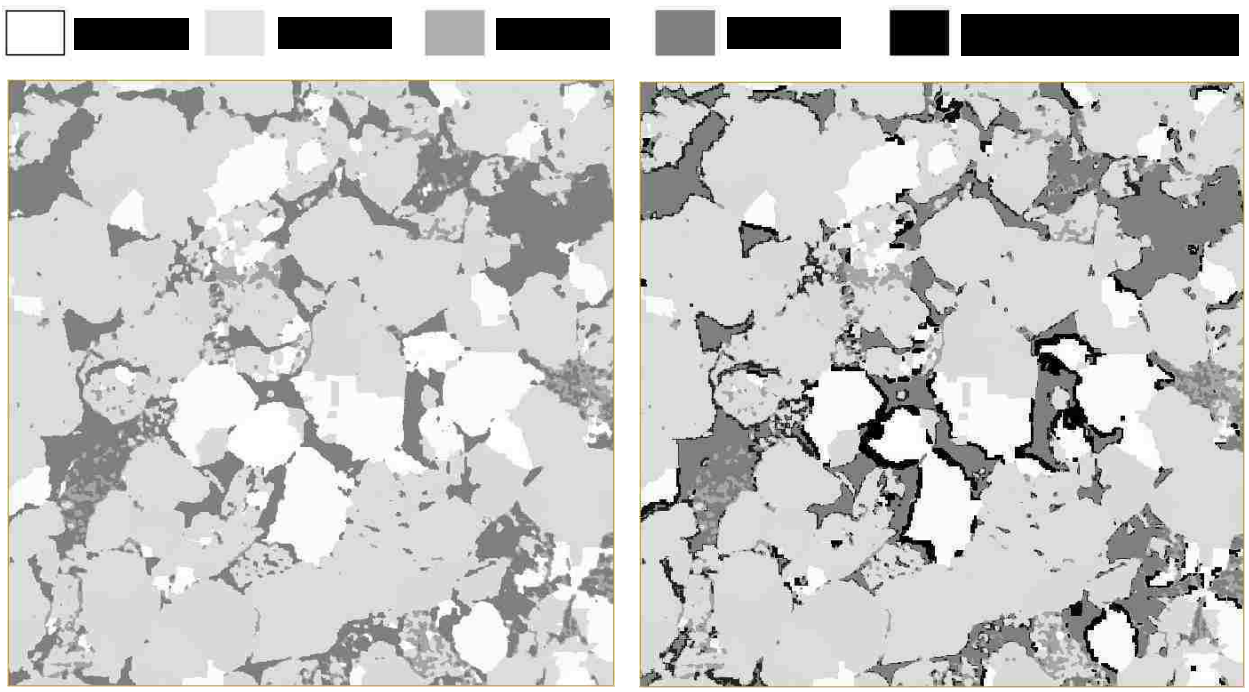

(a) (b)

Figure 4-21. Application of the geochemical changes to the image sample 61 considering clay microporosity. (a) Initial, (b) Altered.

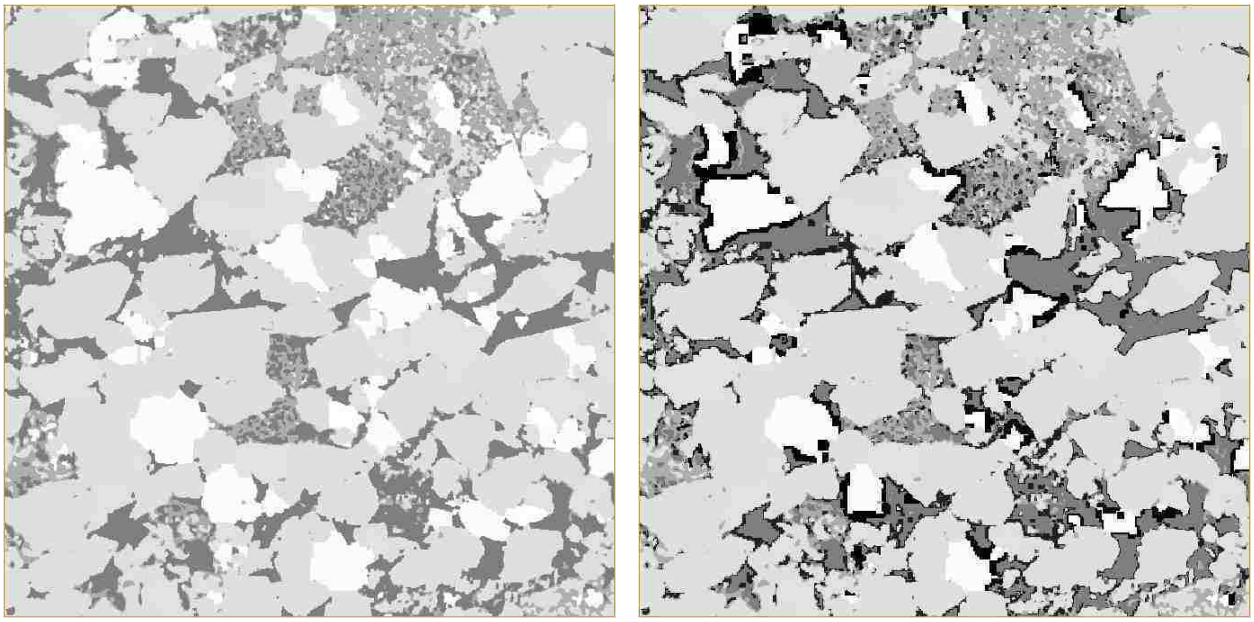

(a) (b)

Figure 4-22. Application of the geochemical changes to the image sample 62 considering clay microporosity. (a) Initial, (b) Altered.

In these altered images, the network of sample 59 has 39,741 pores and 144,057 throats. These numbers for sample 61 are 53,847 and 191,658, respectively. In the network 62 the pore number is 81,622 and throat number is 247,681 (Appendix D).

Table 4-7. The rock composition (volume percent) and permeability (mD) for sample 59, before and after alteration considering microporosity.

Sample No.	Initial	Altered, clay is not microporous	Altered, microporous but impermeable clay	Altered, microporous permeable clay (Micropores **parallel** to the flow direction)	Altered, microporous permeable clay (Micropores **perpendicular** to the flow direction)
Clays	5.58	5.58	5.58	5.58	5.58
Feldspar	10.78	7.32	7.32	7.32	7.32
Quartz	65.85	66.49	66.49	66.49	66.49
Newly generated clay	0	2.35	4.74	4.74	4.74
Porosity	17.79	18.26	15.87*	15.87*	15.87*
Permeability, x direction	3216	2679	1416	1481	1436
Permeability, y direction	2472	2089	1065	1114	1080
Permeability, z direction	2043	1779	899	938	911
Permeability, geometric mean	**2532**	**2151**	**1106**	**1157**	**1122**
Permeability ratio (k/k_0)	**1**	**0.85**	**0.44**	**0.46**	**0.44**

*Adding 50 percent clay microporosity, the total porosity will be 18.24.

Table 4-8. The rock composition (volume percent) and permeability (mD) for sample 61, before and after alteration considering microporosity.

Sample No.	Initial	Altered, clay is not microporous	Altered, microporous but impermeable clay	Altered, microporous permeable clay (Micropores **parallel** to the flow direction)	Altered, microporous permeable clay (Micropores **perpendicular** to the flow direction)
Clays	6.40	6.40	6.40	6.40	6.40
Feldspar	14.49	10.92	10.92	10.92	10.92
Quartz	61.39	61.90	61.90	61.90	61.90
Newly generated clay	0	2.38	5.37	5.37	5.37
Porosity	17.72	18.40	15.40*	15.40*	15.40*
Permeability, x direction	1271	1122	636	666	645
Permeability, y direction	1277	1104	810	848	823
Permeability, z direction	1118	981	616	642	624
Permeability, average	**1220**	**1067**	**682**	**713**	**692**
Permeability ratio (k/k_0)	**1**	**0.87**	**0.56**	**0.58**	**0.57**

*Adding 50 percent clay microporosity, the total porosity will be 18.09.

Table 4-9. The rock composition (volume percent) and permeability (mD) for sample 62, before and after alteration considering microporosity.

Sample No.	Initial	Altered, clay is not microporous	Altered, microporous but impermeable clay	Altered, microporous permeable clay (Micropores **parallel** to the flow direction)	Altered, microporous permeable clay (Micropores **perpendicular** to the flow direction)
Clays	8.21	8.21	8.21	8.21	8.21
Feldspar	13.12	7.38	7.38	7.38	7.38
Quartz	64.09	65.16	65.16	65.16	65.16
Newly generated clay	0	3.69	7.00	7.00	7.00
Porosity	14.58	15.56	12.26*	12.26*	12.26*
Permeability, x direction	608	590	238	246	240
Permeability, y direction	525	519	200	206	201
Permeability, z direction	533	538	227	235	229
Permeability, average	**554**	**549**	**221**	**228**	**223**
Permeability ratio (k/k_0)	**1**	**0.99**	**0.40**	**0.41**	**0.40**

*Adding 50 percent clay microporosity, the total porosity will be 15.76.

4-7 Discussion

A severe formation permeability reduction due to the growth of diagenetic clay was reported previously by Nadeau (1998), even at very low clay content. Simulating the natural diagenetic changes in a reservoir in a laboratory is expensive and time consuming. The goal of our research here was to establish a procedure to predict the reservoir permeability changes due to diagenetic alterations. Pore network modeling was utilized to quantify the impact of rock-brine geochemical reactions on permeability. The geochemical changes were applied to the micro-CT scan images of core samples using a computer code. The permeability changes, then, were calculated using another computer code.

The geochemical modeling results discussed in chapter 3 show mainly a decrease in feldspar content and an increase in the clay portion. In the first investigated scenario, the newly generated clay minerals due to geochemical reactions were added to the micro-CT images as solid voxels without considering any microporosity. The permeability calculations show almost 15 percent decrease in permeability for sample 59, from 2532 to 2151 mD. The permeability decrease for samples 61 and 62 are 12 and 1 percent, respectively (Fig. 4-23).

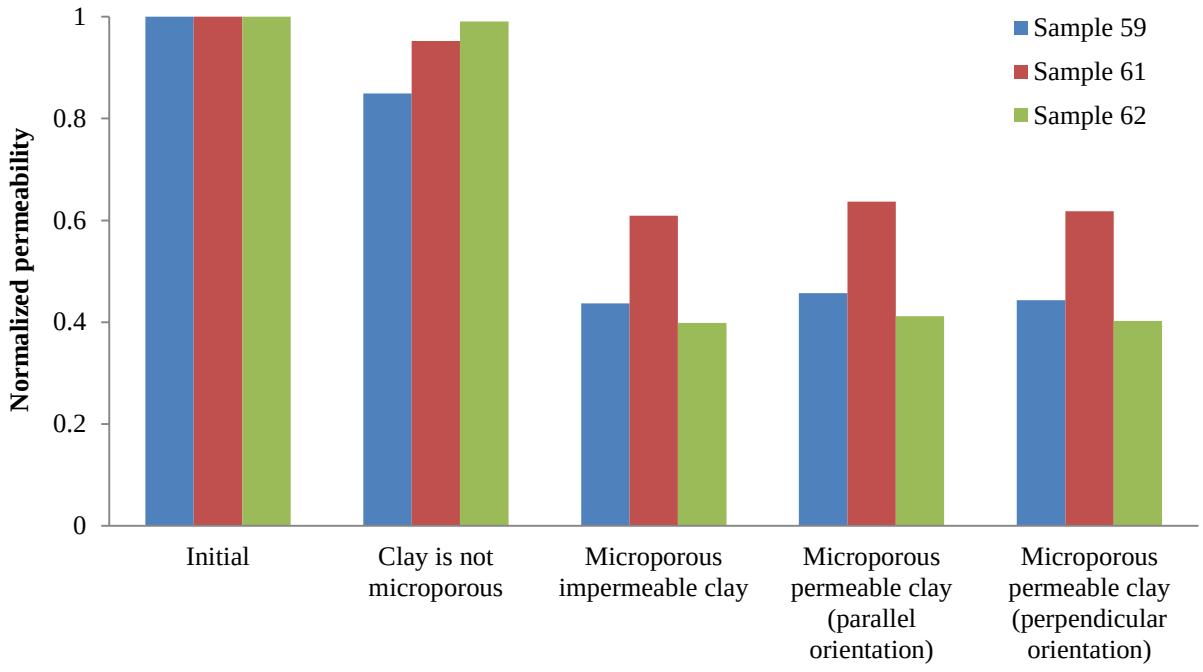

Figure 4-23. Calculated permeability changes due to the anticipated geochemical changes.

To model the natural occurrence of clay minerals more accurately, the microporosity of clay minerals was considered in the second set of calculations. To take the impact of microporosity into account, twice the expected clay mineral volume was added to the images, assuming 50 percent microporosity. Calculations show a severe permeability damage in all three core samples. Assuming no permeability for the clay micropores, the permeability of sample 59 was dropped from 2532 to 1106 mD, showing 56 percent permeability reduction. The permeability damage of samples 61 and 62 in this case, were 44 and 60 percent, respectively (Fig. 4-23).

To consider the permeability of micropores more accurately, the conductivity of throats were modified using a computer code, developed in this study, to consider the contributed conductivity by micropores. Two cases were considered for micropores to be perpendicular and parallel to the flow rate direction. The permeability of sample 59 was dropped from 2532 to 1122 mD, showing 56 percent permeability reduction, where micropores were perpendicular to the flow rate. The permeability damage of samples 61 and 62 for the same orientation of micropores, were 43 and 60 percent, respectively. For the parallel orientation of micropores to flow rate, the permeability reductions are 54, 42, and 59 for samples 59, 61, and 62, respectively (Fig. 4-23).

It is worth noting that in all discussed permeability reduction cases, not only did porosity not decrease, but also a slight increase in porosity occurred. That means that even with the same pore space, permeability can change with changing the pore structure. The growth of clay minerals in some parts of a rock can reduce the throats cross section area and conductivity in specific points and change the fluid flow pattern through the porous media. In the studied samples here, the number of pores and throats with the smaller diameter was increased after altering the images and adding newly generated clay to the images (Appendix D). Applying an empirical formula to relate porosity to permeability, hence, is not always an accurate way to investigate the permeability variations.

Reservoir permeability damage can lead to a serious production drop, which may endanger the whole project economically. In the studied geothermal case here, a 50 percent permeability damage may cause a considerable work load increase on the injection pumps. With increasing the consumed energy by pumps, a bigger part of the produced electricity will be spent in the energy production process.

The application of this procedure is not limited to the geothermal reservoirs. Any geochemical alteration in a reservoir can initiate new geochemical reactions inside the reservoir. These reactions may change the rock composition and therefore change the reservoir permeability and porosity. Utilizing such a procedure can provide better estimations about the permeability alteration in life span of a project and help to employ a suitable approach to prevent potential permeability damage.

Chapter 5
Conclusions and Future research

5-1 Conclusions

1. Theoretical calculations in which reacting a brine from the Cossinade field, Vermilion Parish, LA, with a rock composition from previous studies and also a brine from Chocolate Bayou, TX, with the rock composition of core samples from Pleasant bayou, TX, results in a calculated increase in clay minerals of about 3 percent by volume. This increase occurs over a wide variation in pH, and bicarbonate concentrations. A similar increase is observed when using two different thermodynamic data bases.
2. The modeling shows that the initial observed assemblage of albite, illite, chlorite and smectite would be expected to alter to a mixture of smectite-like minerals (nontronite and saponite) and illite-like minerals (muscovite and paragonite). Continued alteration of albite to paragonite and quartz occurs with each additional reaction step. The presence of pure nontronite, saponite, muscovite and paragonite is not expected in a natural setting, but are proxies for actual expandable and non-expandable clay minerals for which free energy data is not available.
3. Kinetic modeling shows that the increase in clay content can be expected to occur within a time span of approximately 70 years, close to the expected lifespan of a geothermal power plant.
4. The exact clay minerals formed vary depending on the data base, which minerals are allowed to form in the reactions, and the temperature.
5. The increase in total clay is primarily the result of albite altering to clay. The exact clay mineral formed depends on the variables described in (4). High sodium content in the brine reduces the amount of clay formed by reversing the albite to clay transformation.
6. A temperature drop may cause precipitation inside the heat exchanger. The impact of this on the heat exchanger will vary with flow rates and the concentration of dissolved sodium

and other ions in the fluid. An increase in brine salinity will increase the risk of precipitation in heat exchangers dramatically.

7. Geochemical reactions may have an important impact on petrophysical properties of a reservoir, such as porosity and permeability.
8. Diagenetic clay minerals, naturally occurring or a result of flow induced by a geothermal project may cause a severe permeability damage, even at low content, considering their crystal morphology and microporosity.
9. With a constant or even an increasing porosity, a reduction in permeability is possible. Applying an empirical formula to relate porosity to permeability, therefore, is not always an accurate way to investigate the potential permeability variations.
10. Reservoir permeability damage can lead to a serious production drop, which may endanger the whole project economically. Utilizing such a studied procedure can provide better estimations on the permeability alteration in life span of a project and help to employ a suitable approach to prevent a potential permeability damage.

5-2 Future research

Experimental work to validate the modeling, especially the kinetics, is recommended as a future study. Reservoir simulation, considering the predicted permeability damage, can be the next step to understand the reservoir behavior in life span of the project. The reservoir modeling results can then be used to conduct an economic study.

Further investigations are recommended for a better understanding of the impact of the clay micropores on permeability and flow pattern. Different clay minerals and various crystal morphologies need to be considered to make a more general conclusion.

Bibliography

Alekseyev, V. A., (2007), "Equations for the Dissolution Reaction Rates of Montmorillonite, Illite, and Chlorite", Geochemistry International, Vol. 45, No. 8, 770–780.

Ausburn, M.E., (2013), "Controls on the Composition of Saline Formation Waters from Coastal and Offshore Louisiana", Master's Thesis, Louisiana State University, 95p. (http://etd.lsu.edu/docs/available/etd-05302013-141118/unrestricted/Ausburn_thesis.pdf)

Ausburn, M.E., and Hanor, J.S., (2013), "Geochemical Characterization of Formation Waters and Sediments from an Area of South-Central Louisiana with Implications for Geothermal Energy Production", GCAGS/GCSSEPM Transactions, Vol. 63, 67-77.

Berner, R.A., (1971), "Principles of Chemical Sedimentology", McGraw-Hill, 240p.

Bethke, C.M., (2008), "Geochemical and Biogeochemical Reaction Modeling (Second Edition)", Cambridge University press, 543p.

Bethke, C.M. and Yeakel, S., (2012), "Reaction Modeling Guide", Aqueous Solutions, LLC, 162p.

Bhattad, P., Willson, C.S., Thompson, K.E., (2011), "Effect of Network Structure on Characterization and Flow Modeling Using X-ray Micro-Tomography Images of Granular and Fibrous Porous Media", Transport in Porous Media, Vol. 90, 363-391.

Blondes, M.S., Gans, K.D., Thordsen, J.J., Reidy, M.E., Thomas, B., Engle, M.A., Kharaka, Y.K., and Rowan, E.L., (2014), "U.S. Geological Survey National Produced Waters Geochemical Database v2.1", http://energy.usgs.gov

Boas, F.E., and Fleischmann, D., (2012), "CT artifacts: Causes and reduction techniques", Imaging in Medicine, Vol. 4, No. 2, 229-240.

Burton, J.H., Krinsley, D.H., and Pye, K., (1987), "Authigenesis of Kaolinite and Chlorite in Texas Gulf Coast Sediments", Clays and Clay Minerals, Vol. 35, No. 4, 291-296.

Carver, R.E., (1971), "Procedures in Sedimentary Petrology", Wiley-Interscience, 653p.

Dobson, R. J., Hartsock, J. H., McCoy, R. L., and Rodgers, J. A., (1980), "Investigation and Evaluation of Geopressured-Geothermal Wells - Final Report, Beulah Simon No. 2 Well, Vermilion Parish, Louisiana, Volume I: Completion and Testing", Gruy Federal, Inc., Houston, Texas.

Dullien, F.A.L., (1979), "Porous Media, Fluid Transport and Pore Structure", Academic Press, 396p.

Federal Highway Administration, (1991), "Rock and Mineral Identification for Engineers", U.S. Department of Transportation, 50p.

FEI, (2016), Avizo 3D Software, [ONLINE] Available at: http://www.fei.com/software/avizo3d/, [Accessed 18 March 2016].

Frank-Kamenetskii, V.A., Kotov, N.V., and Rjumin, A.A., (1980), "The Transformation of Feldspar and Muscovite to Clay Minerals in (Ca, Mg)-Carbonated Bearing Hydrothermal Media", Clay Minerals, Vol. 15, 263-274.

Flukiger, F., Bernard, D., (2009), "A new numerical model for pore scale dissolution of calcite due to CO_2 saturated water flow in 3D realistic geometry: Principles and first results", Chemical Geology, Vol. 265, 171–180.

Gallup, D.L., (2009), "Production engineering in geothermal technology: A review", Geothermics, Vol. 38, 326–334.

Geothermal Energy Association, (2015), "Annual U.S. & Global Geothermal Power Production Report", Geo-Energy.org.

Gharrabi, M., Velde, B., and Sagon, J.P., (1998), "The Transformation of Illite to Muscovite in Pelitic Rocks: Constraints from X-Ray Diffraction", Clays and Clay Minerals, Vol. 46, No. 1, 79-88.

Goyal, K.P., and Conant, T.T., (2010), "Performance history of The Geysers steam field, California, USA", Geothermics, Vol. 39, 321–328.

Gray, T.A., (2010), "Geothermal Resource Assessment of the Gueydan Salt Dome and the Adjacent Southeast Gueydan Field, Vermilion Parish, Louisiana", Master's Thesis, Louisiana State University, 76p, (http://etd.lsu.edu/docs/available/etd-06092010-150854/unrestricted/TaylorGray_Thesis.pdf).

Hunziker, J.C., Frey, M., Clauer, N., Dallmeyer, R.D., Friedrichsen, H., Flehmig, W., Hochstrasser, K., Roggwiler, P., and Schwander, H., (1986), "The Evolution of Illite to Muscovite: mineralogical and Isotopic Data from the Glarus Alps, Switzerland", Contributions to Mineralogy and Petrology, Vol. 92,157-180.

ImageJ, (2011), ImageJ, [ONLINE] Available at: https://imagej.nih.gov/ij/download.html, [Accessed 18 March 2016].

Kang, Q., Zhang, D., Chen, S., (2003), "Simulation of dissolution and precipitation in porous media", Journal of Geophysical Research, Vol. 108, No. B10, 2505.

Kang, Q.J., Lichtner, P.C., Zhang, D.X., (2006), "Lattice Boltzmann pore-scale model for multicomponent reactive transport in porous media", Journal of Geophysical Research, Vol. 111, No. B05203.

Kang, Q., Lichtner, P., Viswanathan, H., Abdel-Fattah, A., (2010), "Pore scale modeling of reactive transport involved in geologic CO_2 sequestration", Transport in Porous Media, Vol. 82, 197‑213.

Kim, D., Peters, C.A., Lindquist, W.B., (2011), "Upscaling geochemical reaction rates accompanying acidic CO_2-saturated brine flow in sandstone aquifers", Water Resources Research, Vol. 47, No. W01505.

Klinkenberg, L.J. (1941), "The Permeability of Porous Media to Liquids and Gases", Drilling and Production Practice, Vol. 200.

Knauss, K.G. and Wolery, T.J., (1986), "Dependence of albite dissolution kinetics on pH and time at 25 °C and 70 °C", Geochimica et Cosmochimica Acta, Vol. 50, 2481-2497.

Land, L.S., and Milliken, K.L., (1981), "Feldspar diagenesis in the Frio Formation, Brazoria County, Texas Gulf Coast", Geology, Vol. 9, 314-318.

Lane, N. and K. E. Thompson, (2010), "Image-Based Pore-Scale Modeling Using the Finite Element Method", Advances in Computed Tomography for Geomaterials, GeoX 2010 ISTE/Wiley, 295-303.

Li, L., Peters, C.A., Celia, M.A., (2006), "Upscaling geochemical reaction rates using pore-scale network modeling", Advances in Water Resources, Vol. 29, 1351‑1370.

Lynch, F.L., (1996), "Mineral/Water Interaction, Fluid Flow, and Frio Sandstone Diagenesis: Evidence from the Rocks", AAPG Bulletin, Vol. 80, No. 4, 486–504.

Lynch, F.L., (1997), "Frio Shale Mineralogy and the Stoichiometry of the Smectite-to-Illite Reaction: the Most Important Reaction in Clastic Sedimentary Diagenesis", Clays and Clay Minerals, Vol. 45, No. 5, 618-613.

Mitchell, J.K., and Soga, K., (2005), "Fundamentals of Soil Behavior", John Wiley & Sons, 577p.

Molins, S., Trebotich, D., Steefel, C.I., Shen, C., (2012), "An investigation of the effect of pore scale flow on average geochemical reaction rates using direct numerical simulation. Water Resources Research, Vol. 48.

Molins, S., Trebotich, D., Yang, L., Ajo-Franklin, J.B., Ligocki, T.J., Shen, C., Steefel, C.I., (2014), "Pore-scale controls on calcite dissolution rates from flow-through laboratory and numerical experiments", Environmental Science and Technology, Vol. 48, 7453‑7460.

Moore, D.M., and Reynolds, R.C., (1989), "X-ray diffraction and the identification and analysis of clay minerals", Oxford University Press, 332p.

Morris K.A., and Shepperd C.M., (1982), "The Role of Clay Minerals in Influencing Porosity and Permeability characteristics in the Bridport Sands of Wytch Farm, Dorset", Clay Minerals, Vol. 17, 41-54.

Nadeau, P.H., (1998), "An Experimental Study of the Effects of Diagenetic Clay Minerals on Reservoir Sands", Clays and Clay Minerals, Vol. 46, No. 1, 18-26.

Neasham, J.W., (1977), "The Morphology of Dispersed Clay in Sandstone Reservoirs and its Effect on Sandstone Shaliness, Pore Space and Fluid Flow Properties", 52nd Annual Fall Technology Conference and Exhibition of the Society of Petroleum Engineers of AIME, Denver, Colorado.

Perona, P., Malik, J., "Scale-Space and Edge Detection Using Anisotropic Diffusion", IEEE Transactions on Pattern Analysis and Machine Intelligence, Vol. 12, No. 7, 629-639.

Pokrovsky, O.S., Golubev, S.V., Schott, J., and Castillo, A., (2009), "Calcite, Dolomite and Magnesite Dissolution Kinetics in Aqueous Solutions at Acid to Circumneutral pH, 25 to 150 °C

and 1 to 55 atm pCO_2: New Constraints on CO_2 Sequestration in Sedimentary Basins", Chemical Geology, Vol. 265, 20-32.

PoreSim, (2005), PoreSim Research Consotium, [ONLINE] Available at: http://www.poresim.org/, [Accessed 18 March 2016].

Raith, M.M., Raase, P., and Reinhardt, J., (2011), "Guide to Thin Section Microscopy", e-book, 107p.

Rimstidt J. D., and Barnes H. L., (1980), "The Kinetics of Silica–Water Reactions", Geochimica et Cosmochimica Acta, Vol. 44, 1683–1699.

Ruska Permeameter Operating Manuals 1011-801, Ruska Instrumentation Corporation, Houston, TX.

Savagea, D., Noyb, D., and Mihara, M., (2002), "Modelling the Interaction of Bentonite with Hyperalkaline Fluid", Applied Geochemistry, Vol. 17, 207–223.

Sears, S.O., (1983), "Porcelaneous Cement and Microporosity in California Miocene Turbidites – Origin and Effect on Reservoir Properties", Journal of Sedimentary Petrology, Vol. 54, No. 1, 159-169.

Senkayi, A.L., Dixon, J.B., and Hossner, L.R., (1981), "Transformation of Chlorite to Smectite through Regularly Interstratified Intermediates", Soil Science Society of America Journal, Vol. 45, No. 3, 650-656.

Smith, M.M., and Carroll, S.A., (2014), "Experimental Determination of Chlorite Kinetics at Geothermal Conditions", PROCEEDINGS, Thirty-Ninth Workshop on Geothermal Reservoir Engineering Stanford University, Stanford, California, February 24-26.

Szalkowski, D.S, (2003), “Low Salinity Waters in Deep Sedimentary Basins”, Master's thesis, Louisiana State University, 238p, (http://etd.lsu.edu/docs/available/etd-0407103-225827/unrestricted/Szalkowski_thesis.pdf).

Szalkowski, D.S, and Hanor, J.S., (2003), “Spatial Variations in the Salinity of Produced Waters from Southwestern Louisiana”, GCAGS/GCSSEPM Transactions, Vol. 53, 798-806.

Tartakovsky, A.M., Meakin, P., Scheibe, T.D., Wood, B.D., (2007), “A smoothed particle hydrodynamics model for reactive transport and mineral precipitation in porous and fractured porous media”, Water Resources Research, Vol. 43, No. 5.

Tartakovsky, A.M., Redden, G., Lichtner, P.C., Scheibe, T.D., Meakin, P., (2008), “Mixing-induced precipitation: Experimental study and multiscale numerical analysis”, Water Resources Research, Vol. 44.

Thibodeaux, T.W., Sheng, Q., Thompson, K.E., (2014), “Rapid Estimation of Essential Porous Media Properties Using Image-Based Pore-Scale Network Modeling”, Industrial and Engineering Chemistry Research, Vol. 54, No. 16, 4474-4486.

Thompson, K.E., C.S. Willson, Zhang, W., (2006), “Quantitative computer reconstruction of particulate materials from microtomography images”, Powder Technology, Vol. 163, 169–182.

Thompson, K.E., C.S. Willson, C.D. White, S.L. Nyman, J.P. Bhattacharya, and A.H. Reed, (2008), “Application of a new grain-based reconstruction algorithm to microtomography images for quantitative characterization and flow modeling,” SPE Journal, Vol. 13, No. 2, 164-176.

Tiab, D., and Donaldson, E.C., (2012), “Petrophysics; Theory and Practice of Measuring Reservoir Rock and Fluid Transport Properties”, Third Edition, Elsevier, 950p.

Torsæter, o., and Abtahi, M., (2000), "Experimental Reservoir Engineering Laboratory Work Book", Department of Petroleum engineering and Applied Geophysics Norwegian University of Science and Technology.

Tyagi, M., Feng., Y., White, C.D., (2015), "A Downhole Heat Exchanger For Horizontal Wells In Low-Enthalpy Geopressured Geothermal Brine Reservoirs", Geothermics, Vol. 53, 368-378.

Ungemach, P., (2003), "Reinjection of Cooled Geothermal Brines into Sandstone Reservoirs", Geothermics, Vol. 32, 743–761.

Verdel, C., van der Pluijm, B.A., and Niemi, N., (2012), "Variation of Illite/Muscovite $^{40}Ar/^{39}Ar$ Age Spectra during Progressive Low-Grade Metamorphism: An Example from the US Cordillera", Contributions to Mineralogy and Petrology, Vol. 164, 521-536.

Welton, J.E., (2003), "SEM Petrology Atlas", Methods in Exploration Series No. 4 published by The American Association of Petroleum Geologists.

Whitney, G., (1983), "Hydrothermal Reactivity of Saponite", Clays and Clay Minerals, Vol. 31, No. 1, 1-8.

Yoon, H., Valocchi, A.J., Werth, C.J., and Dewers, T., (2012), "Pore-Scale Simulation of Mixing-Induced Calcium Carbonate Precipitation and Dissolution In a Microfluidic Pore Network', Water Resources Research, Vol. 48, 1-11.

Yoon, H., Kang, Q., and Valocchi, A.J., (2015), "Lattice Boltzmann-Based Approaches for Pore-Scale Reactive Transport", Reviews in Mineralogy and Geochemistry, Vol. 80, 393-431.

Zen, E-an., Albee, A.L., (1964), "Coexistent Muscovite and Paragonite in Pelitic Schists", The American Mineralogist, Vol. 49, 904-925.

Appendix A - Sensitivity analysis

A.1 Impact of different temperature drops

To investigate the impact of temperature on the calculated results, rock-brine reactions were modeled with different reservoir and heat exchanger output temperatures, using the similar approach as described in section 3-5. The results are shown in Table A.1. For all cases similar increases in clay content were obtained.

Table A.1. Investigated temperatures and clay volume percent in temperature sensitivity analysis of minerals transformations.

Reservoir temperature	Heat exchanger output temperature	Initial clay volume percent	Clay volume percent after reactions
130	100	10.5	13.49
150	120	10.5	13.55
170	140	10.5	13.43
130	80	10.5	13.49
130	60	10.5	13.49

A.2 Impact of pH

As shown in Table 2, the brine pH for the study area is 6.61. To study the impact of brine pH on the observed results, rock-brine interactions were modeled with two different pHs of 5.61 and 4.61. In both cases similar results to the base case were obtained (Table A.2).

Table A.2. Impact of pH in resulted clay minerals.

Brine pH	Initial clay volume percent	Clay volume percent after reactions
6.61	10.5	13.49
5.61	10.5	13.51
4.61	10.5	13.52

A.3 Impact of HCO_3

To investigate the impact of HCO_3, rock-brine reactions were modeled with the different concentrations of HCO_3 in the brine. In the first case, the concentration of HCO_3 has been decreased to one tenth of the base case amount. Similar results to the base case (Fig. 5) were observed. In the second case, the amount of HCO_3 has been increased to ten times of the base case amount in the brine. The obtained results show a slight decrease in the amount of clay minerals formed.

Table A.3. Impact of HCO_3 in resulted clay minerals.

HCO_3 (mg/l)	Initial clay volume percent	Clay volume percent after reactions
606	10.5	13.49
60.6	10.5	13.54
6060	10.5	12.93

A.4 Impact of Sodium

To investigate the impact of Na^+ in brine, rock-brine reactions were modeled with different concentrations of Na^+. In the first case, the amount of Na^+ was decreased to one half of the base amount. As slight increase in the clay portion in comparison to the base case brine composition was observed (Table A.4). In the second case, the amount of Na^+ has been increased to two times the base case amount. In this case, results show about 4.5 percent less clay formation in compare

to the base case brine composition. The clay minerals form 9.01 percent of the total rock volume after five reaction steps.

Table A.4. Impact of Na^+ in resulted clay minerals.

Na^+ (mg/l)	Initial clay volume percent	Clay volume percent after reactions
32,190	10.5	13.49
16,095	10.5	13.74
64,380	10.5	9.01

With the highest amount of Na^+ in the system, an increase in albite occurs after five reaction steps (Fig. A.1). The amount of albite is increased from initial mass of 1908 grams to 2379 grams in reaction step 5. In this case, clay mineral conversion to albite can be seen.

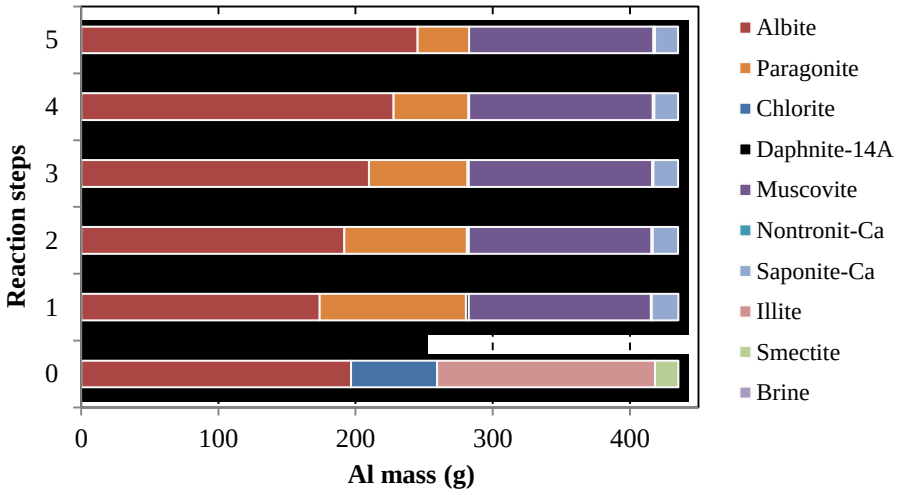

Figure A.1. The change in total Al mass in case with the brine which includes two times more Na compared to the base case brine composition. After the first reaction step the total amount of albite increases while paragonite decreases. Other Al minerals have small changes.

A.5 Impact of initial feldspar

To investigate the impact of feldspar abundance, rock-brine reactions were modeled with the different available amounts of albite in the initial rock composition. In the first case, the amount of albite was increased to twice the base case amount. Similar results to the base case rock composition (Fig. 5) were observed (Table A.5). In the second case, no albite is available in the

initial rock composition. The total amount of clay minerals after reactions stays almost unchanged because there is no albite in the system to convert to clay minerals. Clay minerals form 10.5 percent of the total rock volume before reactions. This number changes to 10.7 percent after five reaction steps.

Table A.5. Impact of feldspar in resulted clay minerals.

Volume percentage of feldspar	Initial clay volume percent	Clay volume percent after reactions
11.5	10.5	13.49
23	10.5	13.49
0	10.5	10.71

A.6 Impact of initial clay

To study the impact of available clay amount in the initial rock composition, rock-brine reactions were modeled with different available amounts of clay (similar clay type to the base case). In the first case, the initial amount of clay minerals has been increased to twice the base case amount. Results show a 4.62 volume percent increase in clay portion of the rock. In the second case, reactions were modeled with no clay minerals in the initial rock composition. Results show 0.6 percent clay formation (Table A.6).

Table A.6. Impact of initial clay in resulted clay minerals.

Initial clay volume percent	Clay volume percent after reactions
10.5	13.49
21	25.62
0	0.6

Appendix B – Pure end member clay minerals formation investigations

As it mentioned in section 3-7 of the dissertation, saponite-Ca and nontronite-Ca are smectite family members which are formed in the calculated first reaction step. In the real world, however, these minerals are formed in higher metamorphic temperatures. In this appendix, the formation of these minerals is investigated further.

B.1 Suppressing metamorphic minerals in LLNL thermodynamic dataset

In order to remove the metamorphic minerals from the results, saponite and nontronite were suppressed (not allowed to form) in the LLNL thermodynamic dataset. The rock-brine reactions were modeled in five consecutive steps with the same conditions as run A. The temperature increases from 100 to 130 °C in the first reaction and is then kept constant at 130 °C for the remaining steps. The results can be seen in Fig. B.1. Almost the same amount of clay forms, increasing from 10.5 percent to 13.24 percent. In this case instead of saponite and nontronite, talc is formed.

In the next case, paragonite was also suppressed in addition to saponite and nontronite. An increase in albite rise from 1908 to 2132 gr can be seen in the results. Quartz decreases from initial 8046 to 7651 gr after five reactions.

Although there is a small increase (from 10.5 to 11.74 percent) in the clay portion in the first reaction step, albite formation in the following steps causes the clay portion to decrease after five reaction steps (to 10.95 percent) (Fig. B.2).

B.2 Comparison with PHREEQC database result

All results obtained so far are based on the LLNL thermodynamic dataset. Reactions were also modeled in five steps with the PHREEQC dataset (“Thermodynamic datasets”). Since the temperature range in PHREEQC spans from 0 to 100 °C, all reactions were modeled with a constant temperature equal to 100 °C. The smectite is not included in the PHREEQC dataset, therefore in these models Ca-montmorillonite has been substituted in initial rock composition (Table 3-1) for smectite.

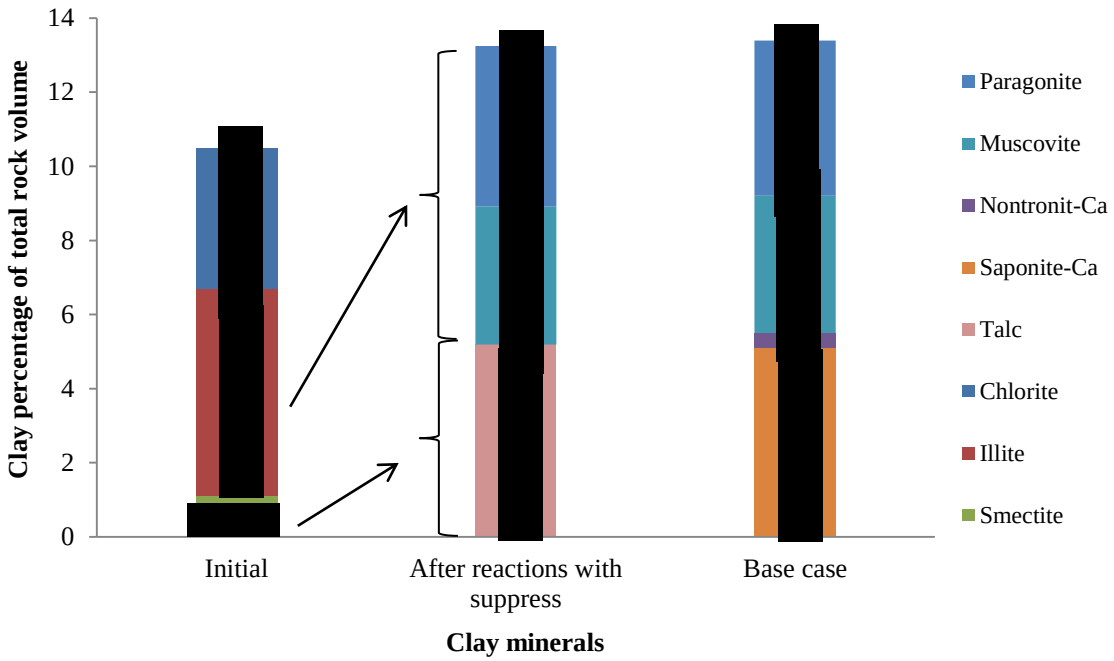

Figure B.1. The comparison of changes in clay volume percentage after five reaction steps with base case. Saponite and nontronite were suppressed to be formed in these runs. About 2.7 percent increase can be seen in the clay portion. Talc, which is another member of smectite family, is formed instead of saponite and nontronite.

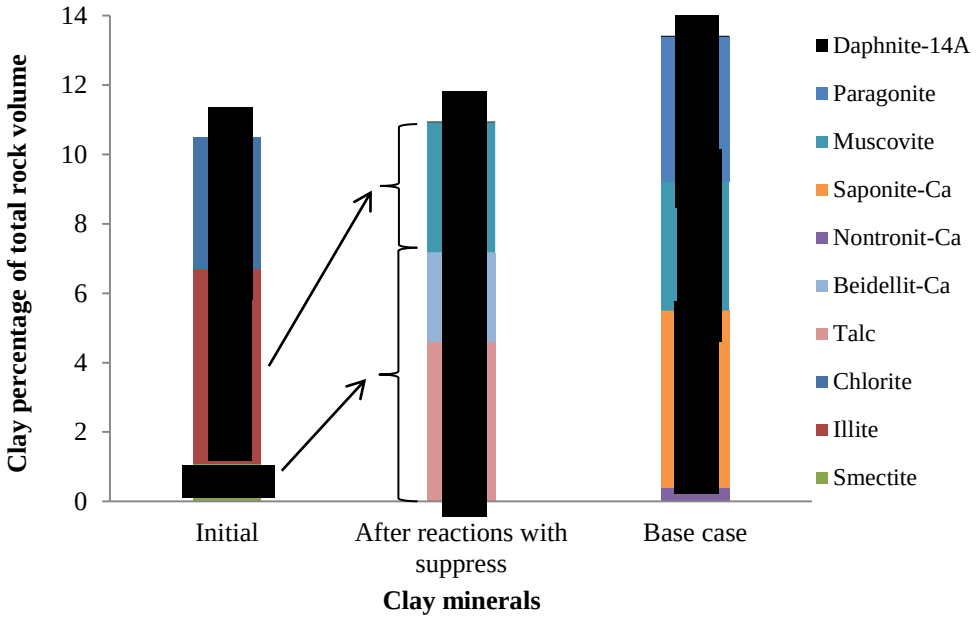

Figure B.2. The comparison of changes in clay volume percentage after five reaction steps with base case. Formation of paragonite, saponite and nontronite were suppressed in these runs. No notable change can be seen in the clay portion. Talc and beidellite are members of smectite family which are formed.

Results show that in the first reaction step the initial clay minerals; Ca-montmorillonite, chlorite, and illite transform to K-mica, kaolinite and talc (Fig. B.3). Quartz decreases from 8046 g to 7866 g after the first reaction and shows slight increase in the rest of steps, changing to 8022 g after five reactions (not shown in the graph).

A comparison between PHREEQC and LLNL thermodynamic database results has been shown in Fig. B.4. For comparison purposes, the temperature of reactions modeled by LLNL thermodynamic database were also held constant at 100 °C. K-mica is the name which is used for muscovite in PHREEQC dataset. Therefore, muscovite formation is also predicted by the PHREEQC database. Although, saponite and nontronite formation are not predicted here, formation of talc is predicted.

Results based on PHREEQC database show the formation of kaolinite which was not predicted by the LLNL thermodynamic dataset. It also appears to form with the LLNL data base at 100 degrees with some minerals being suppressed. Some other diagenetic studies also noted decreases in kaolinite abundance with depth (e.g. Lynch, 1996 and Burton et al., 1987).

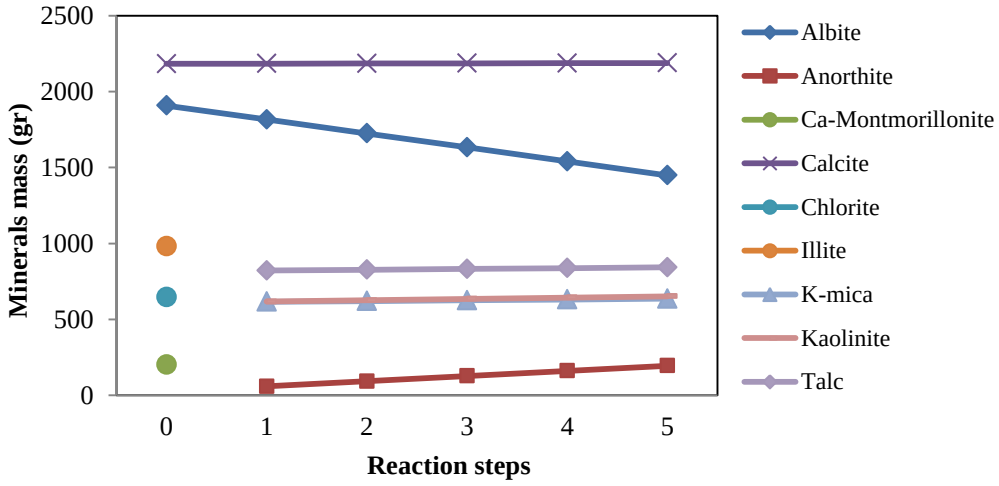

Figure B.3. The changes in major minerals mass with reaction steps. Reaction step 0 shows the initial rock composition. PHREEQC database has been used for these runs. Temperature in all steps is constant and equal to 100 °C.

An albite decrease can also be seen in the results (Fig. B.3). Anorthite, which is the calcium endmember of plagioclase feldspar, is predicted to be formed by the PHREEQC database. With increasing reaction steps conversion of albite to anorthite increases presumably utilizing the calcium in the Ca-montmorillonite. Therefore, although an increase in the clay portion can be seen here (Fig. B.4), it is not as high as when the LLNL thermodynamic database is used. The changes in Al budget is shown in Fig. B.5.

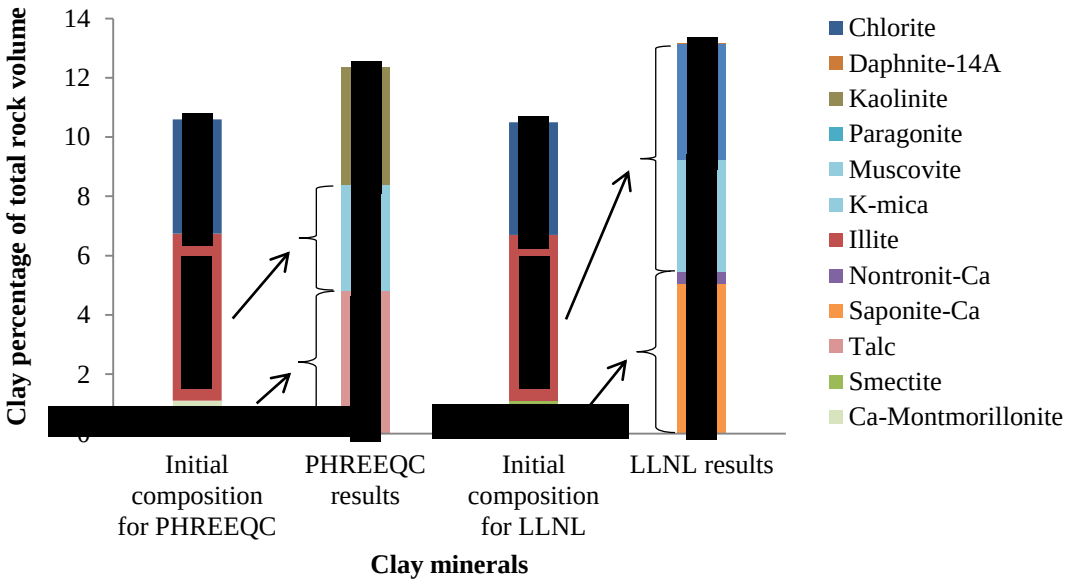

Figure B.4. The comparison of changes in clay volume percentage after five reaction steps obtained from PHREEQC and LLNL thermodynamic datasets. Although the 1.7 percent increase in clay portion can be seen in PHREEQC results it is not as high as LLNL thermodynamic results which shows 2.7 percent increase in clay percentage of total rock volume. The reaction temperature is 100 ºC.

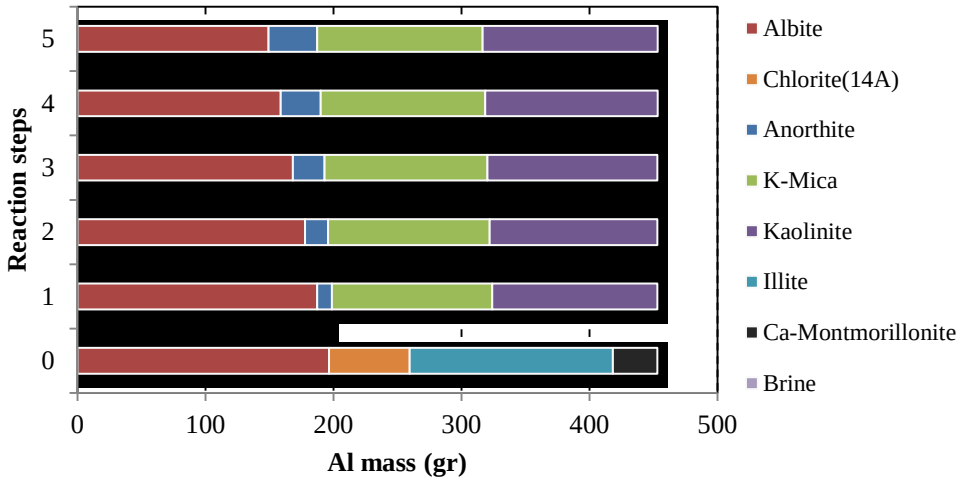

Figure B.5. The change in total Al mass. After first reaction step the total amount of albite decreases while anorthite increases. Other Al-contained minerals have small changes. PHREEQC database has been used for these runs. The reaction temperature is 100 ºC.

Appendix C – Description of utilized algorithms

C.1 Applying geochemical changes

The amount of quartz increase and feldspar reduction should be specified in the input file. The layers of clay that is required to be added to feldspar and/or quartz to reach to the intended volume percent, should also be specified in the input file. This is the step by step algorithm for applying the predicted geochemical changes to a micro-CT image:

1. Read the image file to a matrix,
2. Increasing quartz quantity:
   2.1. For the voxels which belong to the quartz grains, search adjacent voxels and find voxels with the value of 0, which means finding void voxels adjacent to the quartz grains
   2.2. Change the value of those voxels from 0 to the value of the adjacent quartz voxel,
   2.3. Do this procedure until reaching the specified quartz volume percentage,

3. Decreasing feldspar quantity:

   3.1. For the voxels which have the value of 0, search adjacent voxels and find voxels which belong to feldspar grains, which means finding void voxels adjacent to the feldspar grains
   2.2. Change the value of those feldspar voxels to 0,
   2.3. Do this procedure until reaching the specified feldspar volume percentage,

4. Adding newly generated clay voxels:

   4.1. *Feldspar grains, first layer, odd voxels:* For the voxels which belong to the feldspar grains, just for the voxels with odd voxel values, search adjacent voxels and find voxels with the value of 0. Then, change the value of those voxels from 0 to the value of the adjacent feldspar voxel with negative sign.

4.2. *Feldspar grains, first layer, even voxels:* For the voxels which belong to the feldspar grains, just for the voxels with even voxel values, search adjacent voxels and find voxels with the value of 0. Then, change the value of those voxels from 0 to the value of the adjacent feldspar voxel with negative sign.

4.3. *Feldspar grains, second layer, odd voxels:* For the voxels which belong to the first layer of newly generated clay voxels on feldspar grains, just for the voxels with odd voxel values, search adjacent voxels and find voxels with the value of 0. Then, change the value of those voxels from 0 to the value of the adjacent newly generated clay voxel.

4.4. *Feldspar grains, second layer, even voxels:* For the voxels which belong to the first layer of newly generated clay voxels on feldspar grains, just for the voxels with even voxel values, search adjacent voxels and find voxels with the value of 0. Then, change the value of those voxels from 0 to the value of the adjacent newly generated clay voxel.

4.5. *Quartz grains, first layer, odd voxels:* For the voxels which belong to the quartz grains, just for the voxels with odd voxel values, search adjacent voxels and find voxels with the value of 0. Then, change the value of those voxels from 0 to the value of the adjacent quartz voxel with negative sign.

4.6. *Quartz grains, first layer, even voxels:* For the voxels which belong to the quartz grains, just for the voxels with even voxel values, search adjacent voxels and find voxels with the value of 0. Then, change the value of those voxels from 0 to the value of the adjacent quartz voxel with negative sign.

4.7. *Quartz grains, second layer, odd voxels:* For the voxels which belong to the first layer of newly generated clay voxels on quartz grains, just for the voxels with odd voxel values, search adjacent voxels and find voxels with the value of 0. Then, change the value of those voxels from 0 to the value of the adjacent newly generated clay voxel.

4.8. *Quartz grains, second layer, even voxels:* For the voxels which belong to the first layer of newly generated clay voxels on quartz grains, just for the voxels with even voxel values, search adjacent voxels and find voxels with the value of 0. Then, change the value of those voxels from 0 to the value of the adjacent newly generated clay voxel.

5. Write the resulted matrix into an image file.

C.2 Considering the permeability of micropores

This program gets the pore network (.psn) files of the initial image and the image with impermeable microporous clay as the input files and makes a new pore network file containing modified throat conductivity using a defined equation. This is the step by step algorithm:

1. For the initial image, read the pore network (.psn) parameters to the proper matrices.
2. For the image with impermeable microporous clay, read the pore network (.psn) parameters to the proper matrices.
3. For pore i in the initial image find pore j which is connected to i.
4. Find the throat p which connects i to j.
5. Find the throat q which connects j to i.
6. For the pore i in the initial image find the equivalent pore i´ in the impermeable microporous image.
7. For the pore j in the initial image find the equivalent pore j´ in the impermeable microporous image.
8. Find the throat r which connects i´ to j´.
9. Calculate the ratio of the cross section area of r to the cross section area of p.
10. Using the defined equation and the value calculated in 9, calculate the modified conductivity of throats p and q considering permeable micropores.
11. Do these steps for all pores and find the modified conductivity for all throats.
12. Write a new pore network (.psn) file containing modified throat conductivity.

Appendix D – Pore network statistics

D.1 Sample 59

D.1.1 Distribution of Inscribed Pore Diameters

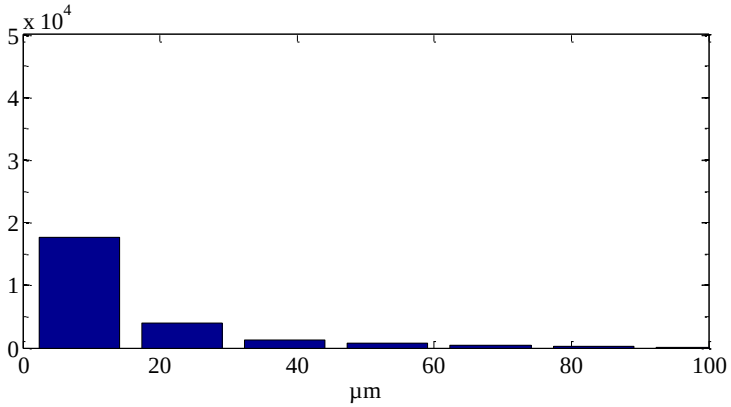

Figure D.1. Inscribed pore diameters, sample 59, initial image.

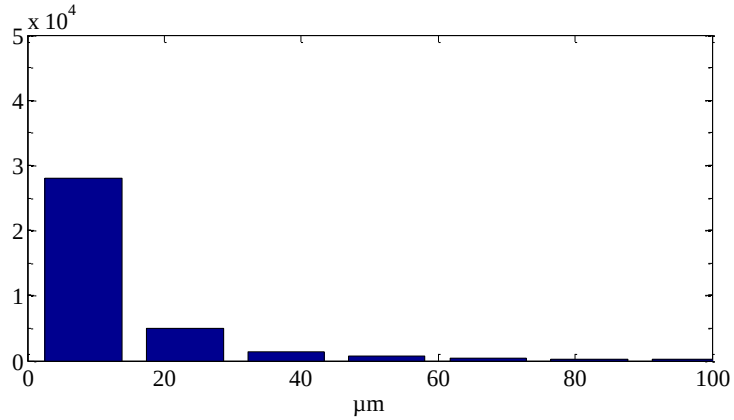

Figure D.2. Inscribed pore diameters, sample 59, altered, clay is not microporous.

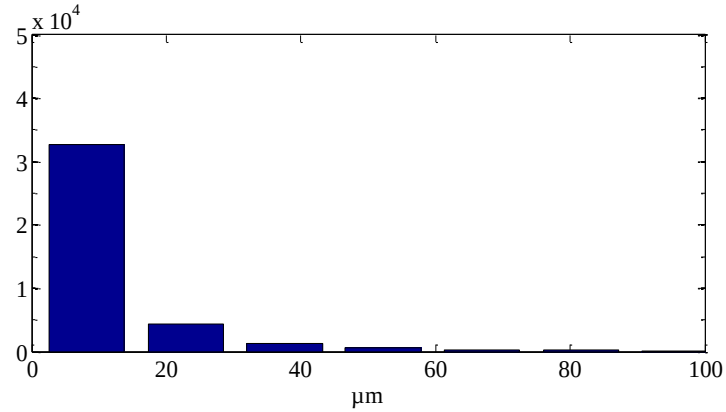

Figure D.3. Inscribed pore diameters, sample 59, altered, microporous but impermeable clay.

D.1.2 Distribution of Pore-Throat Equivalent Diameters

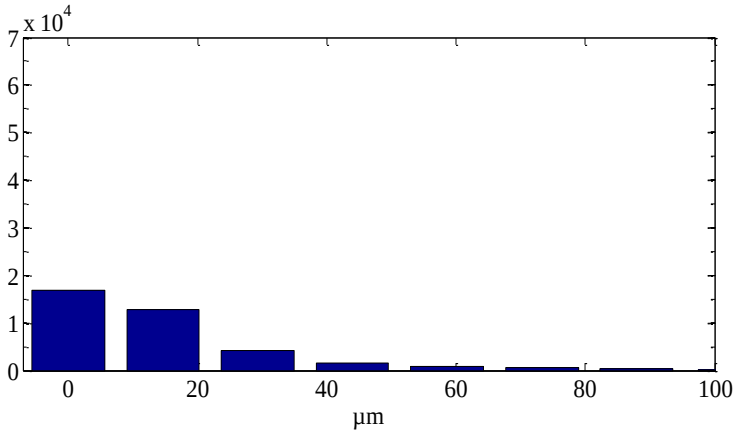

Figure D.4. Pore-throat equivalent diameters, sample 59, initial image.

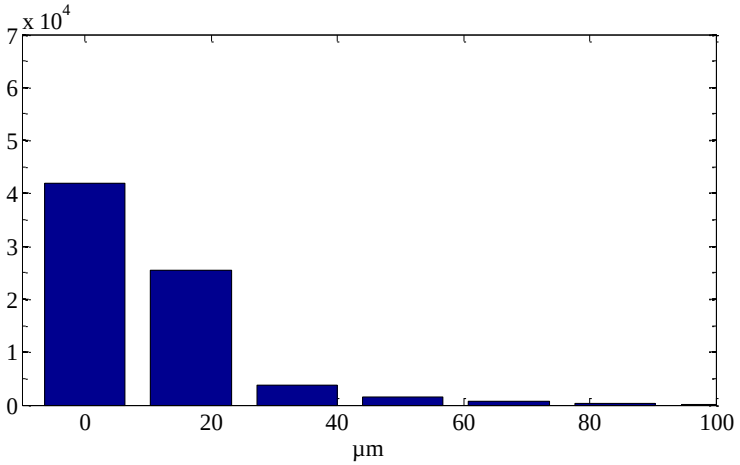

Figure D.5. Pore-throat equivalent diameters, sample 59, altered, clay is not microporous.

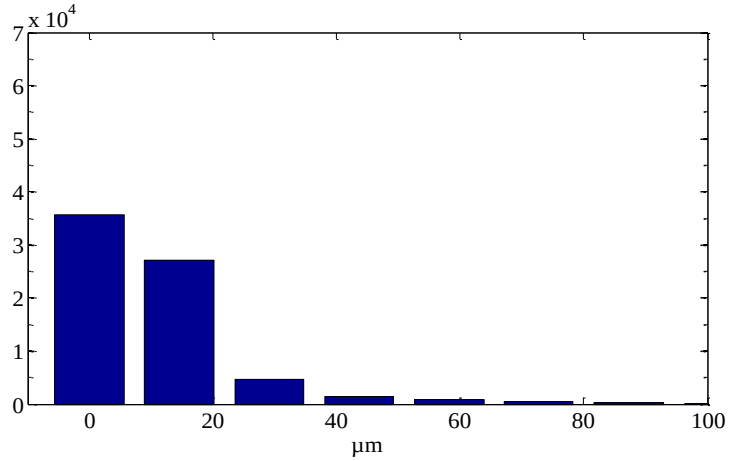

Figure D.6. Pore-throat equivalent diameters, sample 59, altered, microporous but impermeable clay.

D.1.3 Distribution of Pore Coordination Numbers

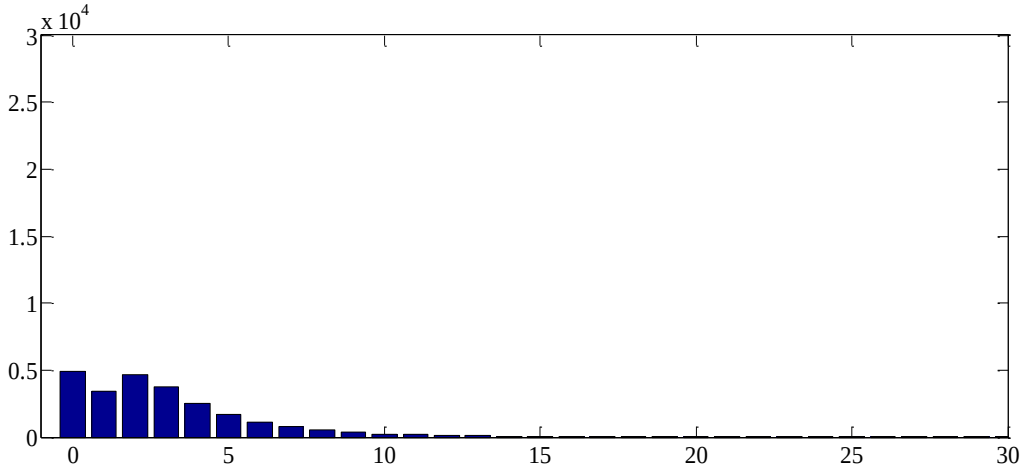

Figure D.7. Pore coordination numbers, sample 59, initial image.

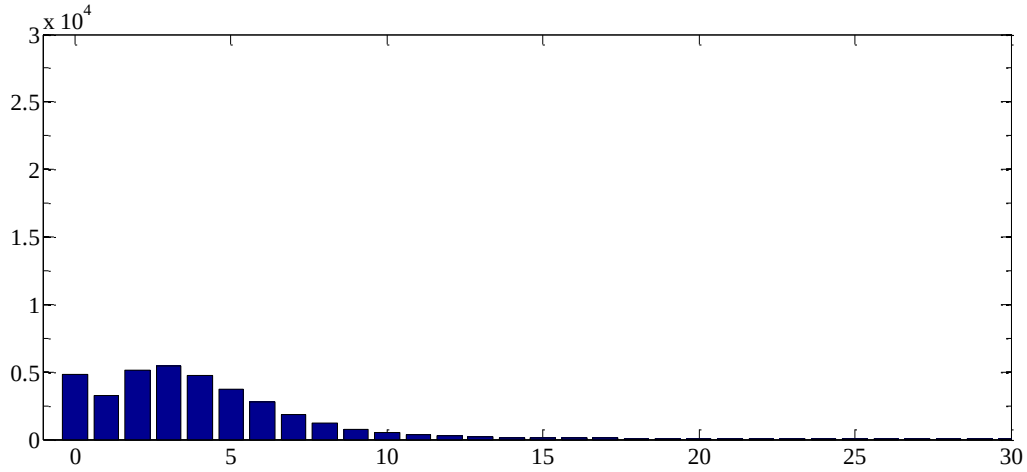

Figure D.8. Pore coordination numbers, sample 59, altered, clay is not microporous.

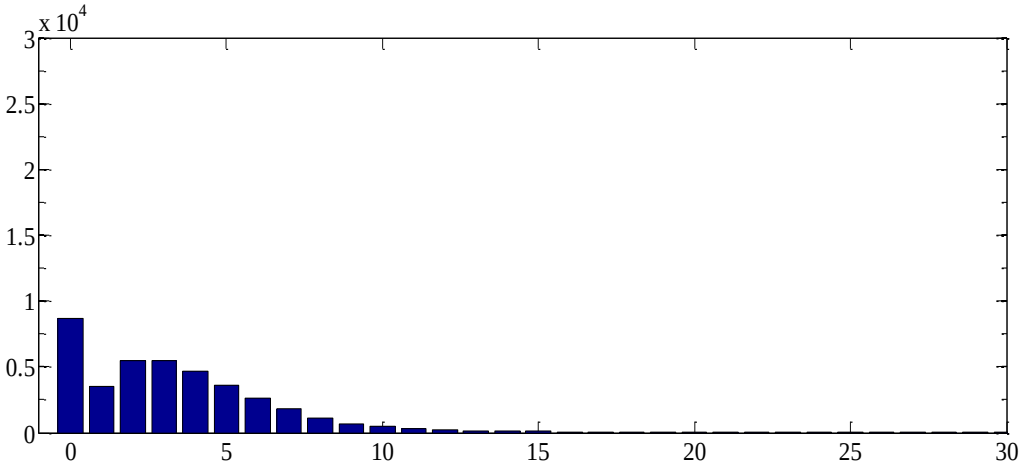

Figure D.9. Pore coordination numbers, sample 59, altered, microporous but impermeable clay.

D.2 Sample 61

D.2.1 Distribution of Inscribed Pore Diameters

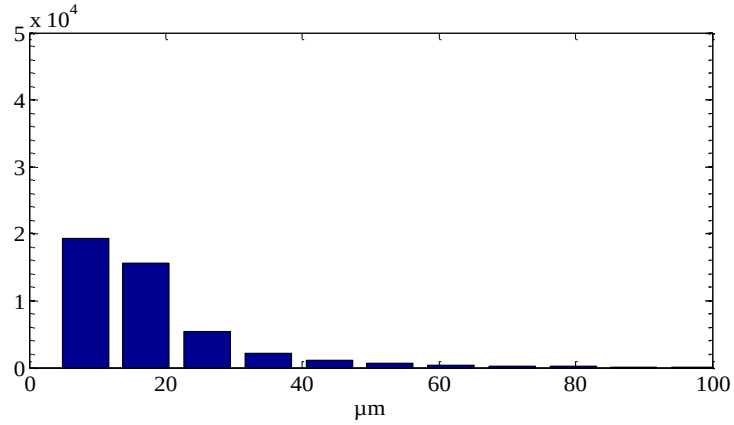

Figure D.10. Inscribed pore diameters, sample 61, initial image.

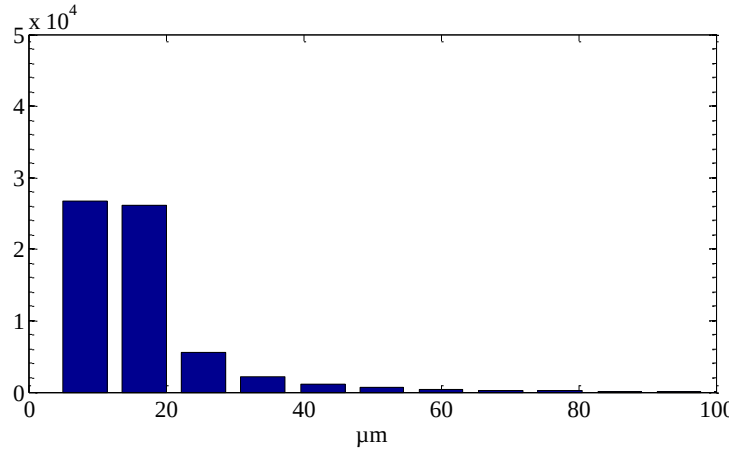

Figure D.11. Inscribed pore diameters, sample 61, altered, clay is not microporous.

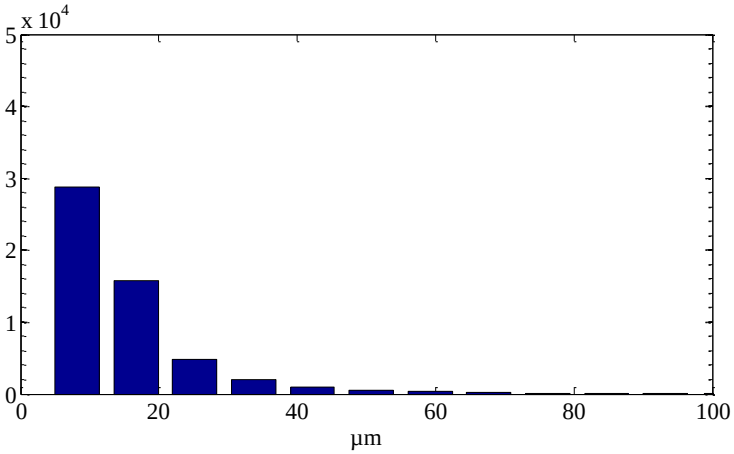

Figure D.12. Inscribed pore diameters, sample 61, altered, microporous but impermeable clay.

D.2.2 Distribution of Pore-Throat Equivalent Diameters

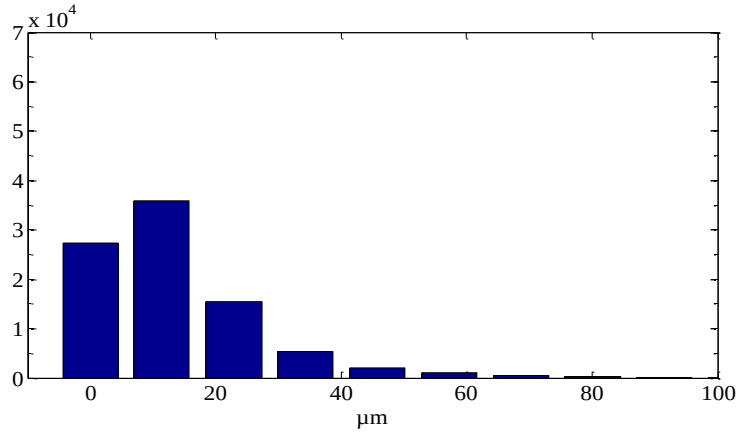

Figure D.13. Pore-throat equivalent diameters, sample 61, initial image.

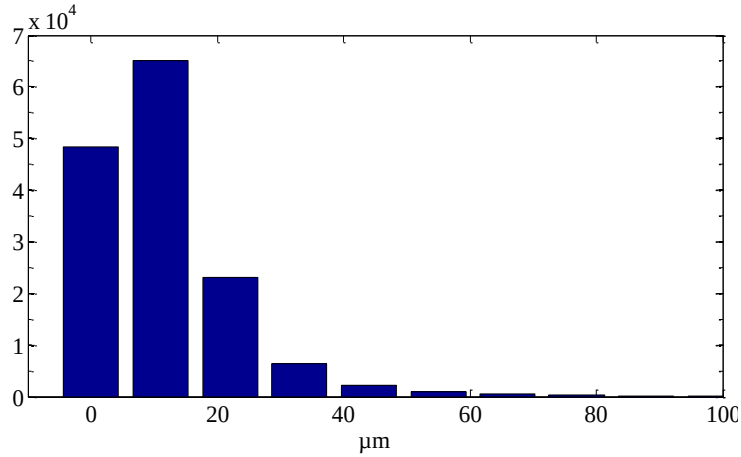

Figure D.14. Pore-throat equivalent diameters, sample 61, altered, clay is not microporous.

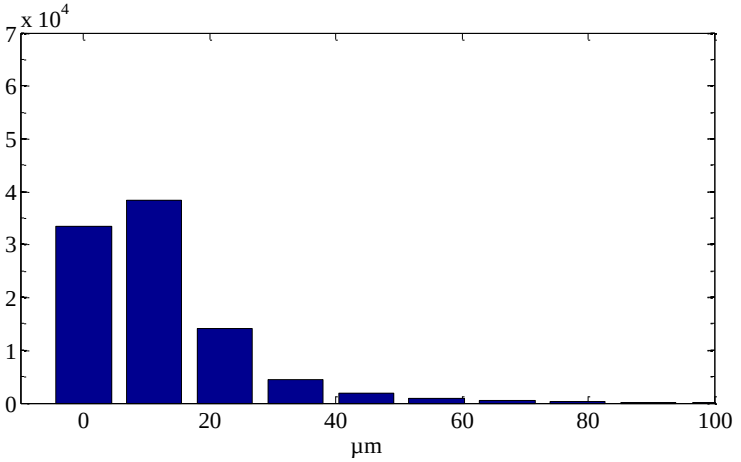

Figure D.15. Pore-throat equivalent diameters, sample 61, altered, microporous but impermeable clay.

D.2.3 Distribution of Pore Coordination Numbers

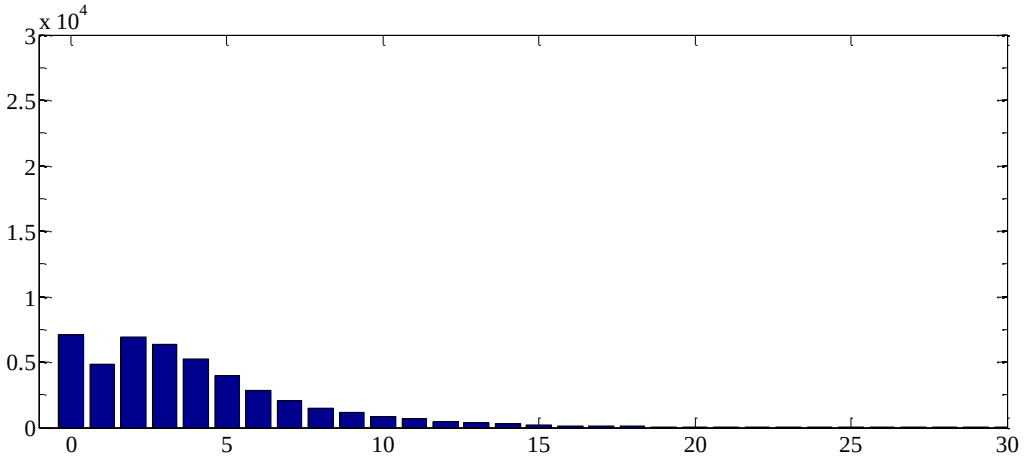

Figure D.16. Pore coordination numbers, sample 61, initial image.

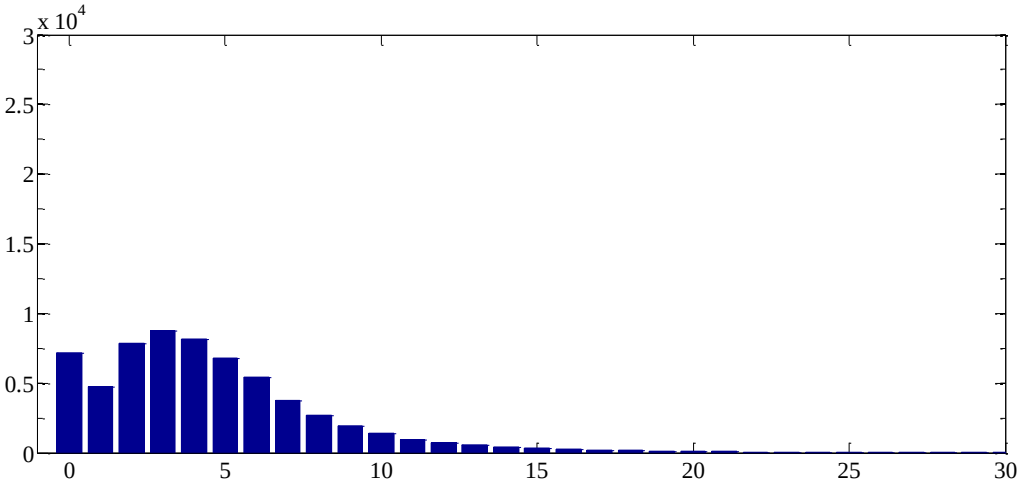

Figure D.17. Pore coordination numbers, sample 61, altered, clay is not microporous.

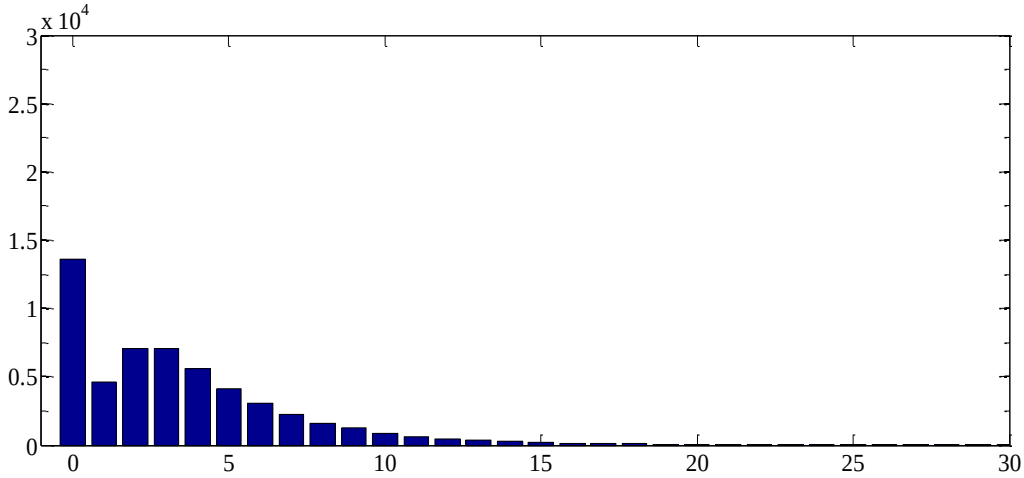

Figure D.18. Pore coordination numbers, sample 61, altered, microporous but impermeable clay.

D.3 Sample 62

D.3.1 Distribution of Inscribed Pore Diameters

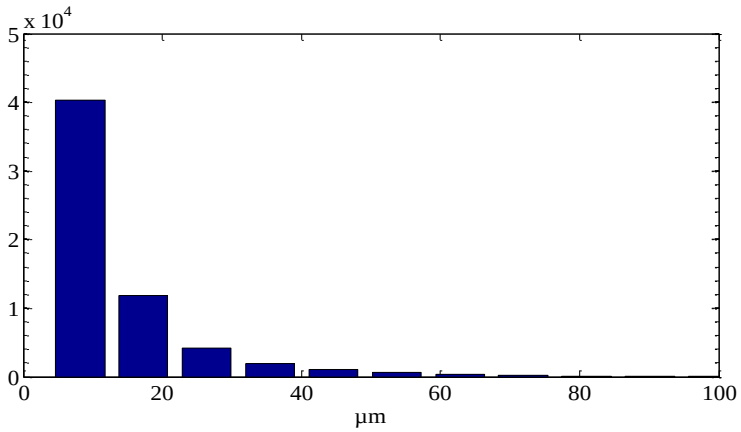

Figure D.19. Inscribed pore diameters, sample 62, initial image.

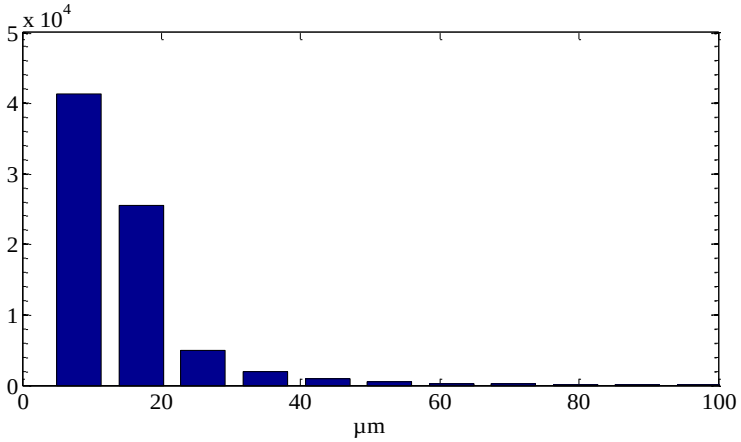

Figure D.20. Inscribed pore diameters, sample 62, altered, clay is not microporous.

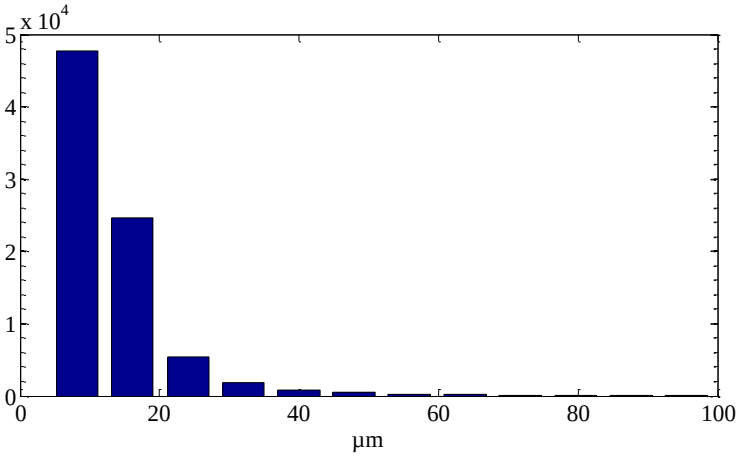

Figure D.21. Inscribed pore diameters, sample 62, altered, microporous but impermeable clay.

D.3.2 Distribution of Pore-Throat Equivalent Diameters

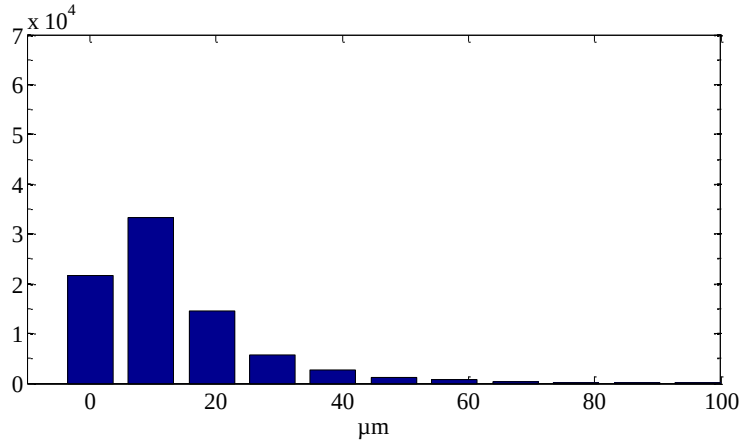

Figure D.22. Pore-throat equivalent diameters, sample 62, initial image.

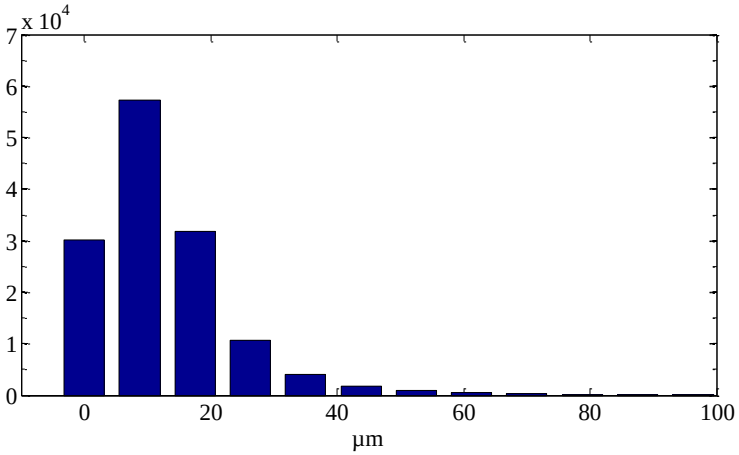

Figure D.23. Pore-throat equivalent diameters, sample 62, altered, clay is not microporous.

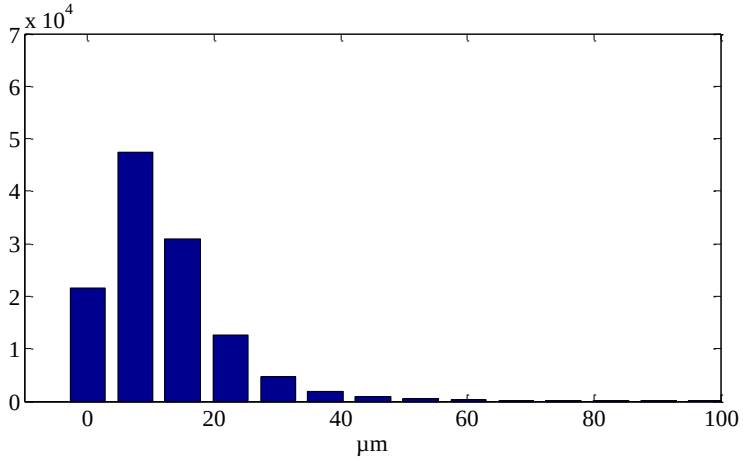

Figure D.24. Pore-throat equivalent diameters, sample 62, altered, microporous but impermeable clay.

D.3.3 Distribution of Pore Coordination Numbers

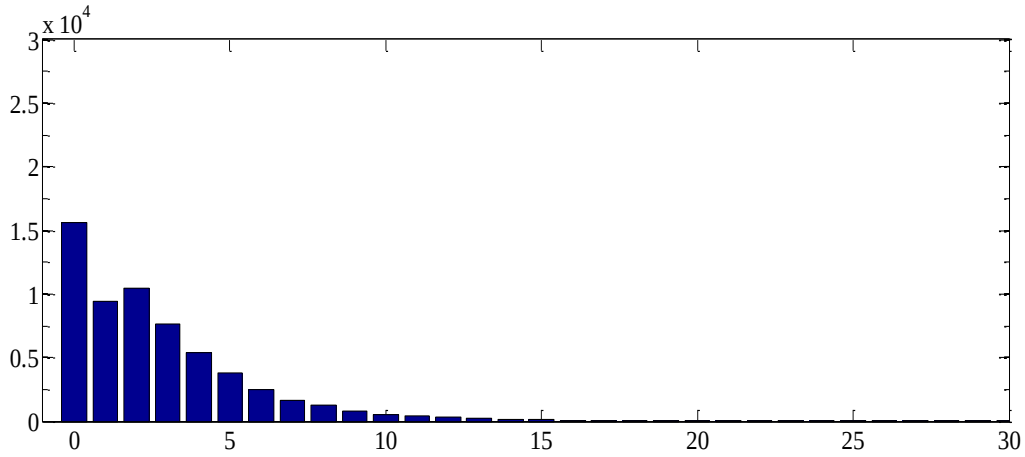

Figure D.25. Pore coordination numbers, sample 62, initial image.

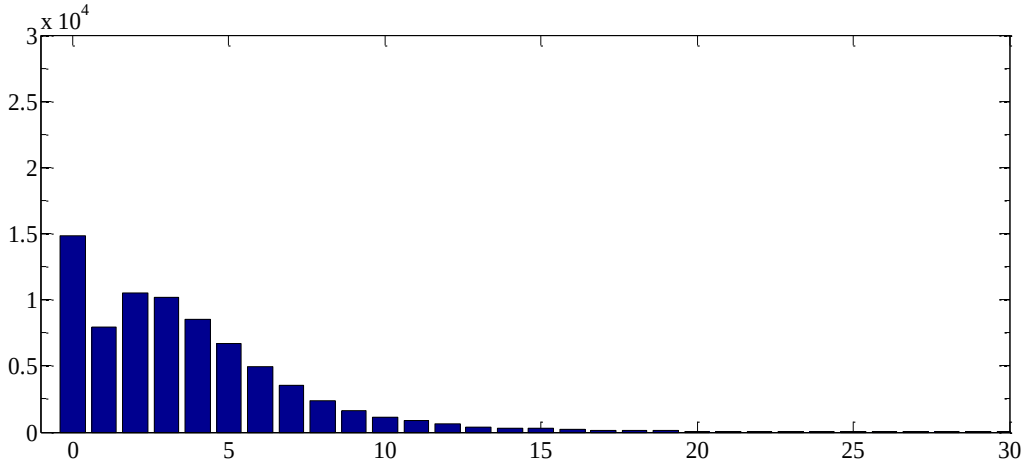

Figure D.26. Pore coordination numbers, sample 62, altered, clay is not microporous.

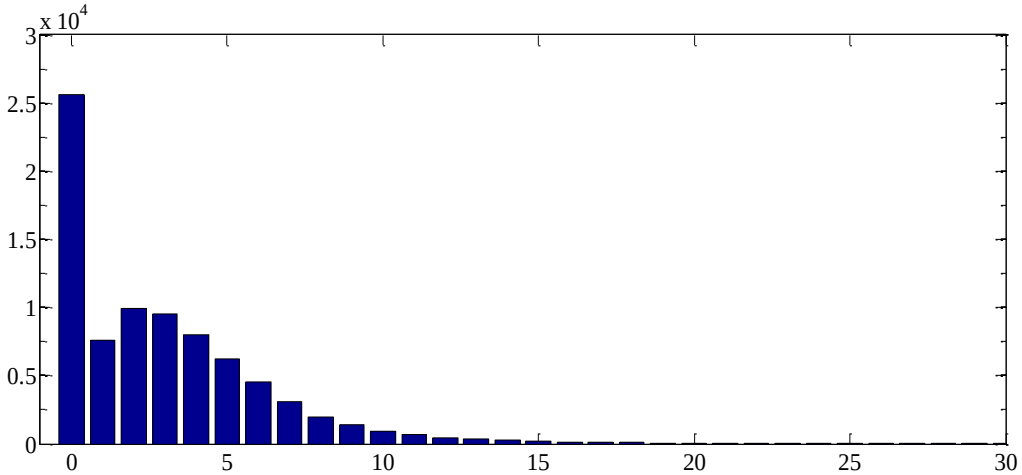

Figure D.27. Pore coordination numbers, sample 62, altered, microporous but impermeable clay.

Vita

Masoud Safari-Zanjani was born in 1983, in Zanjan, Iran, to Khalilollah and Parvin. He attended Rouzbeh High School for his secondary school education and graduated in 2000. He then proceeded to Iran University of Science and Technology, from where he earned a Bachelor of Engineering in Civil Engineering in 2005. Thereafter, in 2008, he received his master degree in Geotechnical Engineering from Bu-Ali Sina University in Iran. In 2012, he started his PhD studies in Craft & Hawkins Department of Petroleum Engineering at Louisiana State University, Louisiana, USA. He is currently a candidate for the PhD in Petroleum Engineering, to be awarded in August 2016. Masoud is a nature enthusiast who enjoys cycling.